



National Library
of Canada

Bibliothèque nationale
du Canada

Canadian Theses Service

Service des thèses canadiennes

Ottawa, Canada
K1A 0N4

NOTICE

The quality of this microform is heavily dependent upon the quality of the original thesis submitted for microfilming. Every effort has been made to ensure the highest quality of reproduction possible.

If pages are missing, contact the university which granted the degree.

Some pages may have indistinct print especially if the original pages were typed with a poor typewriter ribbon or if the university sent us an inferior photocopy.

Reproduction in full or in part of this microform is governed by the Canadian Copyright Act, R.S.C. 1970, c. C-30, and subsequent amendments.

AVIS

La qualité de cette microforme dépend grandement de la qualité de la thèse soumise au microfilmage. Nous avons tout fait pour assurer une qualité supérieure de reproduction.

S'il manque des pages, veuillez communiquer avec l'université qui a conféré le grade.

La qualité d'impression de certaines pages peut laisser à désirer, surtout si les pages originales ont été dactylographiées à l'aide d'un ruban usé ou si l'université nous a fait parvenir une photocopie de qualité inférieure.

La reproduction, même partielle, de cette microforme est soumise à la Loi canadienne sur le droit d'auteur, SRC 1970, c. C-30, et ses amendements subséquents.

UNIVERSITY OF ALBERTA

IMAGE PROCESSING TECHNIQUES FOR ANALYSIS OF
FULL COLOR TURBULENT JET IMAGES

BY

ROBERT PATRICK CAMPBELL

A THESIS

SUBMITTED TO THE FACULTY OF GRADUATE STUDIES AND RESEARCH
IN PARTIAL FULFILLMENT OF THE REQUIREMENTS FOR THE DEGREE
OF MASTER OF SCIENCE.

DEPARTMENT OF MECHANICAL ENGINEERING

EDMONTON, ALBERTA

SPRING 1991



National Library
of Canada

Bibliothèque nationale
du Canada

Canadian Theses Service Service des thèses canadiennes

Ottawa, Canada
K1A 0N4

The author has granted an irrevocable non-exclusive licence allowing the National Library of Canada to reproduce, loan, distribute or sell copies of his/her thesis by any means and in any form or format, making this thesis available to interested persons.

The author retains ownership of the copyright in his/her thesis. Neither the thesis nor substantial extracts from it may be printed or otherwise reproduced without his/her permission.

L'auteur a accordé une licence irrévocable et non exclusive permettant à la Bibliothèque nationale du Canada de reproduire, prêter, distribuer ou vendre des copies de sa thèse de quelque manière et sous quelque forme que ce soit pour mettre des exemplaires de cette thèse à la disposition des personnes intéressées.

L'auteur conserve la propriété du droit d'auteur qui protège sa thèse. Ni la thèse ni des extraits substantiels de celle-ci ne doivent être imprimés ou autrement reproduits sans son autorisation.

ISBN 0-215-66692-7

UNIVERSITY OF ALBERTA

RELEASE FORM

NAME OF AUTHOR: ROBERT PATRICK CAMPBELL

TITLE OF THESIS: IMAGE PROCESSING TECHNIQUES FOR ANALYSIS
OF FULL COLOR TURBULENT JET IMAGES

DEGREE: MASTER OF SCIENCE

YEAR THIS DEGREE AWARDED: 1991

PERMISSION IS HEREBY GRANTED TO THE UNIVERSITY OF ALBERTA LIBRARY TO REPRODUCE SINGLE COPIES OF THIS THESIS AND TO LEND OR SELL SUCH COPIES FOR PRIVATE, SCHOLARLY OR SCIENTIFIC RESEARCH PURPOSES ONLY.

THE AUTHOR RESERVES OTHER PUBLICATION RIGHTS, AND NEITHER THE THESIS NOR EXTENSIVE EXTRACTS FROM IT MAY BE PRINTED OR OTHERWISE REPRODUCED WITHOUT THE AUTHOR'S WRITTEN PERMISSION.



#5 9701 84 AVENUE

GRANDE PRAIRIE, ALBERTA

T8V 4Z8

DATE: January 3, 1991

"...turbulence, baby."

-Jimi Hendrix

UNIVERSITY OF ALBERTA

FACULTY OF GRADUATE STUDIES AND RESEARCH

THE UNDERSIGNED CERTIFY THAT THEY HAVE READ, AND RECOMMEND TO THE FACULTY OF GRADUATE STUDIES AND RESEARCH FOR ACCEPTANCE, A THESIS ENTITLED IMAGE PROCESSING TECHNIQUES FOR ANALYSIS OF FULL COLOR TURBULENT JET IMAGES.

SUBMITTED BY ROBERT PATRICK CAMPBELL IN PARTIAL FULFILLMENT OF THE REQUIREMENTS FOR THE DEGREE OF MASTER OF SCIENCE.


M. D. CHECKEL, Supervisor


D. J. WILSON, Supervisor


N. RAJARATNAM

Date: January 2, 1991

To Mom and Dad

Abstract

Techniques have been developed to utilize digital image processing in the extraction of quantitative information from full color flow visualization images. These techniques have been used to investigate the interactions of two submerged round jets discharging parallel to one another.

Sheets of laser light were used to stimulate laser induced fluorescence (LIF) in jet fluid dyed with fluorescent dye, allowing the study of internal jet structure. The non-linear transformations necessary to determine dye concentration from image hue and intensity have been investigated and a workable method has been developed. The non-linearities considerably complicated the data extraction process.

Four different flow configurations were investigated, including initially laminar and turbulent jets, alone and interacting with other jets, all at a discharge tube Reynolds number of $Re_D = 1600$. The interaction between two jets was well described using a simple point addition of momentum - a zero interaction entrainment model. The utilization of the image processing system allows new measures of jet behavior, such as the instantaneous measurement of jet isopleth area. This type of measure has interesting implications in combustion applications. It was found that an almost constant area of a turbulent jet was within a given isopleth limit.

Acknowledgement

I would like to thank Dr. M. D. Checkel and Dr. D. J. Wilson for their help and guidance throughout this thesis and all of their long distance telephone calls to California. The financial support of the Natural Sciences and Engineering Research Council of Canada is gratefully acknowledged. I would like to thank Wayne Pittman, Cliff Johnston and Brian Zelt for their assistance with the Laser Doppler Velocimeter measurements. Thanks also to Al Muir and all of the machine shop staff for their excellent work. Steve McEvoy proof read the thesis and Karen McEvoy's assistance with the figures was invaluable. Thanks for keeping me sane, guys!

Most of all, I wish to thank Valerie, who said "Yes".

Table of Contents

Chapter	Page
<u>1 - Introduction</u>	1
<u>2 - Flow Visualization</u>	4
Background and Overview	4
Lasers, Fiber Optics and Laser Sheet Lighting	8
Laser Induced Fluorescence	15
<u>3 - Introduction to Digital Image Processing</u>	20
Background and Overview	20
Intensity-Only, RGB, and HSI Images	21
Image Digitizing and Processing Equipment	24
Determining World Pixel Position and Uncertainty	37
<u>4 - Digital Image Processing of Jet Images</u>	46
Overview	46
Concentration from Intensity: Analytical Model	46
Dye Attenuation of Laser Light Sheet Power	56
Correction of Light Sheet Non-Uniformity	66
Color Separation of Jet Fluid	75
<u>5 - Interacting Turbulent Jets</u>	81

Background and Overview	81
Jet Flow System	84
Jet Configurations	88
Velocity Measurements	88
Zero Interaction Jet Model	93
Eulerian Time Averaging of Jet Concentration	97
Mean and Fluctuating Full Field Jet Concentration	106
<u>6 - Conclusions and Recommendations</u>	115
<u>References</u>	119

List of Figures

Figure 2-1: Gaussian Light Sheet Created by Cylindrical Lens.	9
Figure 2-2: Input Optics Schematic	11
Figure 2-3: Light Sheet Output Optics Schematic	13
Figure 2-4: Beam Diameter and Light Sheet Thickness	14
Figure 2-5: Illumination of Experimental Test Section	16
Figure 3-1: HSI Color Scale	25
Figure 3-2: Image Acquisition and Processing System Schematic Diagram . . .	27
Figure 3-3: Non-Linear Video Camera Response	29
Figure 3-4: Camera Correction Function	31
Figure 3-5: Camera Response to Step Change in Intensity	32
Figure 3-6: RGB Response to Step Change in Input Intensity	34
Figure 3-7: Slide Digitizing Equipment Schematic	36
Figure 3-8: Imaging Geometry	38
Figure 3-9: Laser Sheet Thickness Error	42
Figure 3-10: Particle Speed and Video Scanning Method	45
Figure 4-1: Light Sheet Coordinate System	51
Figure 4-2: Light Sheet Attenuation in Disodium Fluorescein	58
Figure 4-3: Light Sheet Attenuation in Rhodamine 610	59
Figure 4-4: Functional Form of Fluorescein Attenuation Factor Φ_F	62
Figure 4-5: Functional Form of Rhodamine Attenuation Factor, Φ_R	63
Figure 4-6: Typical Jet Image Fluorescence Distribution	67
Figure 4-7: Fluorescence Distribution in Constant Concentration Dye	69

Figure 4-8: The Effect of Median Filtering on Light Sheet Correction	71
Figure 4-9: Filtered Light Sheet and Resulting Normalized Jet Image	73
Figure 4-10: Laminar Dye Column Light Sheet Normalization	74
Figure 4-11: Hue Variation With Mixture Composition	77
Figure 4-12: Hue Calibration Curve	78
Figure 5-1: Schematic of Flow Apparatus	85
Figure 5-2: Schematic of Discharge Tubes and Turbulence Generators	87
Figure 5-3: Mean Velocity Profile at Jet Outlet	90
Figure 5-4: Fluctuating Velocity at Jet Outlet	92
Figure 5-5: Mean Turbulent Jet Velocity Profiles at $z/D = 8.5$	94
Figure 5-6: Mean Turbulent Jet Velocity Profiles at $z/D = 17.0$	95
Figure 5-7: Effect of Displaced Center Line at $Z/D = 8.5$	98
Figure 5-8: Effect of Displaced Center Line at $Z/D = 17$	99
Figure 5-9: Fluctuating Velocity Profiles for Turbulent Jets	100
Figure 5-10: Mean Concentration Profiles at $z/D = 8.6$	103
Figure 5-11: Mean Concentration Profiles at $z/D = 17.1$	104
Figure 5-12: Concentration Fluctuations at $z/D = 8.6$ and $z/D = 17.1$	107
Figure 5-13: Instantaneous Concentration Field in Single Turbulent Jet	109
Figure 5-14: Mean Jet Concentration Fields	110
Figure 5-15: Mean and Fluctuation Isopleth Area in a Single Turbulent Jet	113

List of Plates

Plate 4-1: Data Slide From Two Color Jet Interaction Experiment	48
Plate 4-2: Data Slide of Single Dye Experiment	50

Notation

$a(C)$	-	Dye attenuation factor.
A	-	Mean isopleth area.
A'	-	Fluctuating isopleth area.
$C(x,z,t)$	-	Dye concentration function.
C	-	Mean dye concentration.
C'	-	Fluctuating dye concentration.
C_0	-	Maximum dye concentration in jet.
d	-	Water depth in tow tank (mm).
D	-	Discharge tube nozzle diameter (mm).
$F(x,z,t)$	-	Fluorescence function in image processor memory.
$f(C)$	-	Conversion function relating intensity perceived by the camera to $F(x,z,t)$.
f	-	Lens focal length.
h	-	Non-dimensional hue angle.
H	-	Pixel hue (color).
HSI	-	Hue, saturation and intensity.
I	-	Pixel intensity (brightness).
i_{AREA}	-	Isopleth area fluctuation intensity.
$I_{LS}(x,z)$	-	Light sheet intensity distribution.
L	-	Tow tank length, inside dimension (mm).
r	-	Distance (in mm) from light sheet focal point.
RGB	-	Red, green and blue.

S	-	Pixel saturation (white light content).
t	-	Time - usually denotes which image is being worked with.
\bar{u}	-	Instantaneous velocity.
U	-	Mean velocity.
U'	-	Fluctuating Velocity.
W	-	Tow tank width, inside dimension (mm).
X	-	Horizontal position (in mm) to left (-ve) or right (+ve) of tank centerline.
Z	-	Vertical position (in mm) in jet flow direction measured from jet discharge tube nozzle.
δ_v	-	Jet velocity profile half width.
δ_{vc}	-	Jet concentration profile half width.
ϵ	-	Pixel positional error.
ϕ	-	Second form of attenuation factor.
θ	-	Angle above (-ve) or below (+ve) light sheet horizontal centerline.

Superscripts

n	-	Exponent in concentration/fluorescence relation.
m	-	Exponent in concentration/attenuation relation.

Subscripts

o	-	Denotes base or reference position.
1	-	Denotes light sheet #1 (from left in image).
2	-	Denotes light sheet #2 (from right in image).

- F - Denotes disodium fluorescein.
- I - Denotes image coordinates
- LS - Denotes light sheet.
- R - Denotes rhodamine 610 (rhodamine B).
- th - Denotes theoretical.
- W - Denotes world (real) coordinates.

Chapter 1 - Introduction

This thesis was undertaken as an exploratory study of techniques for quantitative analysis of flow visualization for the study of interacting turbulent jets. Like many voyages of exploration, a great deal of ground was covered, and many interesting places were visited but could not all be studied in exhaustive depth. Starting with an empty laboratory, this journey led through the many areas of study such as lasers, Gaussian optics, fiber optics, fluorescent dyes, photography, image processing equipment and processing techniques before arriving at a workable full field concentration measurement system.

This thesis is a map of the journey. This map hopefully has identified most of the key areas and problems that must be addressed, and shows the workable solutions that have been developed to overcome these problems. All of these key areas merit closer study to perfect, expand, and better utilize the developed full field concentration measurement system. Hopefully this thesis can be used as a guide to finding these key areas.

The underlying concept of flow visualization is the use of light as a diagnostic tool for the study of mixing processes in fluid mechanics. A good way, then, to describe the development of the concentration measurement system is to follow the path of light through the experiment.

The jet mixing experiment was visualized with thin sheets of light used to stimulate fluorescent dye in the jet fluid. This type of visualization produces a visual slice of the mixing experiment, in this case a slice through the axis of symmetry of a

single jet or interacting parallel jets. Because the dyed jet fluid is virtually transparent when not fluorescing, the inner structure of the jets is not obscured as with the use of opaque dyes for flow visualization. The intensity of the fluorescent light from the dyed fluid is a measure of the concentration of the jet fluid.

Following the light path, the light was generated by a laser, transported to the jet tank through fiber optic cables, and transformed into thin sheets of light. The laser, the optics developed to couple the laser beam into the fiber optic cables, the fiber optics used to transport the light, and the output optics used to transform the light into a thin sheet are all discussed in the first half of Chapter 2. Some of the light from the light sheets was absorbed by the fluorescent dye in the jet fluid, and stimulated the dye molecules to emit light in all directions at a different wavelength. Different fluorescent dyes will emit different wavelengths (colors) of light, even when absorbing the same type of laser light.

The second half of Chapter 2 discusses the mechanisms of laser induced fluorescence, the absorptive and emissive properties of the laser dyes used in this study, and the external factors which affect their performance. Instantaneous fluorescent light distributions of dyed jet fluid in the light sheet were captured using a 35 mm camera using slide film. The color slide film recorded the intensity distribution as a color-dependent optical density distribution. This distribution was later measured by a video camera and converted to a digital image suitable for computer manipulation by digital image processing equipment. This digital image is also a measure of the concentration distribution of the dyed jet fluid. Manipulation

of the digital image can be used to determine this concentration distribution.

Chapter 3 introduces the concept of digital image processing, reviews ways of describing digital images in terms of colors and intensities and discusses the equipment used in this study to capture and manipulate images, and errors associated with this type of analysis. With the groundwork has established, Chapter 4 describes the specific image processing techniques developed to infer the jet fluid concentration distribution from the digital image. Since different fluorescent dyes emit light at different wavelengths, fluorescent light color is examined as a potential means of tracking more than one scalar concentration in the flow field.

The application section of the thesis, Chapter 5, shows the results obtained by using the system to study single round, turbulent jets, and the interaction between pairs of parallel turbulent jets. Full field jet concentration data measured using the image processing system has been combined with laser doppler anemometer measurements of the jet momentum field to develop a simple model to describe the interaction between two jets. This section demonstrates the present capabilities and some future extensions of the concentration measurement system.

Chapter 6, the final chapter of the thesis, reviews what has been learned, discusses the limitations of the present system, and makes some suggestions for future research directions. It is hoped that this thesis will be helpful in exploring the world of flow visualization image analysis.

Chapter 2 - Flow Visualization

2.1 Background and Overview

Flow visualization has long been used by workers in fluid mechanics. Reynolds (1883) used filaments of dye in water flowing in a glass pipe to determine the point of transition from laminar to turbulent flow. The same principle of using dye in water or smoke in air has long been used to visualize the qualitative behavior of jets and buoyant plumes. However, the use of opaque visual tracers obscured much of the flow. For example, only the outer surface of a jet dyed in this manner is visible, and the observer cannot determine any information about the inner structure of the jet. Despite this drawback, this method is still used today. For example, Huber and Arya (1989a, 1989b) extracted quantitative information about the wake behind building models by visualizing the flow with smoke released in the wake, and observing only the large scale structures of the wake. Although these experimenters used digital image processing to extract quantitative data, the complexity of dealing with the large amount of information in an entire flow field forced them to limit their analysis to single "strips" perpendicular to the wake.

Hesselink (1988) reviewed other traditional methods used to visualize flows such as shadowgraphy, schlieren photography and interferometry. These methods use variations in the index of refraction, integrated along the path line of the illuminating light, to visualize the flow. The resulting reduction in the degrees of freedom precludes the examination of spatial structures except in the simplified case of two dimensional flows. Most of these rather sophisticated techniques are thus unsuitable

for analysis using digital image processing. An exception to this, however, is Hernan and Jimenez (1982), who were able to extract quantitative structural information from shadowgraphy ciné film of a quasi-two dimensional turbulent mixing layer between two gases with different densities. Interestingly, the experimental apparatus was the same used by Brown and Roshko (1974) in the landmark paper on large scale structures in turbulent mixing.

Internal structure can be studied if the axisymmetric plane of the jet or plume is illuminated with a thin sheet of light, usually generated by a laser. The jet fluid is seeded with a tracer that will scatter or emit light when illuminated, but will be almost transparent when not in the sheet of light. This technique overcomes many of the limitations imposed by using opaque tracers for flow visualization, and, if care is taken, allows simultaneous, quantitative concentration measurements over the full field of view. Long *et al* (1981, 1983), and Vranos and Liscinsky (1986, 1988) used gas jets seeded with small ($1\ \mu\text{m}$ diameter) aerosol particles to scatter the laser light - a process known as Mie scattering. Another technique is to use the process of Rayleigh scattering, which scatters the light off the gas molecules directly. This method was used by Escoda and Long (1983). Mie scattering is more effective at scattering the illuminating light, but exhibits noise and resolution problems due to the finite number of large (on a molecular scale) tracer particles in the flow. Rayleigh scattering does not have these problems, but since it is a much less efficient means of scattering light, extremely high intensity light (such as that from a pulsed laser) must be used. In addition, the gas must be well filtered to remove any suspended

particles and prevent undesirable Mie scattering. Both of these methods scatter the laser light without shifting its wavelength, so only the concentration of a single tracer can be measured.

The flow visualization technique used in this study was laser induced fluorescence (LIF). LIF is a technique that can be used for flow visualization and concentration measurements in gas and liquid mixing experiments, as well as in combustion studies and overcomes many of the problems of the previously mentioned techniques. Long *et al* (1983) used LIF in concentration measurements of acoustically forced gas jets. Since their tracer (iodine vapor) was mixed at the molecular level, molecular diffusion effects could be monitored if the light sheet was thin enough and the data acquisition optics had high enough resolution. LIF has been used extensively in combustion research to measure reaction species concentration, map temperature fields, and even infer velocity, pressure and vorticity distributions. An overview of these techniques can be found in Manson (1986) or in Kychakoff *et al* (1987).

Laser induced fluorescence in liquid mixing experiments can be accomplished by using fluorescent solutions mixing with clear water. The flow can be illuminated with either a sheet (for full field measurements) or a single beam of laser light. This technique has been used with some success over the last decade. Mixing layers were investigated by Koochesfahani and Dimotakis (1985, 1986), turbulent jets by Dimotakis *et al* (1983), Dahm and Dimotakis (1987), Walker (1987), and Shlien (1988) and channel flow by Walker (1989).

Some of the advantages of using fluorescent dyes in liquid mixing experiments were discussed by Shlien (1988):

- They are detectable at extremely low concentrations.
- They are almost completely transparent except where stimulated with appropriate wavelength light.
- Their intensity variation is almost linear over a 3 order of magnitude concentration range.

As discussed in section 5.2, fluorescent dyes absorb laser light and then emit light at a different wavelength. Different dyes emit at different wavelengths, and this property can be exploited to measure the concentration of more than one scalar in a mixing experiment. For example, the interaction between two parallel round jets can be studied by dyeing each of the jets with a different color fluorescent dye.

The most common source for light sheet generation is a laser. Light from a laser is extremely intense, is usually monochromatic or confined to just a few wavelengths, and remains coherent over large distances. Common types used in this type of flow visualization are argon-ion continuous wave (cw) lasers and high power pulsed lasers. Laser light sheets can be produced using several methods, the two most common being scanning mirrors and cylindrical lenses. A single beam of light can be scanned rapidly back and forth using a rotating or galvanometer-controlled mirror. The beam must be moved back and forth rapidly enough that it illuminates the entire field of view at least once while the viewing camera's shutter is open. The second method for generating sheets of light is to pass the laser beam through a

cylindrical lens, causing the beam to fan out in one dimension only, forming a sheet as shown in Figure 2-1. The Gaussian intensity distribution across the original laser beam is also spread by the cylindrical lens, so this type of sheet generally has a non-uniform light intensity cross section as well. Light sheets created with scanning methods have a more uniform intensity cross section, but the associated mirrors and scanning electronics are more difficult to align than the extremely simple cylindrical lens sheets. Because of their simplicity, cylindrical lenses were used for this study. As will be shown in Chapter 4, the Gaussian light intensity distribution can be corrected for.

2.2 Lasers, Fiber Optics and Laser Sheet Lighting

For safety and convenience, a fiber optic light sheet delivery system was developed, similar to one described by Koga, *et al* (1987). The use of fiber optics to transport the laser light eliminates the need for carefully aligned mirrors to position the beam, and greatly reduces the possibility of the operator being injured by the exposed high power beam.

The laser used was a Coherent Innova 70, a 4 watt argon-ion cw laser operating in multiline mode, producing light at wavelengths of 488 nm and 514.5 nm (blue-green). Its output beam was split into two beams using a 50/50 dielectric mirror beam splitter. In the initial system developed, the two beams were directed into the ends of 200 μm diameter multimode fiber optic cables. Microscope objectives (40 x) were used to focus the Gaussian intensity beams (≈ 1.2 mm diameter) down to "waists" smaller than the fiber diameter. The ends of the fibers were

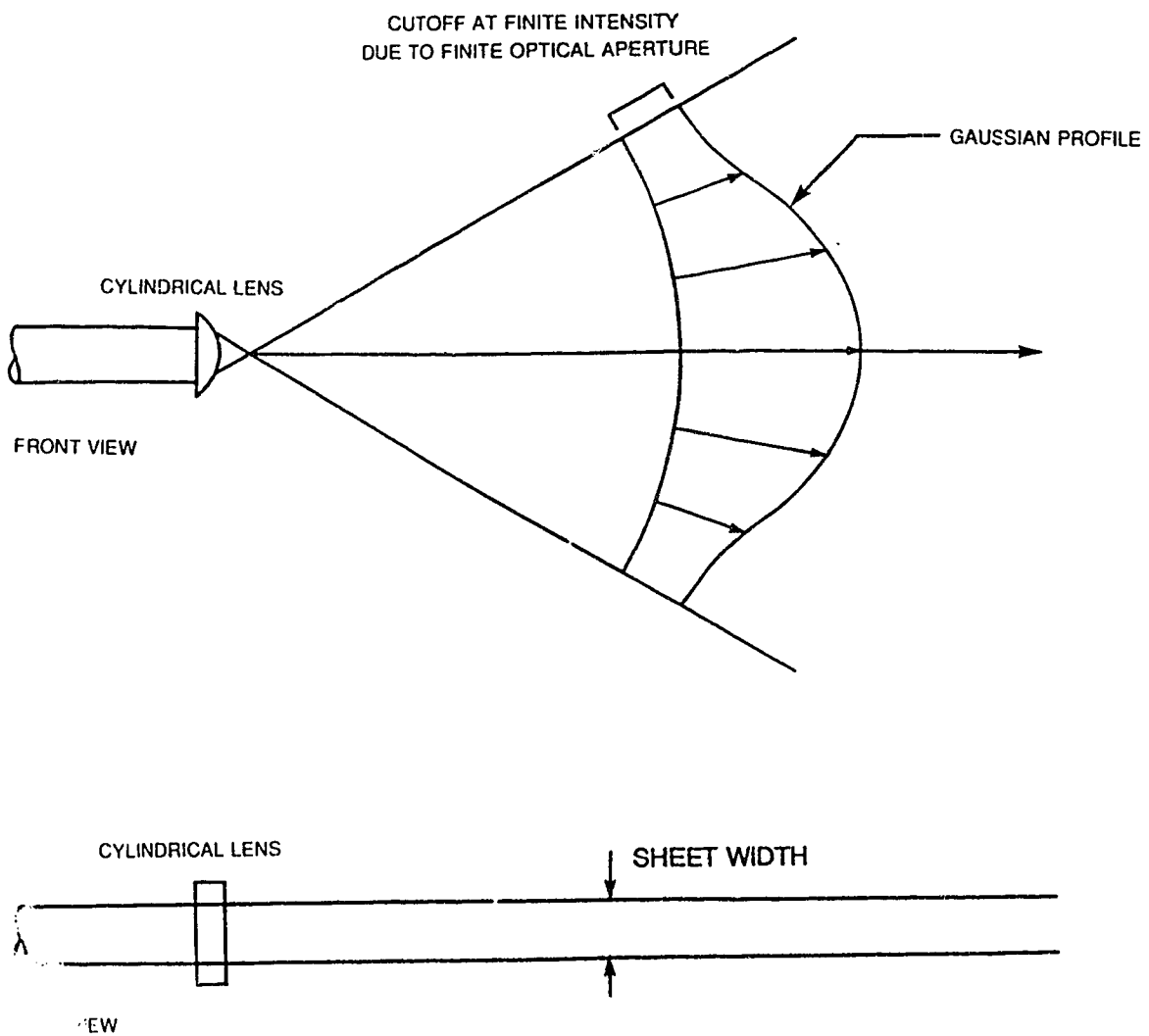


Figure 2-1: Cylindrical lens causes Gaussian beam to expand in one direction only.

positioned at these waists using precision fiber positioners. The fiber had two types of end terminators, bare, cleaved fiber ends or polished, epoxied couplers. Although the ends with epoxied couplers were more durable, the process of epoxying and polishing the ends was extremely laborious and the polished ends had poorer transmission efficiencies than cleaved bare fiber. Cleaving is a simple operation; smooth fiber ends are produced by breaking the fiber after nicking its edge with a carbon steel blade. The fiber optic input assembly schematic is shown in Figure 2-2. With careful alignment and clean fiber ends and optics, total transmission efficiency from the laser through the input optics, along 10 m of cable and out the output surface was about 65%.

Light emerged from the output end of the fiber as a rapidly expanding cone whose included angle was determined by the fiber numerical aperture. This beam of light had to be collimated again before it could be used. If the end of the fiber was a true point source of light, the collimation could be accomplished with a single spherical lens. However, the finite size of the fiber end requires the use of another 40 x microscope objective and two long focal length (100 mm and 300 mm) spherical lenses to convert the fiber output into a slowly converging beam. The 100 mm lens was placed closest to the microscope objective while the 300 mm lens was placed about 40 cm further away. The exact positions of the spherical lenses were determined by trial and error to produce a reasonable compromise between waist diameter and diameter variation. The output beam in this case converged to a waist diameter of approximately 6 mm, 1.2 m from the end of the output optics. Placing a

OPTICS MANUFACTURED BY NEWPORT OPTICS

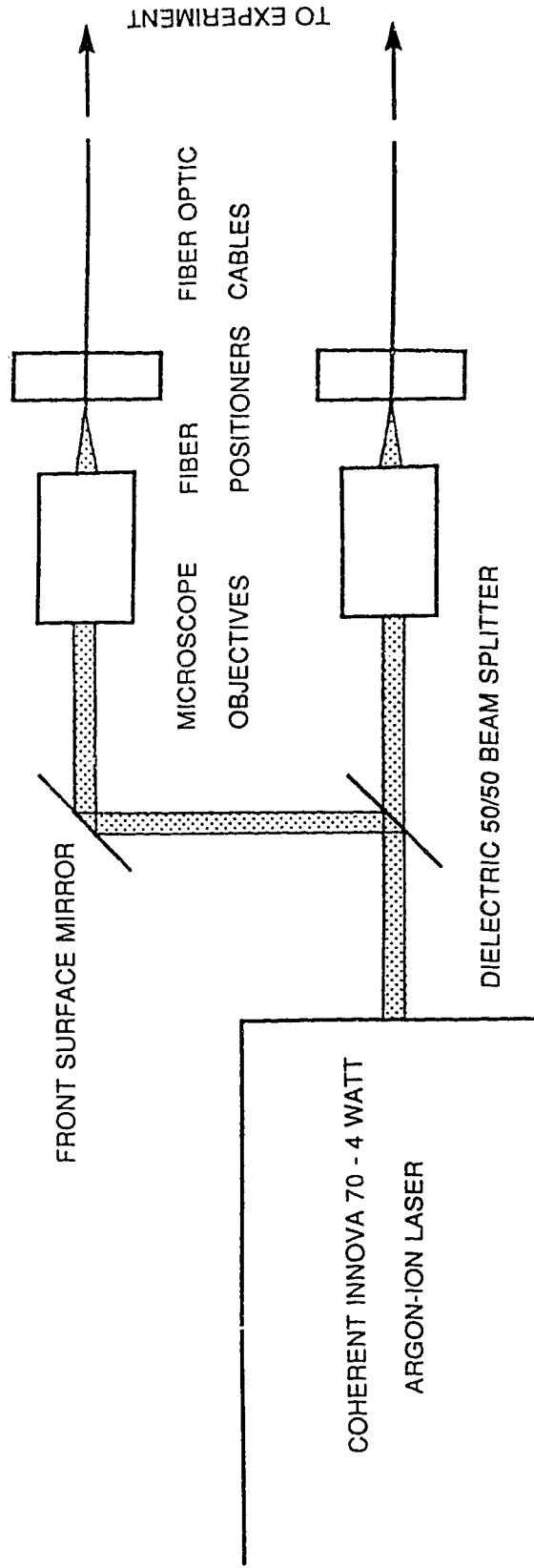


Figure 2-2: Input optics for coupling a single laser beam into two fiber optic cables.

cylindrical lens of 10 mm focal length after the second spherical lens spread the converging beam into a sheet of laser light. The waist diameter of the output beam produced the thinnest part of the resulting light sheet (6 mm), as shown in Figure 2-3. The output optics used can be seen in Figure 2-4.

As will be discussed in Chapter 3, the thinnest possible light sheet is desired, both to improve the spatial resolution and to reduce the maximum possible positional error of the image acquisition and processing system. In an effort to reduce both the minimum sheet thickness and the variation in sheet thickness, a second system was developed using 50 μm core diameter fibers. This system required changing the input microscope objective from 40 x to 20 x, but still used the same output optics, again adjusted through trial and error to produce the most collimated beam. The minimum sheet thickness using these smaller diameter fibers was found to be approximately 1.5 mm, increasing to approximately 3 mm over a distance of ± 500 mm on either side of the sheet waist. The sheet minimum thickness was located about 2000 mm from the output optics. Overall transmission efficiency of this system approached that of the first, approximately 60% - 65%. Further reductions in fiber diameter were not attempted, owing to the perceived difficulty in coupling high power laser light into smaller diameter fibers. This second system was used to collect all data presented in this thesis.

The fiber optic system allowed the generation of two sheets of light from a single laser. These sheets could be used to illuminate two different planes in a mixing experiment simultaneously. However, in this study they were used to illuminate the

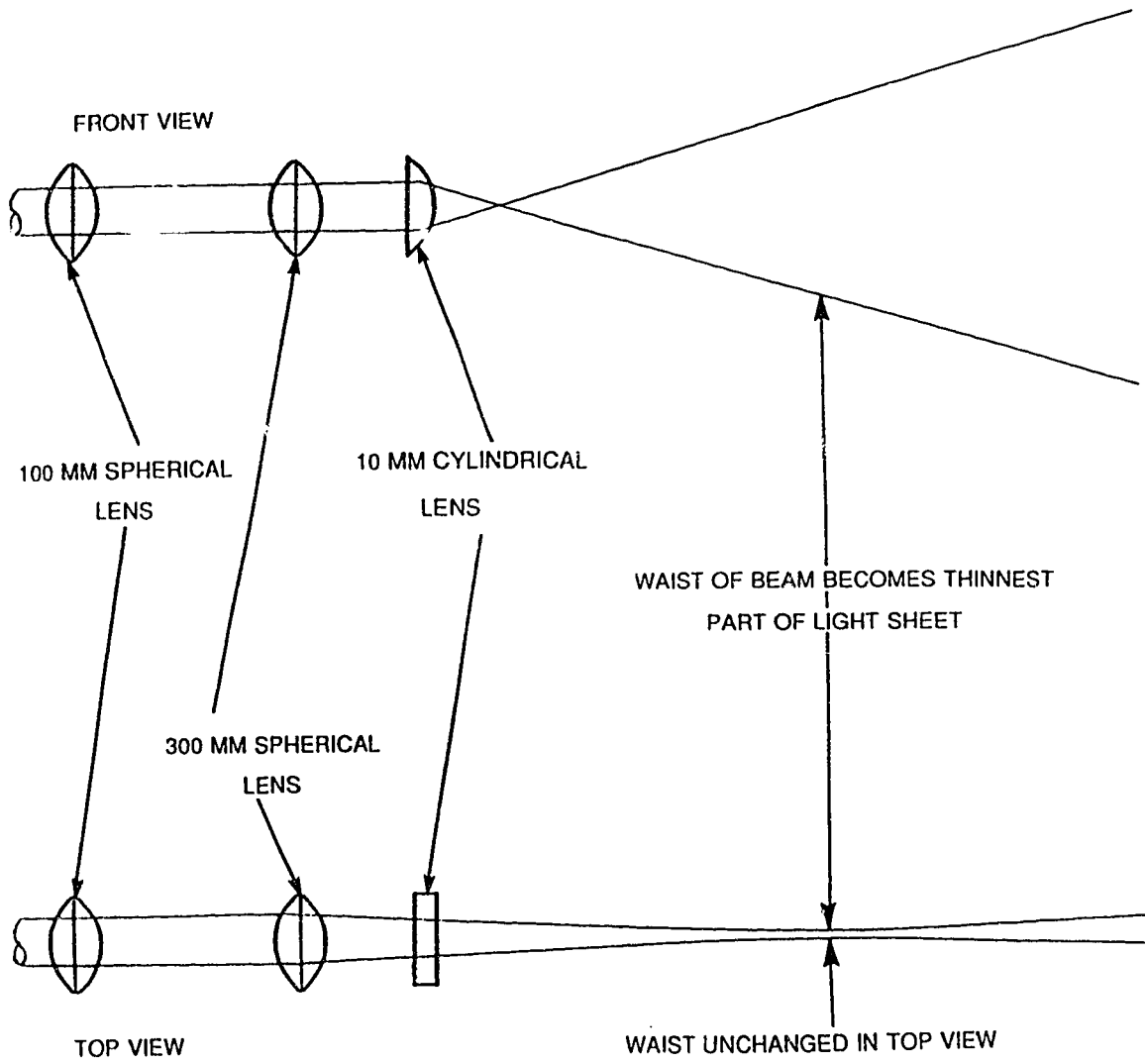


Figure 2-3: Output beam waist becomes thinnest part of resulting light sheet.



Figure 2-4: Photograph of output optics for 50 μm cables.

test section of the experiment more uniformly by shining them into the test section from opposite sides of the flow apparatus. The two sheets were aligned to illuminate only the plane of the pair of nozzles for the jets being studied, as shown in Figure 2-5.

2.3 Laser Induced Fluorescence

For an introduction to fluorescence, see the brief overview in Walker (1987) or the more in-depth coverage in Guilbault (1973). Fluorescence occurs after an outer electron of the fluorescing atom is excited by light absorption and jumps from its ground state to a higher energy, excited state. If the excited atom returns to its ground state from a lower vibrational level than it was initially raised to, light is emitted at a different wavelength than that originally absorbed. This shift in light wavelength between absorption and emission characterizes fluorescence, and can be useful in allowing the background laser light to be filtered out of images using common color filters, such as the Wratten type manufactured by Kodak. Scattered laser light was not a problem in this study, and color filters were not used in acquiring the data presented here.

The two dyes used in this study were disodium fluorescein and rhodamine 610 (also known as rhodamine B). The light from an argon-ion laser is blue-green in color, with about 40% of its power at 488.0 nm (blue) and about 30% at 514.5 nm (blue-green). The remainder of the power is distributed over several low power lines from 457.9 nm to 528.7 nm. When stimulated with argon laser light, disodium fluorescein emits light from about 530 nm to 580 nm, with peak power at approxi-

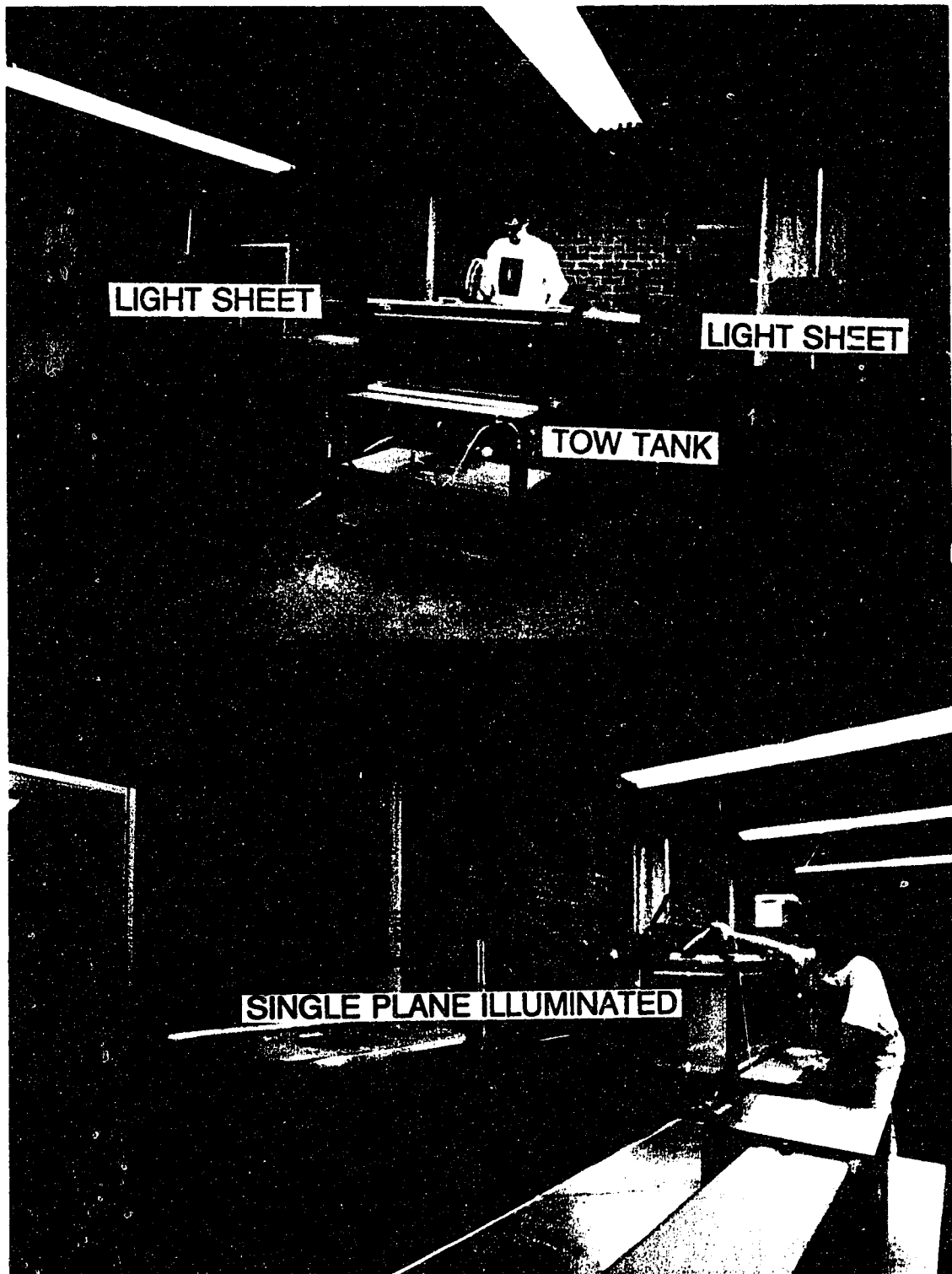


Figure 2-5: Photographs showing how two light sheets illuminated a single plane in the tow tank.

mately 550 nm (yellow-green). When stimulated with the same light, rhodamine 610 emits light at wavelengths from about 600 nm to 680 nm with peak power at a wavelength of approximately 630 nm (orange-red).

As described by Walker (1987), the intensity of light emitted by a fluorescent dye depends on several factors:

- dye concentration.
- stimulating light intensity (laser sheet power per unit area).
- solution chemistry (pH).
- dye temperature.

Fluorescent light intensity varies with dye concentration. This property was used to estimate full field dye concentration distribution from flow visualization intensity distribution. Unfortunately, fluorescent intensity also depends linearly on laser light sheet intensity, over the range of intensities used here. As mentioned above, the light sheets generated by cylindrical lenses are approximately Gaussian in cross section intensity, and also decrease in intensity as the sheet spreads with distance from the lens. Because illumination from the two light sheets is not constant, elaborate image manipulation was needed before concentration information could be extracted from flow visualization images. However, by illuminating the interacting jets with two light sheets, the light intensity over the region of interest was kept reasonably constant, and the correction complexity minimized. The image manipulation associated with light sheet non-uniformity correction is discussed in detail in Chapter 4.

The concentration of fluorescent dye used in the tagged jet fluid must be high

enough to be detectable by the camera recording the experiment. At high concentrations, however, the dye absorbs too much of the incident laser light sheet power, causing uneven light intensity over the test section. This problem is discussed in greater detail in Chapter 5. It is sufficient to note here that a reasonable compromise was found to be a disodium fluorescein concentration of $1 \cdot 10^{-6}$ mol/liter.

Because of the relatively inefficient fluorescent emission of rhodamine 610 compared to disodium fluorescein, it was difficult to record intensity distributions of both dyes in the same experiment when used at the same concentration. One dye or the other would fall outside of the dynamic range of the video camera or 35 mm film. An effort was made to increase the intensity of the rhodamine by using higher concentrations of rhodamine than fluorescein.

To set the ratio of concentrations, a simple experiment was performed by viewing jets of varying dye concentration discharging into clear water. The jets were illuminated by the same argon light sheets (power and position held constant) and viewed by a Hitachi RGB video camera connected to the digital image processing equipment manufactured by Data Translation. This equipment, discussed in Chapters 3 and 4, can be used to evaluate light intensity in an image. Just outside of the jet discharge nozzle, the dye concentration is still constant because it has not yet mixed with ambient fluid. The intensity of light emitted by the undiluted dye in this region was measured using this equipment and led to the adoption of a 5:1 rhodamine 610 to disodium fluorescein concentration ratio, or $5 \cdot 10^{-6}$ mol/liter rhodamine concentration. The purpose of this test was not to match the intensities exactly, but rather to

get them close enough to each other to be used in the same mixing experiment.

As shown by Walker (1987), the fluorescence of disodium fluorescein is strongly pH dependant below a pH of 8.0, dropping off sharply as the solution becomes more acidic. Above a pH of 8.0, the fluorescence is independent of acidity. This property has been used by Dahm and Dimotakis (1987) to investigate isothermal reacting jets. However, in this investigation, the pH of all jet and ambient fluid in the mixing tank was held at 9.0 by using a dilute buffer solution of ammonium hydroxide and boric acid. Approximate buffer solution concentrations were $2.4 \cdot 10^{-3}$ mol/l ammonium hydroxide and $1.2 \cdot 10^{-3}$ mol/l boric acid.

Walker (1987) also investigated the effects of dye temperature on the fluorescence of disodium fluorescein showing that the fluorescence intensity decreased by about 6% as dye temperature increased from 24°C to 44°C, a slope of 0.3% per °C. Guilbault (1973) states that rhodamine 610 has a much larger temperature dependence of approximately 5% per °C. In the present study water was stored in a 1000 liter container in the lab to reach room temperature and to remove dissolved air. All experiments in the current investigation were carried out with all fluids at $22 \pm 2^\circ\text{C}$ (room temperature). Variations in this range have a $\pm 0.6\%$ effect on disodium fluorescein fluorescence, and a $\pm 10\%$ effect on rhodamine fluorescence. This effect may have been seen from test to test, but within any one test, the temperature was considered constant. As shown in detail in Chapter 4, dye fluorescence in each individual test was normalized so as to eliminate the test-to-test variation in temperature.

Chapter 3 - Introduction to Digital Image Processing

3.1 Background and Overview

A digital image is visual data which has been discretized for storage and manipulation by a digital computer. The image is usually discretized spatially into a two dimensional array (memory buffer), of intensity levels for a monochrome image, or three arrays of red, green and blue intensity levels for a color image. Digital image processing is generally used to enhance visual data for one of two purposes. It can either be altered to improve human perception of the image or to aid computer extraction of quantitative information.

Digital image processing was initially developed to recreate and enhance video images generated by remote sensors in space and transmitted to Earth. As a tool for the analysis of flow visualization pictures, digital image processing has been used extensively over the last decade in many different experimental regimes. A good overview of work done in this area is contained in Hesselink (1988). Specific examples of data extraction using image processing in flow visualization are discussed in Chapter 4.

The concentration of a single scalar tracer in mixing experiments can be determined from an intensity-only image, and as a result almost all image processing used in flow visualization has been based on monochrome, intensity-only images. The colorimetric information available in visual data is usually ignored. A good example of utilizing color information, however, was shown by Armstrong and Vosen (1990), who performed an interesting experiment where the presence of an intermediate

reaction product (NO_2) was detected by examining the resulting color of white light after it has passed through burning liquid propellant.

Before the techniques developed for analyzing flow visualization images can be discussed, an overview of the subject of color digital image processing is needed.

3.2 Intensity-Only, RGB, and HSI Images

An intensity-only digital image is a "black and white" image which has been digitized at many points corresponding to an array of rows and columns known as an image buffer. Each element in the buffer contains a number representing the light intensity level, called a grey level, at that point in the original image. This grey level can vary from totally dark to fully bright. In digital systems, a fixed number of grey levels exist between these limits, set by the number of bits of memory used for each element in the buffer. The Data Translation system used in this study was an 8 bit image processing system with an intensity resolution of 256 grey levels between fully dark and fully bright.

Visual information possesses more information than just intensity, however. The wavelengths of light between about 400 nm to 700 nm are seen by humans as different colors of light. Because of the way that light is interpreted by humans, almost all perceived colors can be generated by a mixture of red, green, and blue light, the so-called "primary" colors. This physiological quirk is used in color television systems as a means of quantifying and reproducing color in visual data. The sensor in a video camera looks at the visual data through three filters which transmit only red (≈ 650 nm wavelength), green (≈ 530 nm) and blue (≈ 460 nm) light.

These three images can be treated as three intensity-only images. They can be used to stimulate the appropriate red, green, and blue phosphors on a color cathode ray tube to produce what appears to be a full color image to the human eye. A good introduction to color television and color mixing can be found in Kiver (1964).

One way to digitally process full color images is to digitize the red, green and blue (RGB) signals output from an RGB video camera or other source, and then store this information in three separate buffers as three separate intensity-only images. The disadvantage is that the three images are highly correlated. Most image enhancement or analysis operations must be done on all three buffers. For instance, to determine the monochrome light intensity at any point requires calculating the average value of the red, green and blue intensities at that point.

As described in Wilson (1988), a different way to work with color images is hue, saturation and intensity (HSI) processing. These three color attributes more closely approximate the way that humans perceive and think about vision. They are relatively uncorrelated compared with their RGB counterparts. This can speed computer enhancement and analysis of color images because many operations only have to be performed on one or two of the three buffers. Because the HSI processing system closely corresponds to human perception, it is easier to predict the necessary operation to give a certain image correction.

Hue is an attribute which describes what humans generally think of as "pure" color, such as red, yellow, green, blue, purple, etc. Saturation is an attribute which describes color purity, or the degree to which the color is not diluted with white. For

example, pure red (100% saturated) becomes pink when mixed with white light. Saturation can be thought of as the inverse of the white light content in a color. The third attribute, intensity, is the light level of the color - it is identical to the intensity level in the above discussion of monochrome images.

The functions relating RGB attributes to HSI attributes, from Wilson (1988), are:

$$I = \frac{R+G+B}{3} \quad (3.1)$$

$$H = \frac{1}{360^\circ} \cdot [90^\circ - \tan^{-1} \left(\frac{1}{\sqrt{3}} \cdot \left[\frac{2R-G-B}{G-B} \right] \right)] \quad (3.2)$$

+ (0°, G ≥ B; 180°, B ≤ G)]

$$S = 1 - \left(\frac{\min(R,G,B)}{I} \right) \quad (3.3)$$

In these three equations, R, G, and B represent red, green and blue light intensity. H, S, and I represent hue, saturation and intensity. All six parameters have values between 0 (fully off) and 1 (fully on). Digital resolution will limit the number of levels between on and off for each quantity.

A simple way to visualize the relationship between RGB and HSI is the color chart shown in Figure 3-1. Hue is represented by the angle between red (arbitrarily chosen as zero) and the color of interest. Saturation is represented by the location between the origin (pure white) and the rim (pure color). Intensity is represented by the third axis running perpendicular through the center of the cylinder. Any

intensity and color given by RGB or HSI coordinates is represented by a single point on this diagram.

3.3 Image Digitizing and Processing Equipment

Amorese and Bloomfield (1988) describe some of the different video standards used for image processing applications. The RS-170 video standard was developed to define broadcast standard black and white video signals in the United States. Images conforming to this standard consist of 525 horizontal scan lines interlaced 2:1. The odd lines in the frame are scanned in 1/60th of a second, followed by the even lines in the next 1/60th of a second for an interlaced framing rate of 30 frames per second. Each of the odd and even "fields", as they are known, consists of 262.5 horizontal lines. The last 22.5 lines of each field are not part of the image, but are used for a vertical sync signal. The full frame, therefore, has 480 lines of image information. Each of the red, green and blue intensity signals from an RS-170 RGB video camera conforms to this definition.

The broadcast standard color television signal in North America is not the RS-170 RGB definition. Rather than broadcasting three separate image signals, and to maintain backward compatibility with black and white television sets, the National Television Standards Committee's (NTSC) standard encodes the color information at a higher frequency within a single black and white RS-170 signal. This type of signal is commonly known as composite video.

The image processing system used in this study is made up of Data Translation components designed to work with either true RGB or NTSC input images in an PC-

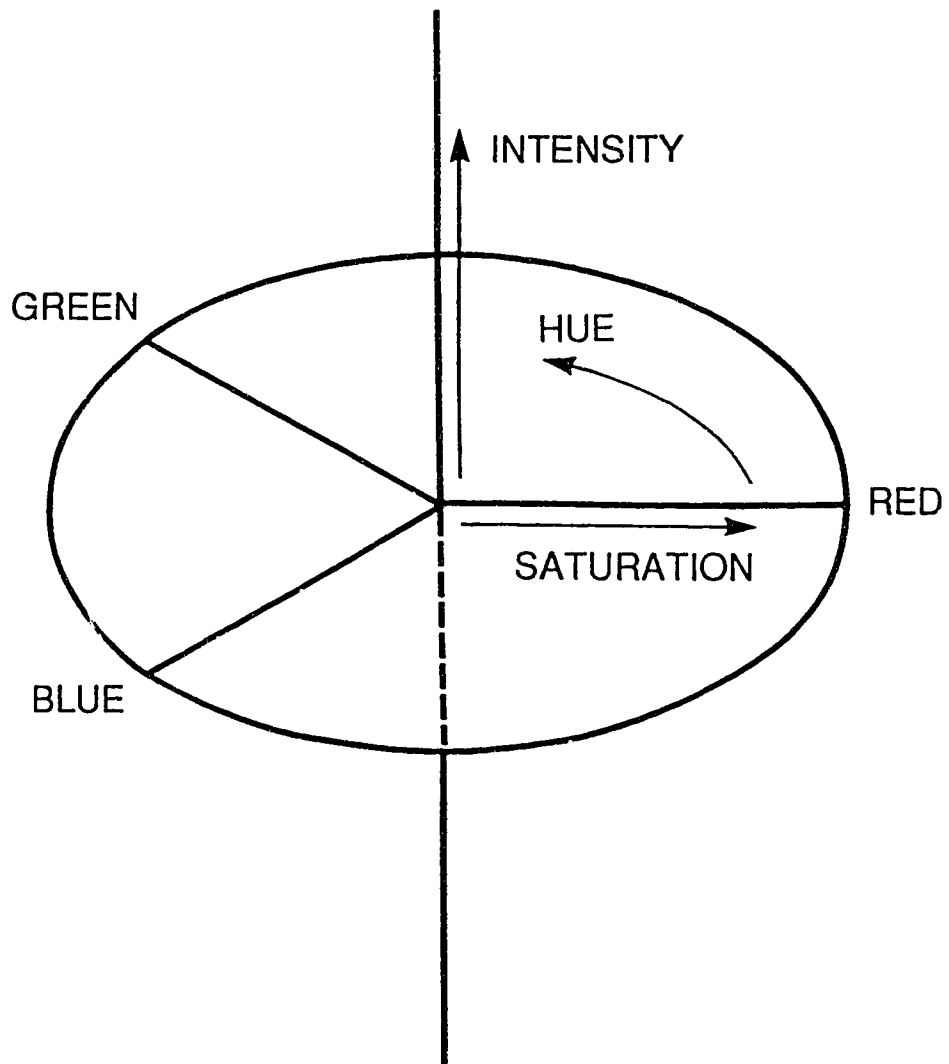


Figure 3-1: HSI color scale.

AT compatible computer. The system consists of 3 plug-in PC boards: a frame grabber, an auxiliary frame processor, and a composite (NTSC color) video to RS-170 RGB video converter board. A schematic of the acquisition and processing system is shown in Figure 3-2.

The frame grabber, a Data Translation model DT2871, is designed to work with full color RS-170 RGB television standard images. It is capable of digitizing an analog television frame in real time (ie: in 1/30th of a second) and converting it from RGB to HSI for processing and back to RGB for display using two proprietary high speed integrated circuits. It has a spatial resolution of 512 * 512 discrete picture elements, or pixels. Since the video signal contains only 480 horizontal lines of information the last 32 horizontal lines are not used. The image is stored in 3 buffers, one each for hue, saturation and intensity (or red, green and blue if desired). Each pixel location in each buffer consists of 8 bits of storage, for a total of 256 attribute levels per buffer. Because of the standard aspect ratio of NTSC video equipment, the width to height ratio of each pixel is 4:3.

The auxiliary frame processor, a Data Translation model DT2858, is used to perform high speed integer logic and mathematical operations on single image buffers. Although it has the same spatial resolution (512 * 512), each pixel is stored with 16 bits of memory, for a total of 65,536 attribute levels. This additional storage helps prevent overflow and round-off errors from occurring on such operations as buffer additions and multiplications.

The third PC board in the image processing system, a Data Translation model

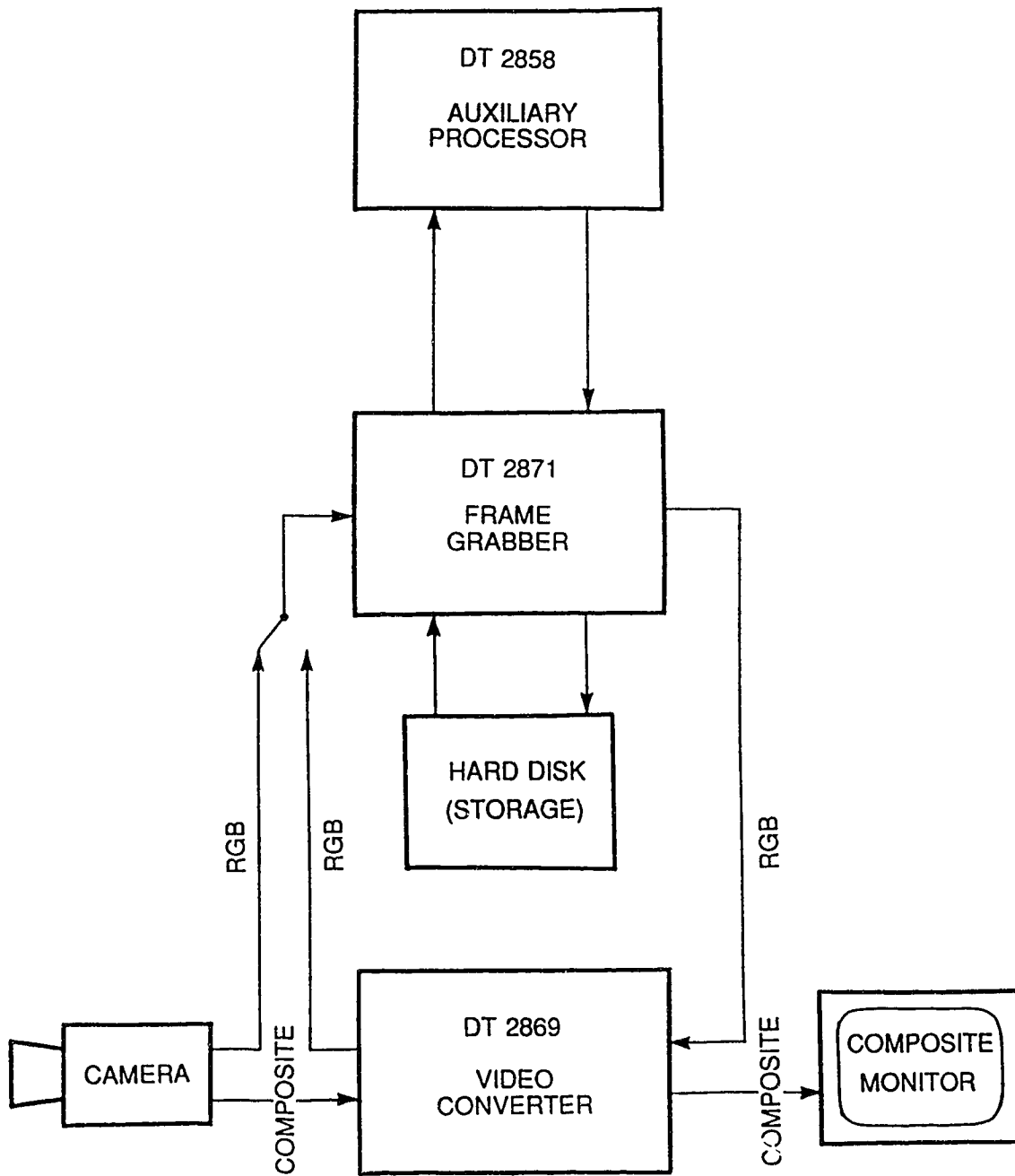


Figure 3-2: Schematic diagram of image acquisition and processing system.

DT2869, is a two channel, real time video conversion board. One channel converts NTSC composite color images to RS-170 RGB images, and the other converts RGB images back to NTSC composite. This board allows the use of composite video sources (such as standard video cassette recorders) for input or output and composite video monitors for output image display.

Images were acquired with a Hitachi VK-C360 RS-170 RGB/composite video camera. This camera has a single image sensing array chip with 760 discrete horizontal pixels by 485 vertical pixels. The image is output as both analog RGB video and NTSC composite video signals. The horizontal resolution of each line of video signal is limited by the response of the analog amplifier in the camera, specified by Hitachi as better than 430 pixels per horizontal line. The camera was used to view a test pattern of 512 black to white transitions per horizontal video line. The resulting image digitized by the frame grabber was able to follow all of the transitions along horizontal rows in the digital buffer. The digital image resolution is therefore limited only by the frame grabber to 512 horizontal by 480 vertical pixels. For the remaining discussion, the camera and the frame grabber will be considered to be a single piece of equipment because the camera output was measured exclusively with the frame digitizer.

Although the Hitachi camera had good spatial resolution, there were two serious problems with its ability to accurately digitize intensity levels. As shown in Figure 3-3, the camera/frame grabber response to light intensity from fluorescent lighting tubes was measured and found to be non-linear. These fluorescent tubes, in

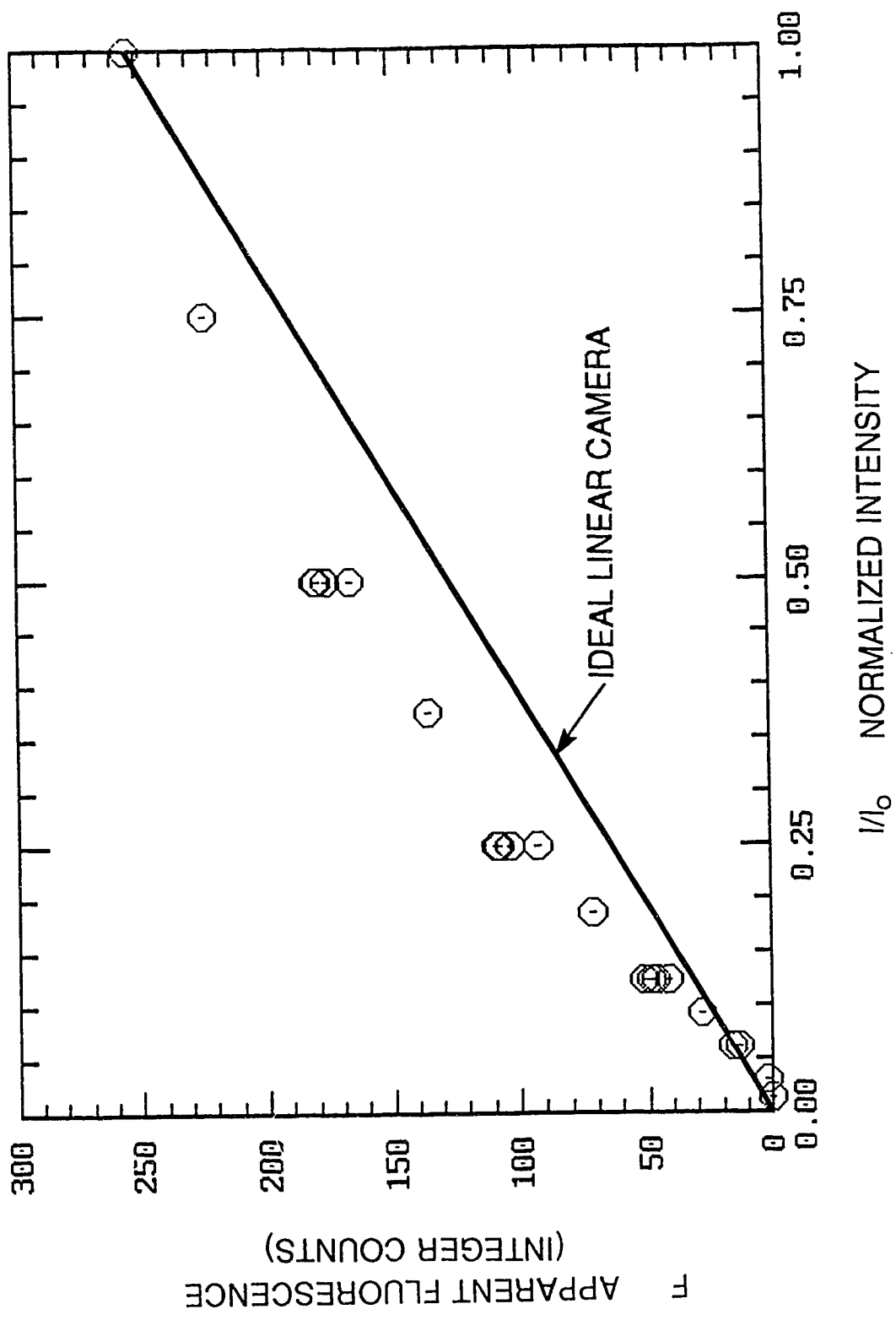


Figure 3-3: Non-linear video camera response.

the constant illumination light box described in Chapter 4, emit a multiline light spectrum which is only approximately white light. As this was the lighting used to illuminate data slides for the video camera, it was used to calibrate the intensity response of the camera. The light intensity reaching the sensor in the video camera was varied both by altering the f-stop of the camera lens and by changing the number of fluorescent tubes in the light box.

The video camera output non-linearity was corrected using the empirically determined function of Equation (3.4), shown in Figure 3-4. This function was initially determined using a least squares fit, and then modified slightly to force the function to pass through the origin. This modified function is:

$$F_{lin} = 6 \left(1 - \frac{1}{F_{meas} + 1} \right) + 0.7F_{meas} - 0.0025F_{meas}^2 + 0.000014F_{meas}^3 \quad (3.4)$$

The other problem with the Hitachi video camera was its response to a step change in intensity along a horizontal scan line. Figure 3-5 shows typical camera/frame grabber response to this type of input. The image that the system was viewing consisted of white strips of paper of varying widths arranged vertically on a black velvet background and illuminated with high intensity flood lights to provide several step changes in input intensity to the camera. Figure 3-5 shows the mean of 10 horizontal rows of the resulting image in the frame grabber's intensity buffer. Three different magnitudes of step changes are shown. The measured light intensity contained "spikes" on either side of the bright strips. The height of these spikes

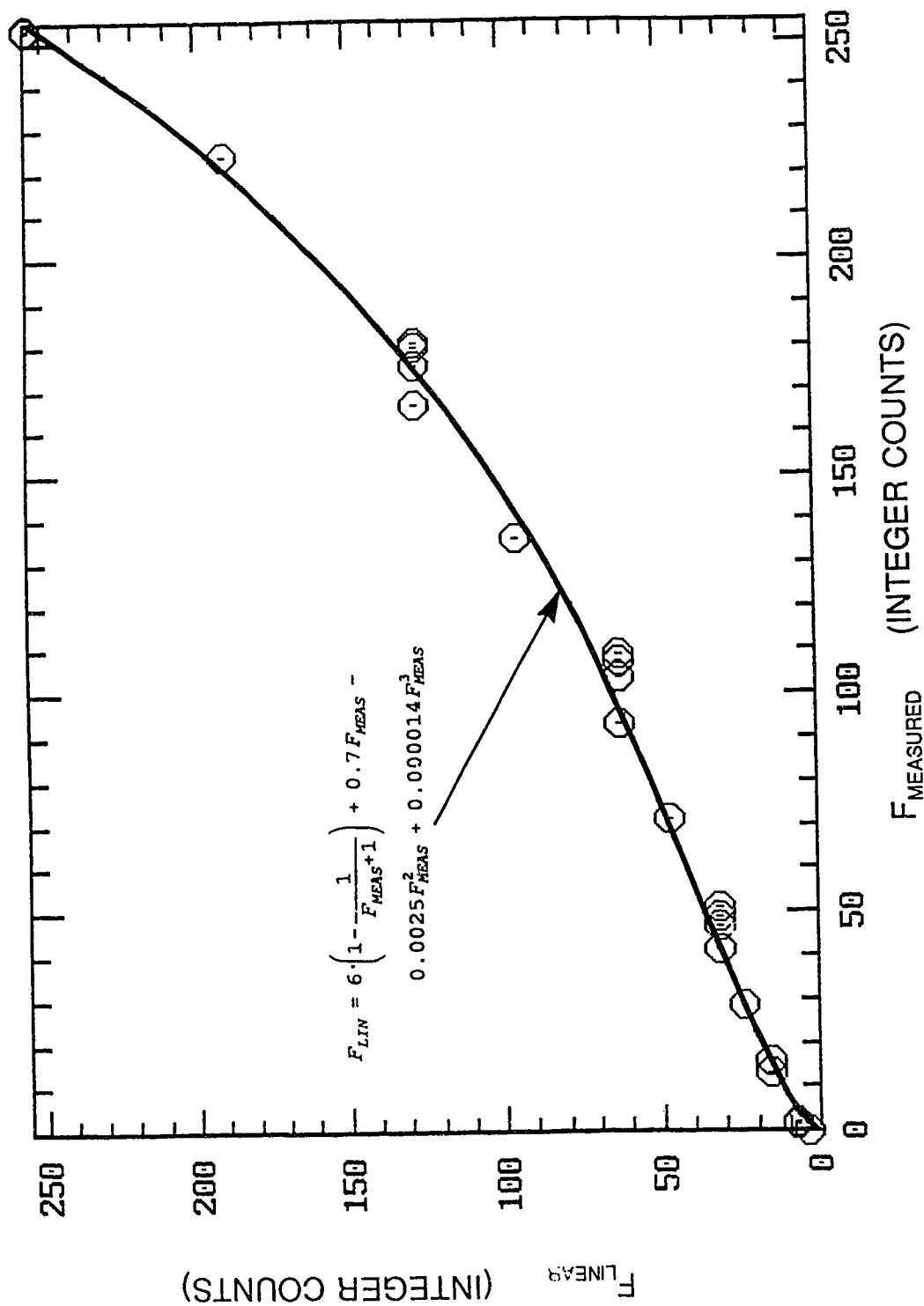


Figure 3-4: Camera linearity correction.

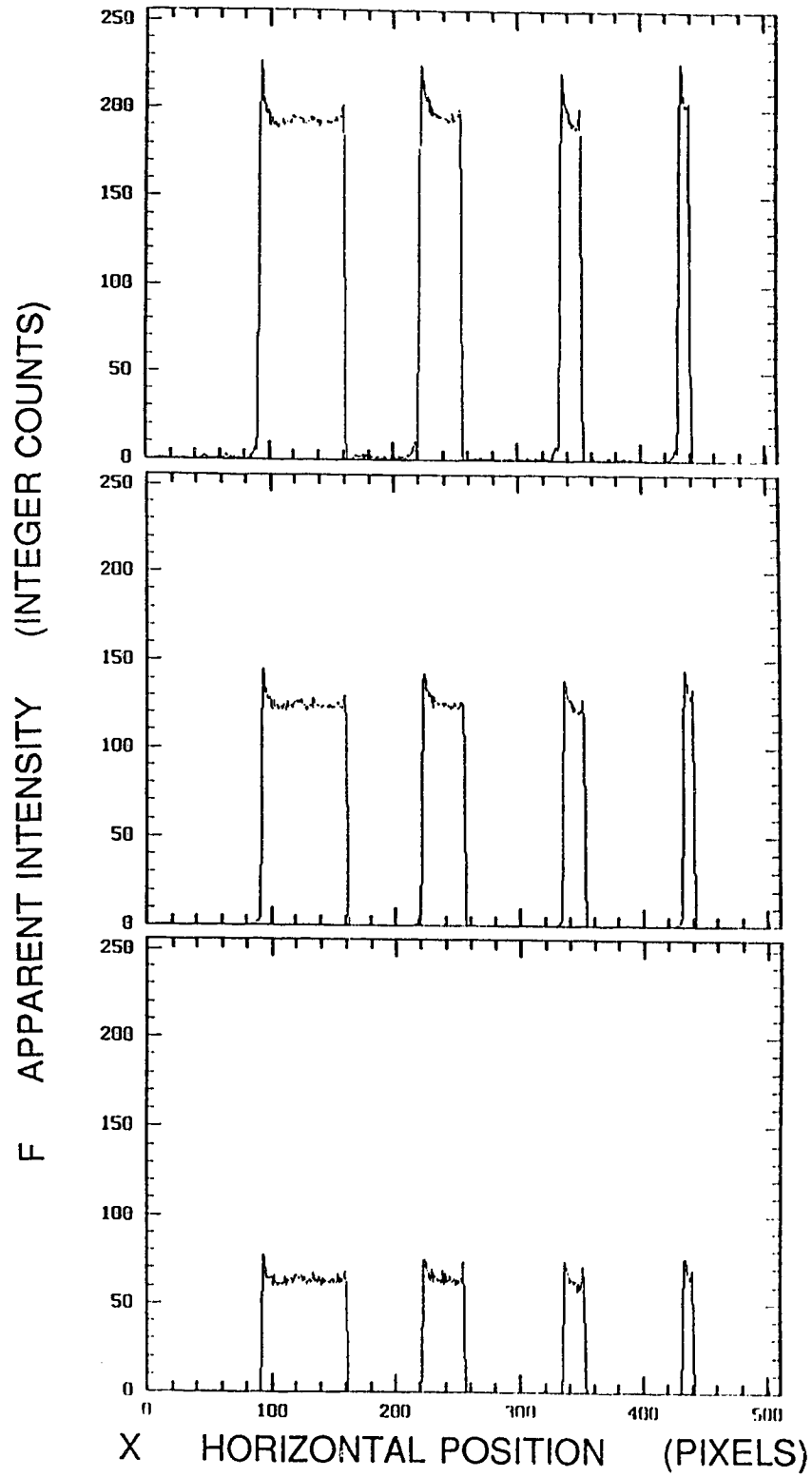


Figure 3-5: Camera response to step change in intensity. Three different magnitudes of step changes are shown.

appears to be independent of bright region width, but does appear to be a function of bright region intensity. Since the intensity buffer is the average of the red, green and blue input signals from the camera at each pixel location, the frame grabber was switched into RGB mode and the resulting RGB buffer levels for a single bright region are shown in Figure 3-6. The left hand spike appears in all 3 input signals while the right hand spike is visible only on the red input signal. These effects are produced electronically by edge enhancement hardware in the video camera coupled with irregularities in the analog output amplifiers. In the experimental images from this study, this effect only produces significant overshoot after abrupt transitions to high intensity (high fluorescent dye concentration). As will be shown in Chapter 5, step changes in intensity only occurred in the laminar regions of initially laminar jets where the concentration of jet fluid was known. Outside this initial region, turbulent mixing generally provided smoother transitions between bright and dark regions. This effect was felt not to cause significant errors and no attempt was made to correct for these spikes in the present study. It may be possible to disable or bypass the edge enhancement features of the Hitachi camera and correct these errors in future work.

Images could be acquired in one of two ways, either directly with the video camera or by using the video camera to digitize 35 mm still film slides. Images could be digitized directly from the RGB output of the video camera to computer memory. Because of the large memory requirements for full color images (786,432 bytes per image), a maximum of 4 images at approximately 1 second intervals could be digitized before they would have to be saved to hard disk. This limitation meant that

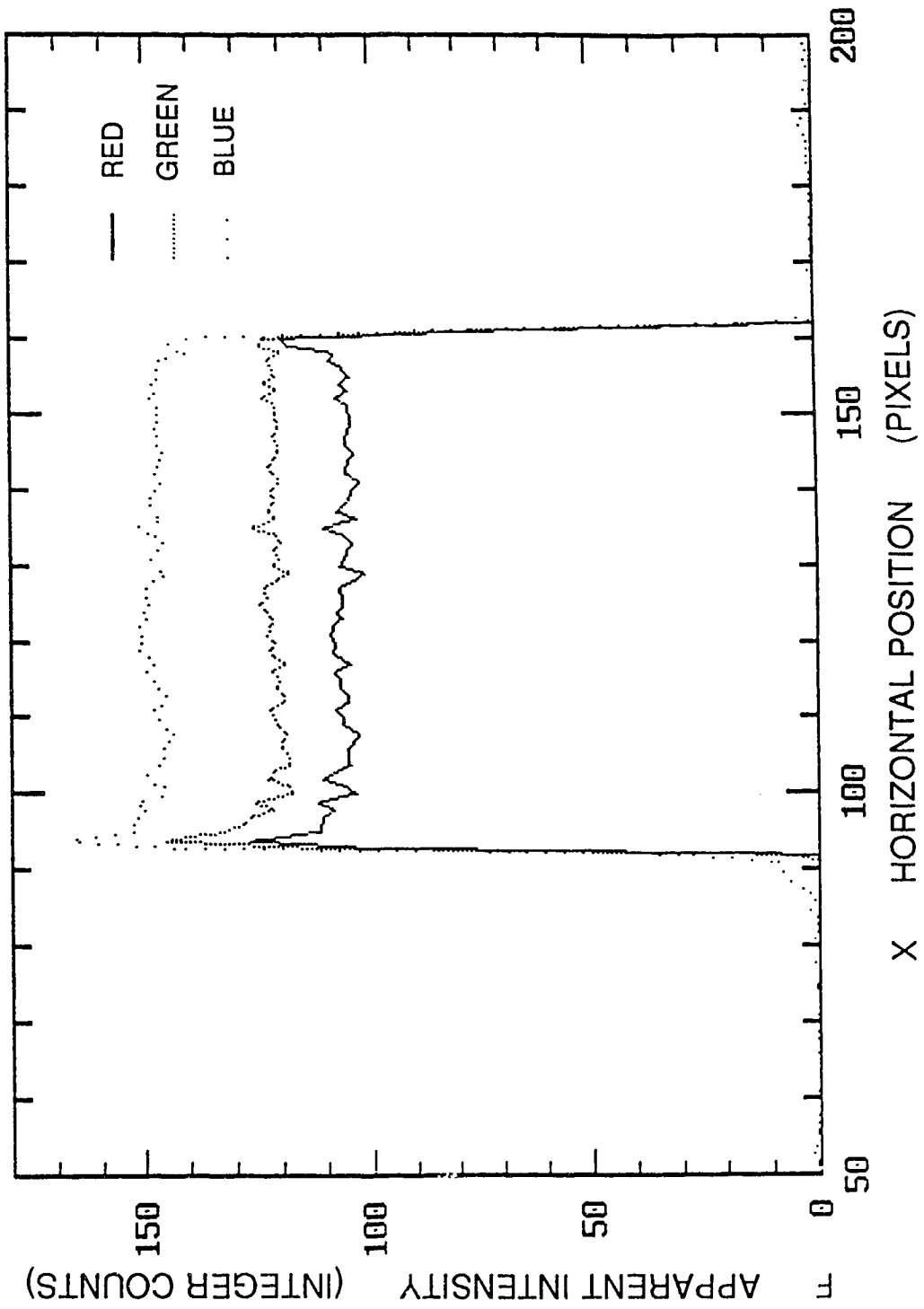


Figure 3-6: RGB response to step change in input intensity

this method was more suitable for directly digitizing calibration experiments such as constant concentration fluorescing dye tests rather than flow mixing tests. Direct acquisition with the video camera was also limited to viewing the entire flow field.

Flow visualization images were recorded using a standard Nikon 35 mm single lens reflex camera with a motor drive and a 200 mm f4 lens. The film used was Kodak Ektachrome 800/1600 ASA daylight film processed at 1600 ASA. For the turbulent jet flow visualization, an exposure time of 1/125th of a second (8 ms) and an aperture of f4 captured the images without saturating the film. The slides were digitized by illuminating them with a uniform intensity light box and viewing them with the Hitachi video camera coupled to a 50 mm focal length Nikon lens and a bellows for macro focussing. A threaded, two axis positioner allowed precision placement of the slide in the plane perpendicular to the camera viewing axis. This arrangement, as shown in Figure 3-7, allows for enlarging sections of the slide until the resolution of the slide film grain limits the image resolution. The uniform intensity light box shown in Figure 3-7 used eight fluorescent tubes inside of a large plywood box to provide indirect, uniform illumination to a small, slide-sized hole in the side of the box. The interior of the box was painted white to increase diffuse reflections. The color of the illuminating light affects the color of the slide as perceived by the image processing system. Because the illumination source was kept constant, however, the perceived colors were consistent for all slides digitized. All attenuation and jet data presented in this thesis were acquired using this slide film method.

Slide digitizing equipment and light box

Figure 3-7: Photograph of Slide Digitizing Equipment

Two mathematical operations were performed on the digitized images before further processing. The video camera average intensity response with the lens cap on was subtracted from each image's intensity to remove any small "black noise" offset in individual pixels, and the corrected image was saved to disk. Then, Equation (3.4) was applied to each pixel in the intensity buffer to correct the intensity levels for camera non-linearity. Corrections were only applied to the intensity buffer since this was the only buffer used to determine the total dye concentration field of the image.

3.4 Determining World Pixel Position and Uncertainty

Careful thought is required to extract quantitative spatial information from a digitized image. The original illuminated plane (world) coordinates can be related to image coordinates through a simple linear transformation. However, uncertainties in position arise due to finite light sheet thickness, digitizing camera and frame grabber resolution, camera shutter speed blurring and possible non-linearities in the transformations.

The coordinate system used for describing real world and digital image position is shown in Figure 3-8. The digital image and the slide image are both flat, two dimensional planes. The flow is illuminated by a light sheet of finite thickness, but it too can be modelled as a flat, two dimensional plane. Any point on this flat plane can be linearly mapped onto another plane by the transformation:

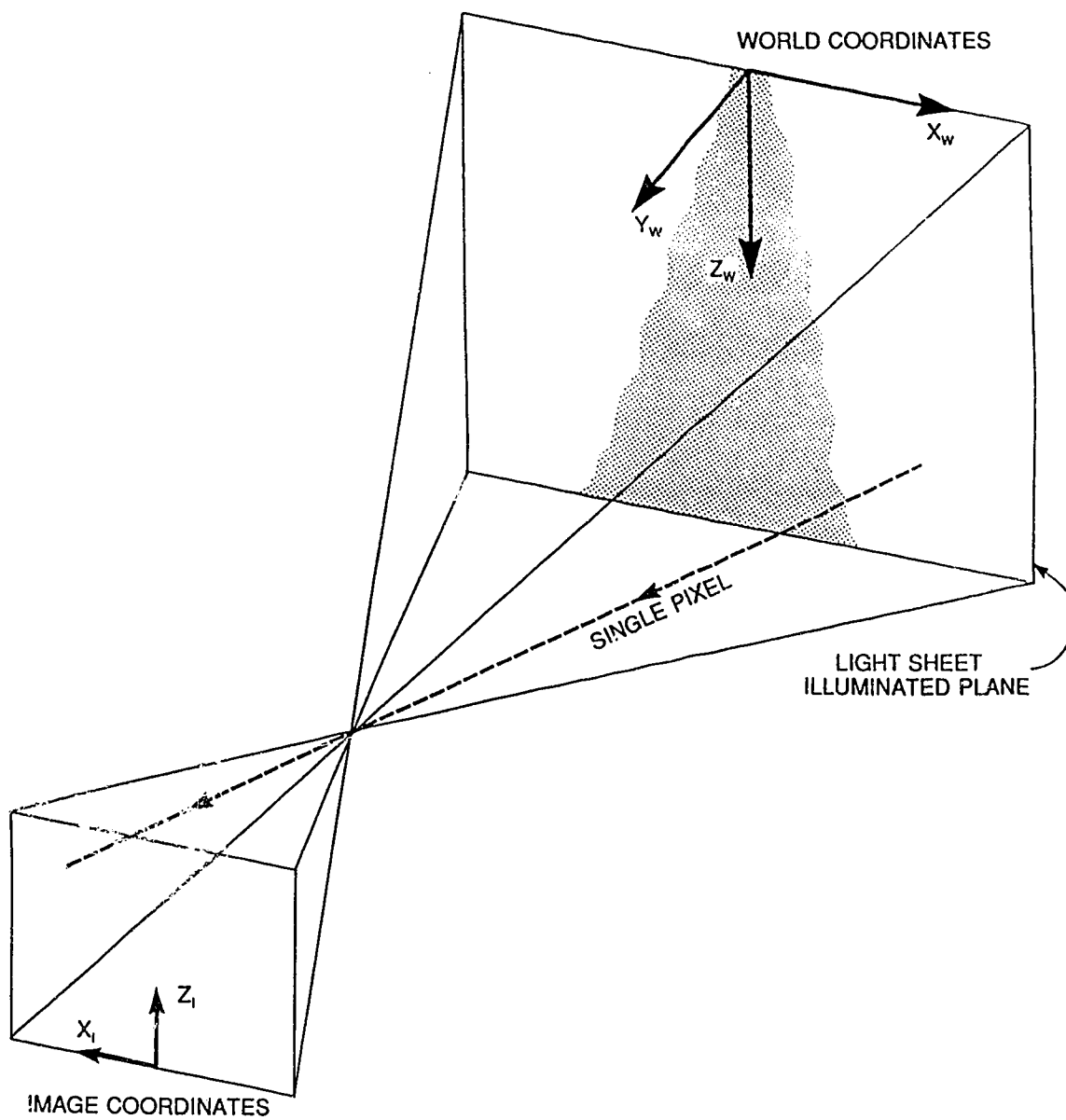


Figure 3-8: Imaging geometry: How world coordinates are related to image coordinates.

$$\begin{bmatrix} x_i \\ z_i \\ 1 \end{bmatrix} = \begin{bmatrix} a & b & c \\ d & e & f \\ 0 & 0 & 1 \end{bmatrix} \cdot \begin{bmatrix} X_w \\ Z_w \\ 1 \end{bmatrix} \quad (3.5)$$

where subscript i denotes image coordinates and w denotes world coordinates.

These homogeneous coordinates are required to allow translation between planes, as well as rotation and scaling. Translation, rotation and scaling allow the image coordinate system to be aligned with the original world coordinate system. It is evident from equation (3.5) that the overall transformation from world coordinates to film coordinates to digital image coordinates will be the superposition of two linear transforms. So, for calibration purposes, digitizing a slide is no different than directly acquiring images from the flow.

The calibration process was simplified a great deal for the present study, however, because there was no rotation between the world and the image axes. Additionally, since the original world coordinates of one point in the image were known (the end of a jet discharge tube was one such point) it was not necessary to perform the full transformation of equation (3.5). All that was required to extract spatial information was horizontal and vertical calibration scaling factors. By using scaling factors, all world coordinates were determined relative to the known point in the image. These scaling factors were determined by measuring the distances in the image (in pixels) between additional points with known real world coordinates. These

calibration constants, C_x and C_z , relate real world position to image position in the following manner:

$$\Delta X_w = C_x \cdot \Delta x_i \quad (3.6)$$

$$\Delta Z_w = C_z \cdot \Delta z_i \quad (3.7)$$

The overall pixel resolution governs the smallest structure which can be discerned from the digitized image. The horizontal and vertical resolution of the digital image will be:

$$\textit{Vertical Resolution} = C_z \cdot 1 \textit{ pixel} \quad (3.8)$$

$$\textit{Horizontal Resolution} = C_x \cdot 1 \textit{ pixel} \quad (3.9)$$

Deviations between the idealized 2D - 2D transformation and the actual image transformation can cause uncertainty in the pixel placement calibration. Finite laser sheet thickness, finite camera shutter speeds, incorrect alignment of the image and world coordinate systems and non-linearities inherent in the cameras all contribute to this uncertainty.

The laser sheet has a finite thickness, t_l , so the uncertainty in the y position of an observed fluid particle is $\pm(t_l/2)$. Since the camera recording the flow visualization picture perceives a line of sight as a single pixel, laser sheet thickness can also cause uncertainty in the perceived x and z position of the particle. As the thickness of the sheet increases, so does the uncertainty. Using similar triangles as

shown in Figure 3-9 , the uncertainty in horizontal position, ϵ_x caused by this effect is:

$$\epsilon_x = \frac{t_L X_w}{2 Y_w} = \frac{t_L x_i}{2 f} \quad (3.10)$$

Similarly:

$$\epsilon_z = \frac{t_L Z_w}{2 Y_w} = \frac{t_L z_i}{2 f} \quad (3.11)$$

where f is the focal length of the camera lens.

These uncertainties can not be systematically corrected and must be thought of as error terms. The y position of the fluid particle can not be determined to any resolution better than the thickness of the light sheet from the information contained in the image. This error is linearly related to distance from image center - the worst uncertainty is in the image corners. This uncertainty can be reduced by minimizing the sheet thickness and/or using a long focal length lens.

The two cameras used to record flow visualization images were the Hitachi video camera and the 35 mm single lens reflex camera. For error calculations, it is simpler to use the focal length of the lens and the size of the image actually formed in the camera rather than the digital image buffer. The video camera used a 50 mm

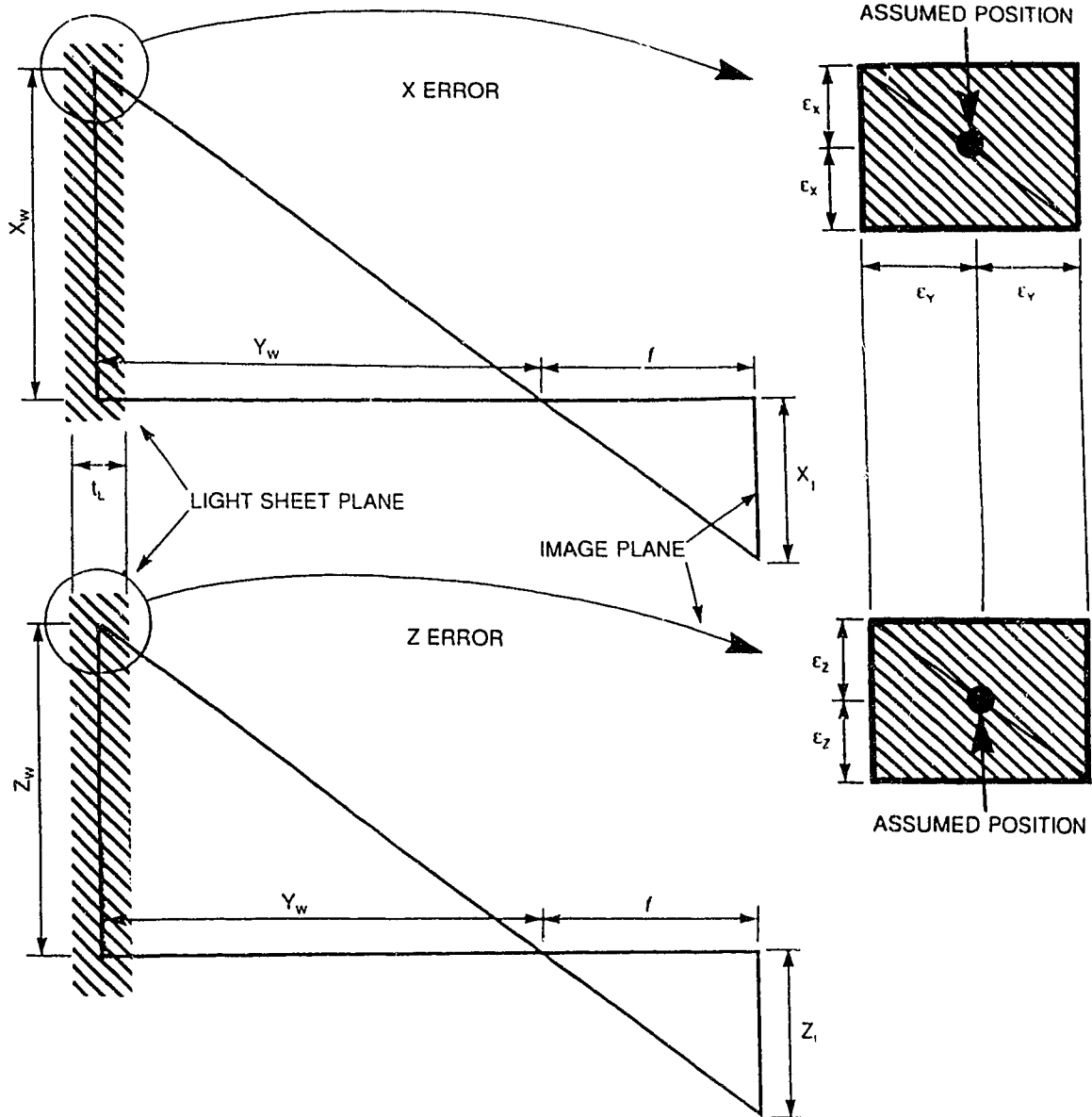


Figure 3-9: Error due to laser light sheet thickness.

focal length lens to focus the image onto an internal imaging plane 8.8 mm wide and 6.6 mm high, so that $x_{i,max} = 4.4$ mm and $z_{i,max} = 3.3$. The SLR camera used a 200 mm focal length lens to focus the image onto an area of slide film 36 mm wide and 24 mm high, so that for this camera $x_{i,max} = 18$ mm and $z_{i,max} = 12$ mm. The largest positional errors will occur in the image corners. With the present light sheet thickness of less than 2 mm over the observed area, the maximum positional uncertainties using the video camera directly were $\epsilon_x = 0.09$ mm, $\epsilon_y = 1$ mm and $\epsilon_z = 0.07$ mm. Using the SLR camera, the maximum possible errors in the corners of the imaging area were $\epsilon_x = 0.09$ mm, $\epsilon_y = 1$ mm and $\epsilon_z = 0.06$ mm. These errors are independent of the size of the viewed area. They are fixed by the focal length of the camera lens and the size of the imaging area in the camera.

Video cameras can exhibit spatial non-linear imaging errors. This type of error may also be measured in an image generated by the camera when it is viewing a test pattern consisting of a square grid. When the Hitachi camera and Nikon lens were tested for non-linearities by digitizing an image of such a grid, no non-linearities could be detected. The digital image of the square grid remained square over the entire image, within the ± 0.5 pixel resolution.

If the video camera is used to directly digitize an image of a mixing experiment, the RS-170 scanning method can cause errors. Recall that it takes 1/60th of a second to scan the even lines of a video image and another 1/60th of a second to scan the odd lines of a video image, which when interlaced make up one video frame. The particle velocity at which a particle will not "smear" into the adjacent

pixels is limited by this scanning method.

This video scanning effect is shown in Figure 3-10. The limiting velocity in all directions is either

$$V_{\text{lim}} = \frac{C_z \cdot (1 \text{ pixel})}{\left(\frac{1}{60} \text{ sec}\right)} \quad (3.12)$$

which is the frame line limit, or it is

$$V_{\text{lim}} = \frac{C_z \cdot (2 \text{ pixels})}{6.3 \times 10^{-5} \text{ sec}} \quad (3.13)$$

which is the field line limit. Typical values of C_x and C_y in this study were 1.5 mm/pixel and 1.2 mm/pixel, respectively.

The images were not digitized directly from the mixing experiment in this study, but instead were recorded with a 35 mm SLR camera on slide film. As will be shown later in Chapter 5, the 8 msec exposure time used to record the flow was fast enough to effectively freeze the fluid motion at velocities up to 15 cm/sec when analyzing frames with $Z_w = 20$ cm in the flow direction (see Figure 3-9). The distance that fluid particles or structures moving slower than 15 cm/sec could travel in 8 msec was shorter than 1 pixel when the slide was subsequently digitized.

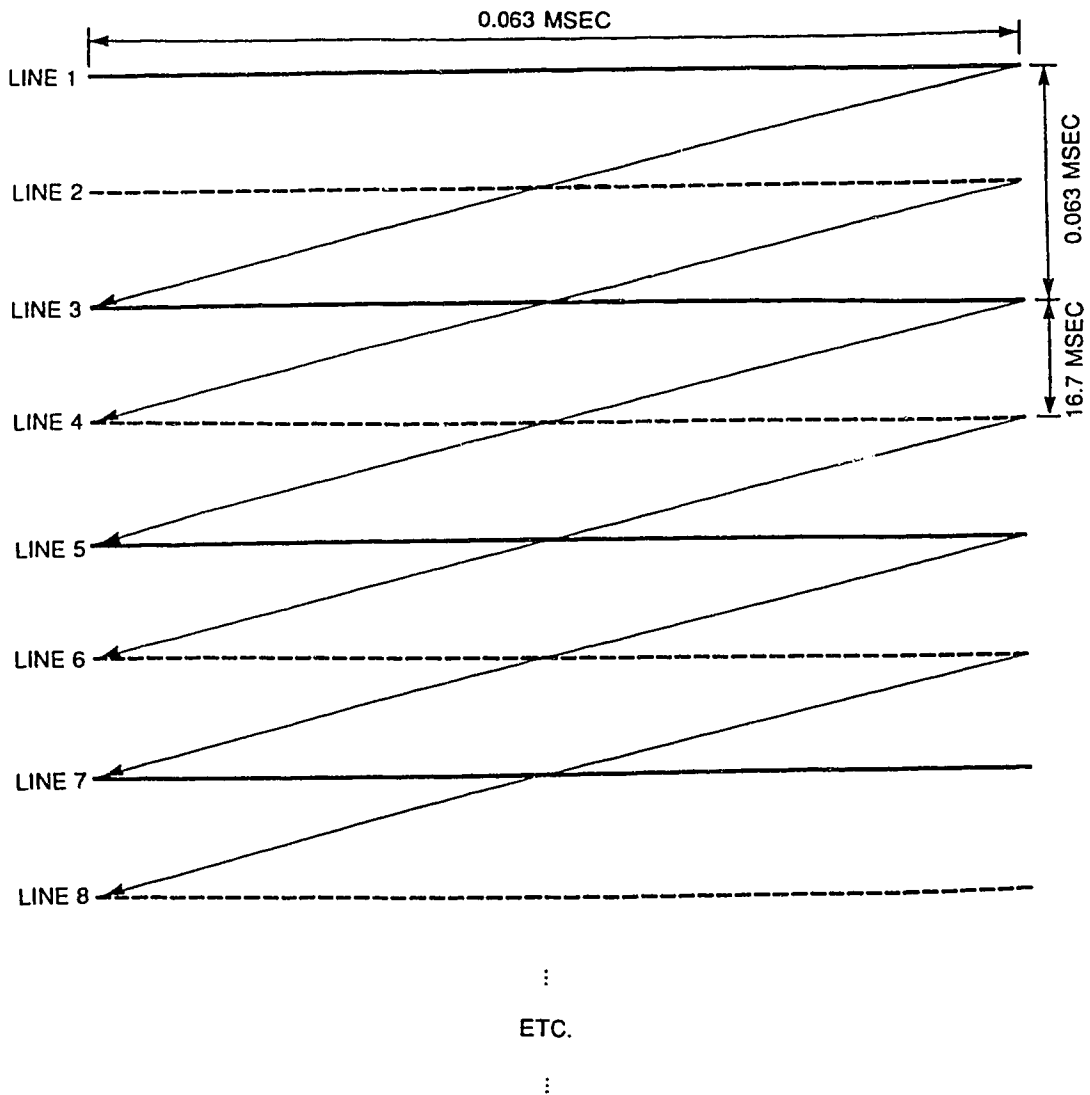


Figure 3-10: A one pixel vertical step is separated by 16.7 msec. A two pixel vertical step is separated by only 0.063 msec.

Chapter 4 - Digital Image Processing of Jet Images

4.1 Overview

Plate 4-1 is a color print of a typical data slide from a two jet, two dye (fluorescein and rhodamine) jet interaction experiment before digitization and digital image processing. Plate 4-2 is a print from a single jet, single dye (fluorescein) data slide. Although the reproduction process has obscured some of the fine detail visible in the original slides, these plates still show most of the flow detail that can be resolved using the laser sheet light flow visualization technique. Before these images can be used to produce quantitative data, they must be digitized and corrected so that they display the dye concentration field, rather than just the fluorescence intensity field. For example, they must be corrected for the varying intensity in the laser light sheet.

4.2 Concentration from Intensity: Analytical Model

Figure 4-1 shows the coordinate system used to describe position of any point illuminated by the sheets of laser light. Because the light sheets spread radially from their focal points, the simplest way to describe position in a light sheet is using radial coordinates r and θ . The illumination technique in the present study uses two separate light sheets with two separate focal points, so confusion may result using this system to describe all positions in the test section. The following convention will be adopted: Position in a light sheet will be described with radial coordinates based on that light sheet's origin, while position in the test section will be described with cartesian coordinates x (horizontal position) and z (vertical position, positive in the

Plate 4-1: Typical uncorrected, full color image from two laminar jet interaction experiment.

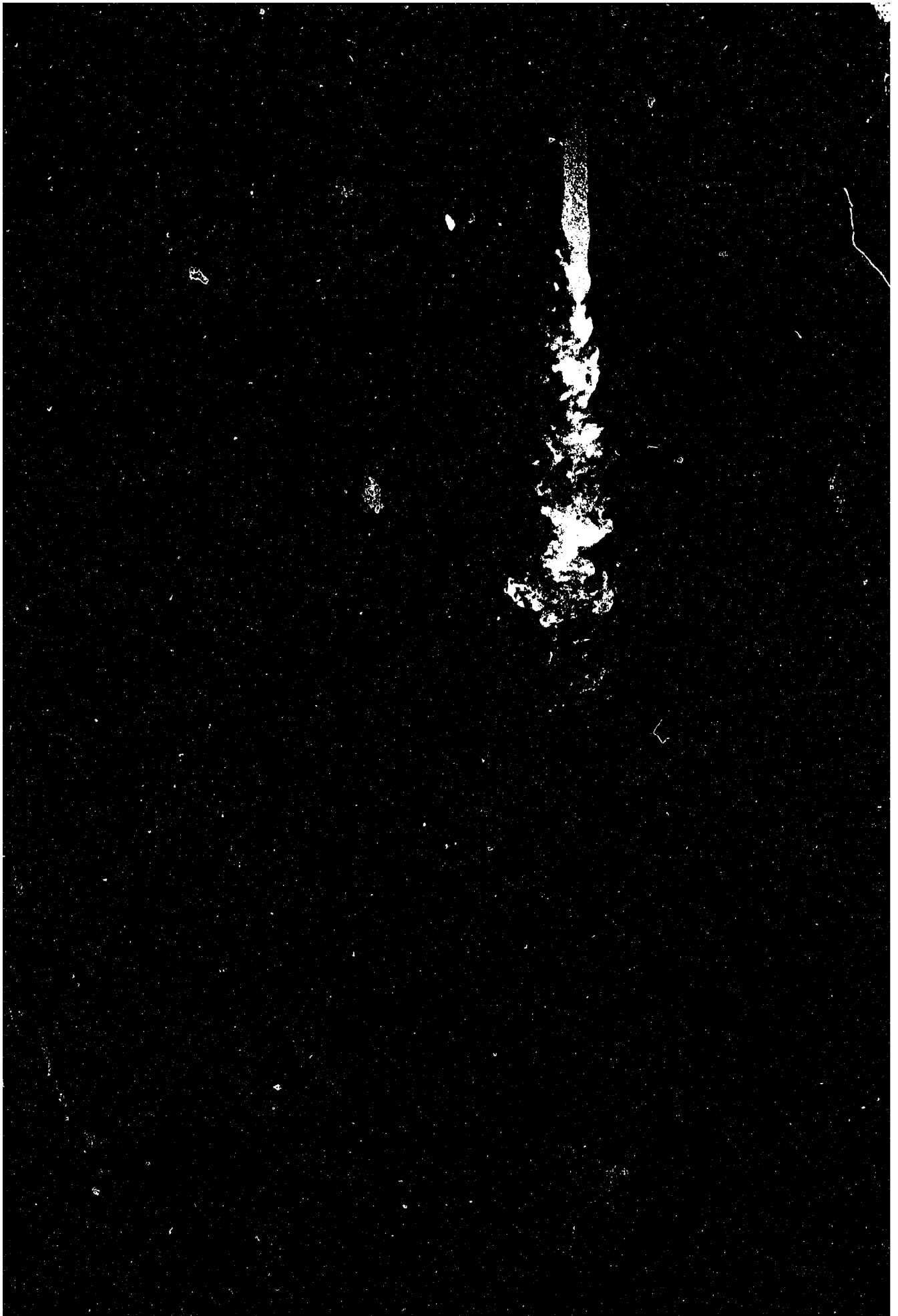
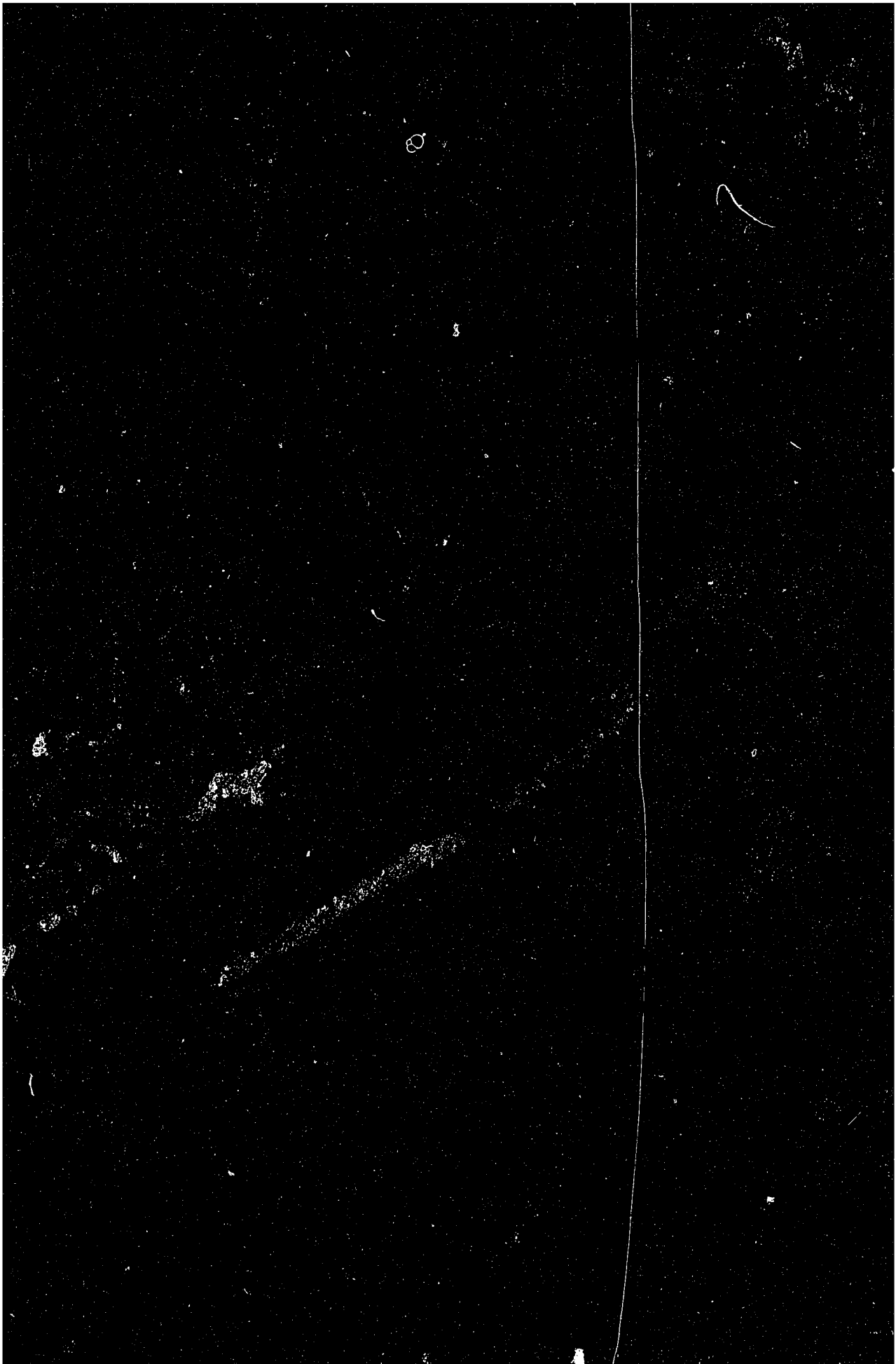


Plate 4-2: Typical uncorrected, full color image from a single turbulent jet experiment.



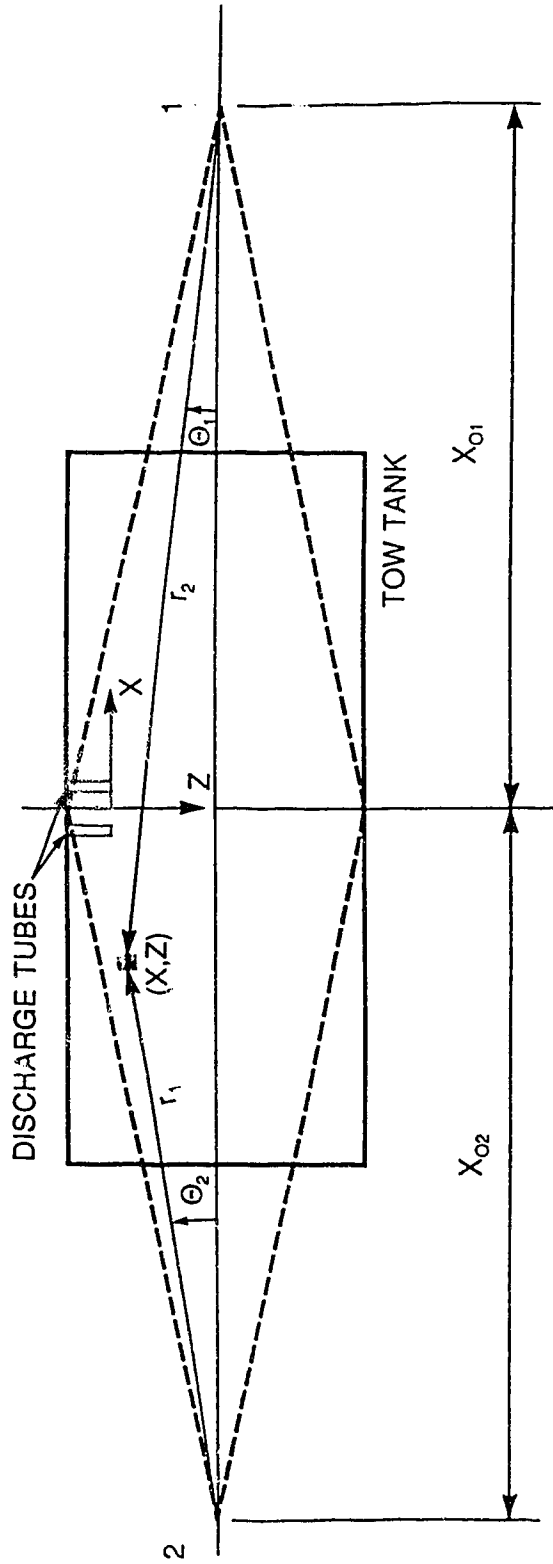


Figure 4-1: Any point in the system can be described by (x,z) , (r_1, Θ_1) and/or (r_2, Θ_2) coordinates, whichever is best suited for the task at hand.

direction of jet flow). For single jets, the origin will be at the center of the left hand discharge tube exit (left hand as viewed in Figure 4-1). For two jets, the origin will be centered between the two discharge tubes. Since $x=x(r,\theta)$ and $z=z(r,\theta)$, equations in the following analysis will use a mix of coordinate systems.

At any point (r,θ) in the plane, the fluorescent light intensity $F(r,\theta)$ as perceived by the image recording and processing system will consist of the contribution from any dye fluorescing at that point, considered here to be independent of dye color. In this study disodium fluorescein (green) was used in single dye color experiments. It was also used along with rhodamine 610 (orange-red) for two color experiments. Therefore the total perceived fluorescence in a two color experiment is:

$$F_{TOTAL}(r,\theta) = F_{FLUORESCIN}(r,\theta) + F_{RHODAMINE}(r,\theta) \quad (4.1)$$

Hopefully, the fluorescence intensity from each of the two dyes can be separated into two images based on colorimetric information. Operating under that premise, the rest of this analysis will assume the fluorescence in an image is from one dye alone. The fluorescence distribution for a single dye, then, is:

$$F(x,y) = f(C) \cdot C(x,y) \cdot [I_{LS1}(r_1,\theta_1) + I_{LS2}(r_2,\theta_2)] \quad (4.2)$$

where: $F(x,y)$ is the measured fluorescence of the single dye at any point in the image.

$C(x,y)$ is the concentration of dye at any point in the image.

$I_{LS1}(r_1, \theta_1)$ is the intensity of light sheet #1 at any point in the image.

$I_{LS2}(r_2, \theta_2)$ is the intensity of light sheet #2 at any point in the image.

$f(C)$ is a transfer function relating actual fluorescent light level to fluorescence as measured by the image processing system in integer counts over the 0 to 255 range available in the 8 bit storage register.

The transfer function $f(C)$ may be a simple constant, or it may depend on the dye concentration at the point of interest. This function will be treated in this study as a simple "calibration constant" to relate intensity level in the image processing system to actual fluorescent light level. In order to determine the jet fluid concentration distribution from the fluorescence distribution the intensity distribution of the two light sheets must be known.

The intensity of a light sheet along a line of constant angle θ is described by the differential equation:

$$dI = -\frac{I}{r} dr \quad (4.3)$$

This equation describes the intensity decrease of the sheet due to simple geometric expansion, and ignores any other effects. If the laser intensity at any point along this line of constant θ is known, ie: if $I_0(r_0)$ is known, then this equation can be integrated

to give:

$$I = \frac{I_o r_o}{r} \quad (4.4)$$

In general, I_o at r_o will be a function of angle θ , so the intensity of a sheet of light based only on initial intensity distribution across the beam entering the cylindrical lens and geometrical expansion will be:

$$I(r,\theta) = \frac{I_o(\theta) r_o}{r} \quad (4.5)$$

If the amount of laser sheet light absorbed by the fluorescent dye in the test section is significant, then equation (4.3) must be modified to account for this. For a single dye the governing differential equation is:

$$dI = -\frac{I}{r} dr - I \cdot a(C) \cdot C(r,\theta) dr \quad (4.6)$$

where: $C(r,\theta)$ is the dye concentration as a function of position.
 $a(C)$ is the dye attenuation factor, a function of concentration.

This differential equation can also be integrated from a radius r_o where the intensity is known, resulting in

$$I(r,\theta) = \frac{I_o(\theta) r_o}{r} \cdot \exp\left(-\int_{r_o}^r a(C) C(r',\theta) dr'\right) \quad (4.7)$$

For a two dye experiment, both dyes must be included in equation (4.6) to properly account for beam attenuation; they cannot be treated separately. This results in:

$$I(r,\theta) = \frac{I_o(\theta) r_o}{r} \cdot \exp\left(-\int_{r_o}^r [a_1(C_1) \cdot C_1(r',\theta) + a_2(C_2) \cdot C_2(r',\theta)] dr'\right) \quad (4.8)$$

Continuing with the single dye case, equation (4.7) can be rewritten for a discrete array of concentration values, such as a video picture of a fluorescence experiment:

$$\begin{aligned} I(\theta, r_i) &= \frac{I_o(\theta) r_o}{r_i} \cdot \exp\left(-\sum_{k=0}^i [a(C_k) \cdot C_k \cdot \Delta r]\right) \\ &= \frac{I_o(\theta) r_o}{r_i} \cdot \prod_{k=1}^i (\exp[-a(C_k) \cdot C_k \cdot \Delta r]) \end{aligned} \quad (4.9)$$

Whether discrete or continuous forms are used, the concentration distribution must be known in advance in order to calculate the light sheet intensity distribution. But, the light sheet intensity distribution must be known in order to calculate the

concentration field! With a single light sheet, it is possible to march along lines of constant θ starting from r_o and updating I and C along the whole light sheet. With two light sheets, however, the problem would have to be solved using an iterative technique of some sort. An example of the marching correction along a single light source is given by Koochesfahani and Dimotakis (1985). They did not use a sheet of light, but rather measured concentration along a single laser beam. A similar marching technique would apply along a line of constant θ in a light sheet experiment.

4.3 Dye Attenuation of Laser Light Sheet Power

An interesting simplification of equation (4.7) is the case of a single light sheet passing through a tank of constant concentration dye. Although uninteresting from a fluid mechanics viewpoint, this case allows the determination of the dye attenuation factor, $a(C)$. Beginning the integration from the input edge of the tank (r_o), the resulting light sheet attenuation is:

$$I(r,\theta) = \frac{I_o(\theta) \cdot r_o}{r} \cdot \exp[-a(C) \cdot C \cdot (r - r_o)] \quad (4.10)$$

The fluorescence distribution is the parameter actually measured using the image processing system. It follows from equation (4.2) that the fluorescence along a line of constant θ should be:

$$F(r,\theta) = \frac{F_o(\theta) \cdot r_o}{r} \cdot \exp[-a(C) \cdot C \cdot (r - r_o)] \quad (4.11)$$

where F_o is the fluorescence caused by I_o and C at r_o . Because the exact functional form of $a(C)$ is not known, we can define $\Phi(C) = a(C) \cdot C$, and write:

$$\frac{F}{F_o} \cdot \frac{r}{r_o} = \exp \left[-\Phi(C) \cdot r_o \cdot \left(\frac{r}{r_o} - 1 \right) \right] \quad (4.12)$$

This special case was tested by filling the tow tank with various concentrations of the two laser dyes. Only one light sheet was used to illuminate the solution, and the fluorescence along the light sheet center line was recorded using 35 mm slides which were subsequently digitized and corrected with the image processing system, as described in Chapter 3. Results for five different concentrations of disodium fluorescein are shown in Figure 4-2. These cover the range of dye concentrations used in jet visualization experiments from $C_{\text{dye,F}}/C_{\text{a,F}} = 0.6$ to 1.0, where C_o is the dye concentration of pure fluorescein dyed jet fluid. Results for four different concentrations of rhodamine 610 are shown in Figure 4-3. The range of data from $C_{\text{dye,R}}/C_{\text{a,R}} = 0.1$ to 0.18 is plotted.

Ideally, more data would be needed to correctly define the attenuation characteristics of the dyes. Tests were originally conducted on both types of dye over the same absolute 1:10 concentration range of $1 \cdot 10^{-7}$ mol/liter to $1 \cdot 10^{-6}$ mol/liter. Since the dye concentration used in rhodamine jet fluid was five times higher than the fluorescein jet fluid, no rhodamine data were taken at concentration ratios higher than $C_{\text{dye,R}}/C_{\text{a,R}} = 0.2$. Additionally, the entire range of attenuation data could not be recorded on film with the same exposure. At the time the data were taken, large

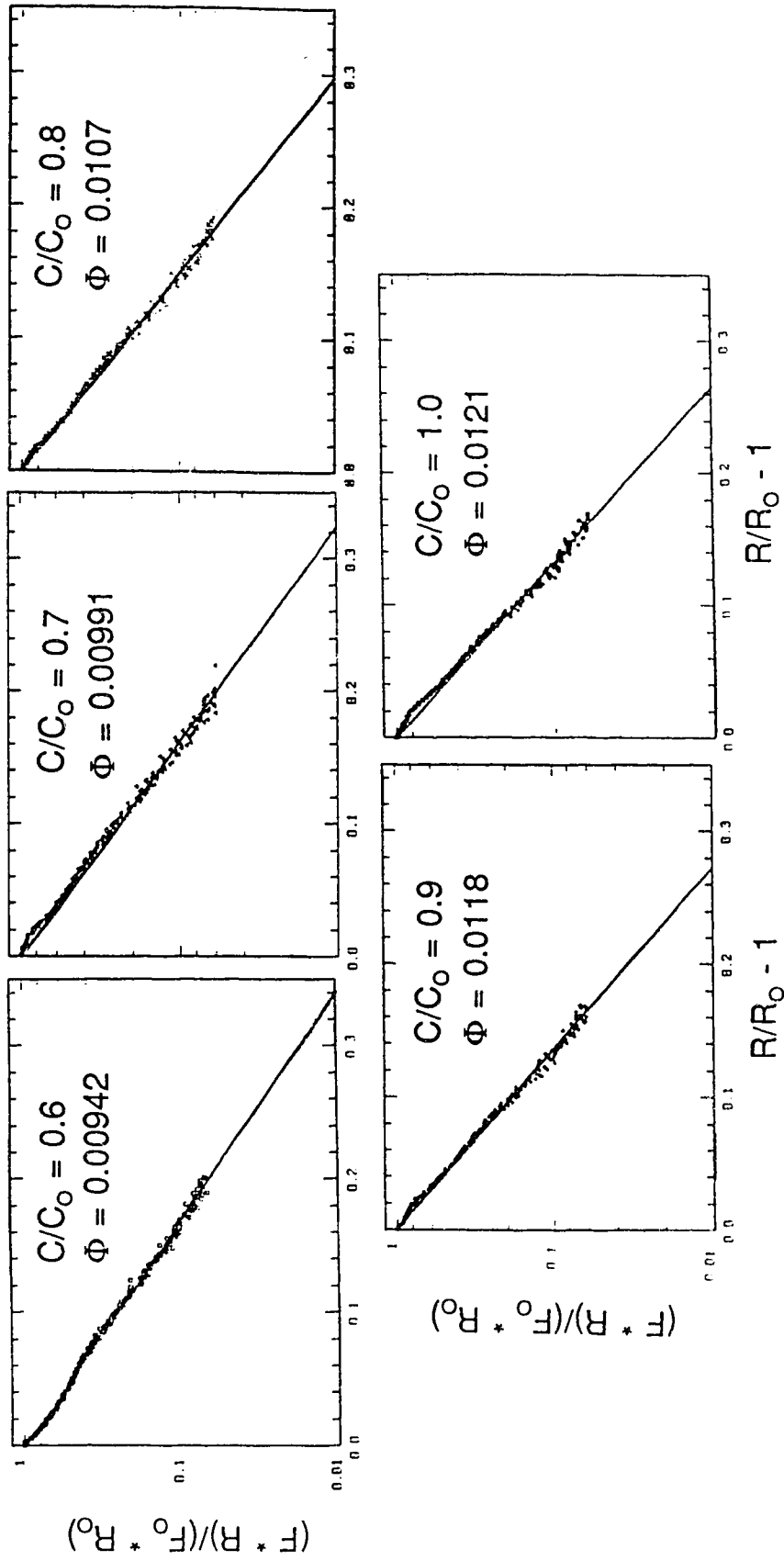


Figure 4-2: Light sheet attenuation in disodium fluorescein.

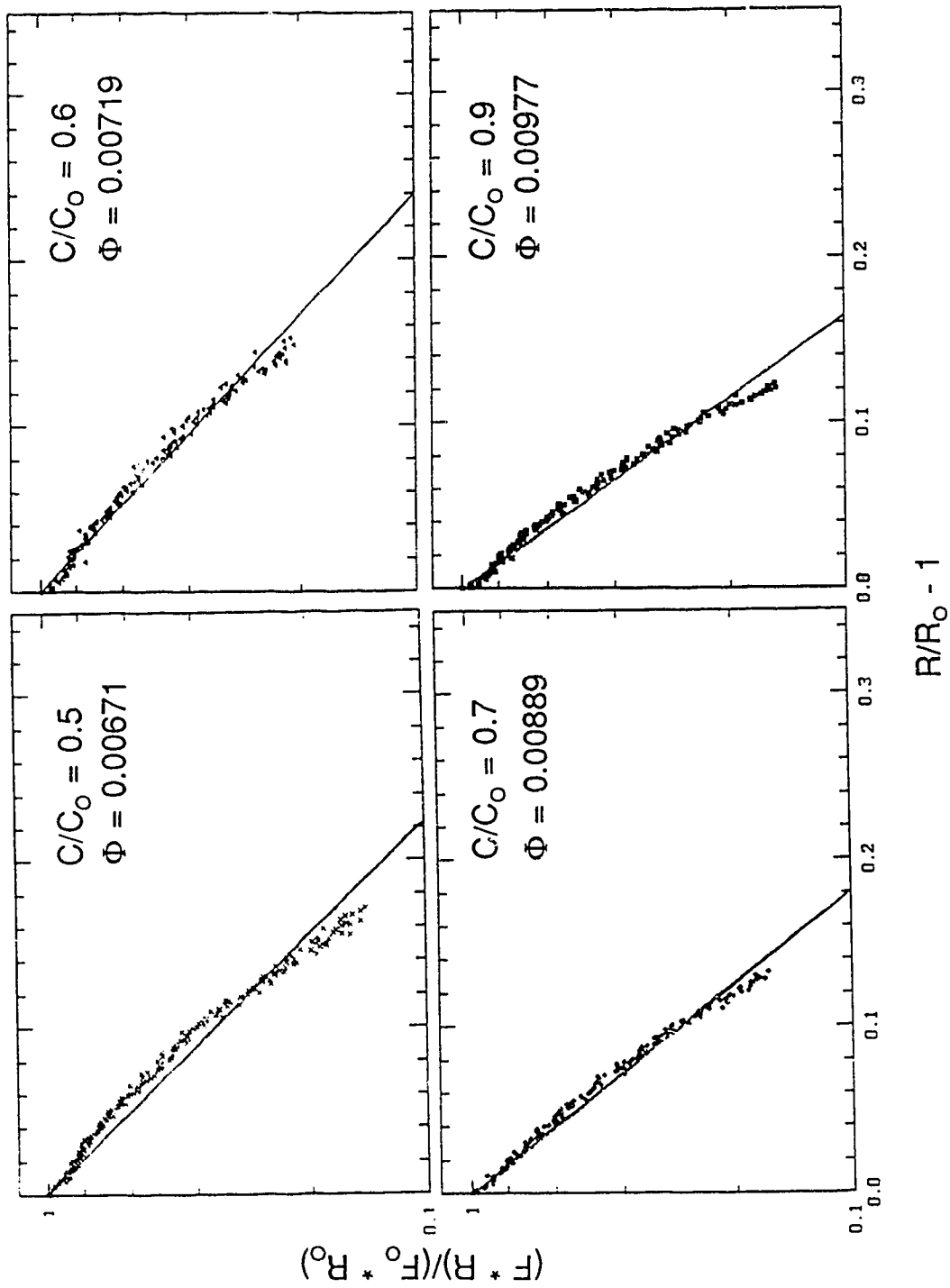


Figure 4-3: Light sheet attenuation in rhodamine 610.

departures from predicted attenuation behavior were thought to be due to film linearity problems. The data shown cover the widest range which could be recorded at the same aperture and shutter speed. It was later discovered that the apparent departures from predicted attenuation were caused by the video camera nonlinear behavior which could be corrected for. In retrospect, the attenuation data at other film exposures could have been used. However, those data had been discarded by this point.

The attenuation tests do not cover the concentration range where rhodamine attenuation in the jets would be significant. Fortunately, as is discussed below, no quantitative measurements of concentration were made using rhodamine. The tests do cover the highest concentrations of fluorescein used. As will be shown, the attenuation of laser light in fluorescein-dyed jets could be safely neglected. Although the paucity of data in this test will not effect image analysis in this thesis, further work in this area is needed. An analytical framework has been developed so that future work can accurately determine the exact attenuation functions for the dyes when attenuation must be corrected.

All data sets have had a best fit (least squares) line of constant $r_0 \cdot \phi$ fitted through them, shown by the solid line. Since r_0 is a constant for any given geometry, the material property $\phi(C)$ for each dye can be determined from the best fit value of $r_0 \cdot \phi$. Equation (4.12) predicts that $r_0 \cdot \phi$ should fall as a straight line on a semi-log plot of $\ln[(F \cdot R)/(F_0 \cdot R_0)]$ versus $R/R_0 - 1$. The data for disodium fluorescein follow this trend, and the least squares fit of the data is a good representation of the

behavior of the fluorescein.

The measured behavior of rhodamine 610 does not follow the predicted model as well. The emitted light intensity of the fluorescing rhodamine 610 was much less than that from the fluorescein during this experiment. The data slides from the rhodamine test were underexposed compared to the fluorescein test. As a result, the image digitization camera/system was required to operate in the lower 25% of its range while digitizing these slides. The underexposed film, the image processing system's operating range, or perhaps inadequacies in the predictive theory may have been responsible for this deviation.

The purpose of this test was to determine the functional forms of $\Phi_F(C_F)$ and $\Phi_R(C_R)$. These quantities are plotted versus jet fluid concentration normalized by the nozzle jet concentration in Figures 4-4 and 4-5. The functional forms are:

$$\begin{aligned}\Phi_F &= 0.012 \cdot C_F^{1/2} \\ \Phi_R &= 0.033 \cdot C_R^{7/10}\end{aligned}\tag{4.13}$$

These are for $C = C/C_o$, and for this study, $C_{o,F} = 1 \cdot 10^{-6}$ mol/l and $C_{o,R} = 5 \cdot 10^{-6}$ mol/l. The functional forms would have to be modified to account for different source concentrations.

A least squares fit was used to determine the coefficients and exponents of these functions, and a power function was assumed as the form of Φ for simplicity. Although a linear function with a zero offset would fit the limited amount of data, the

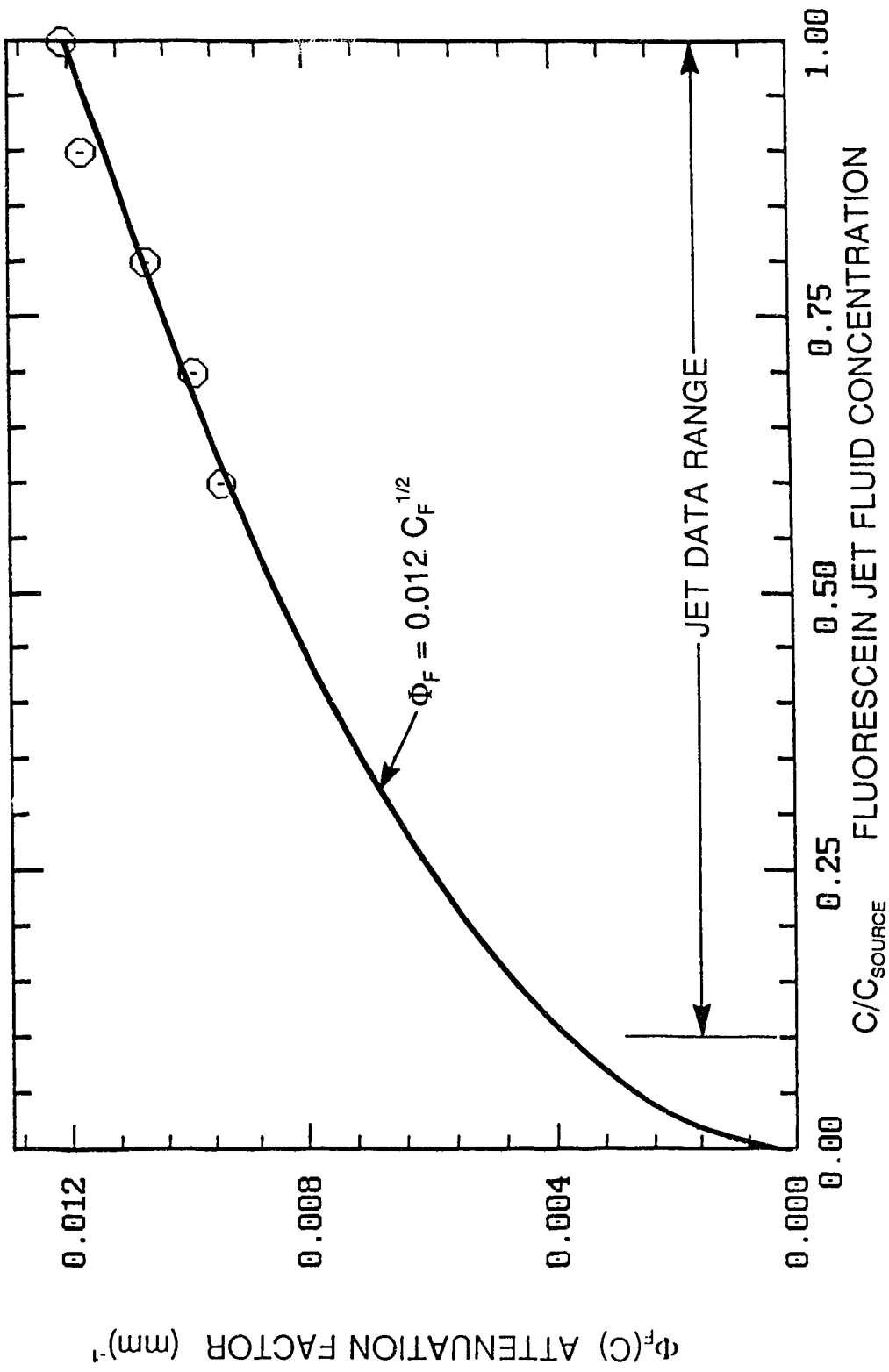
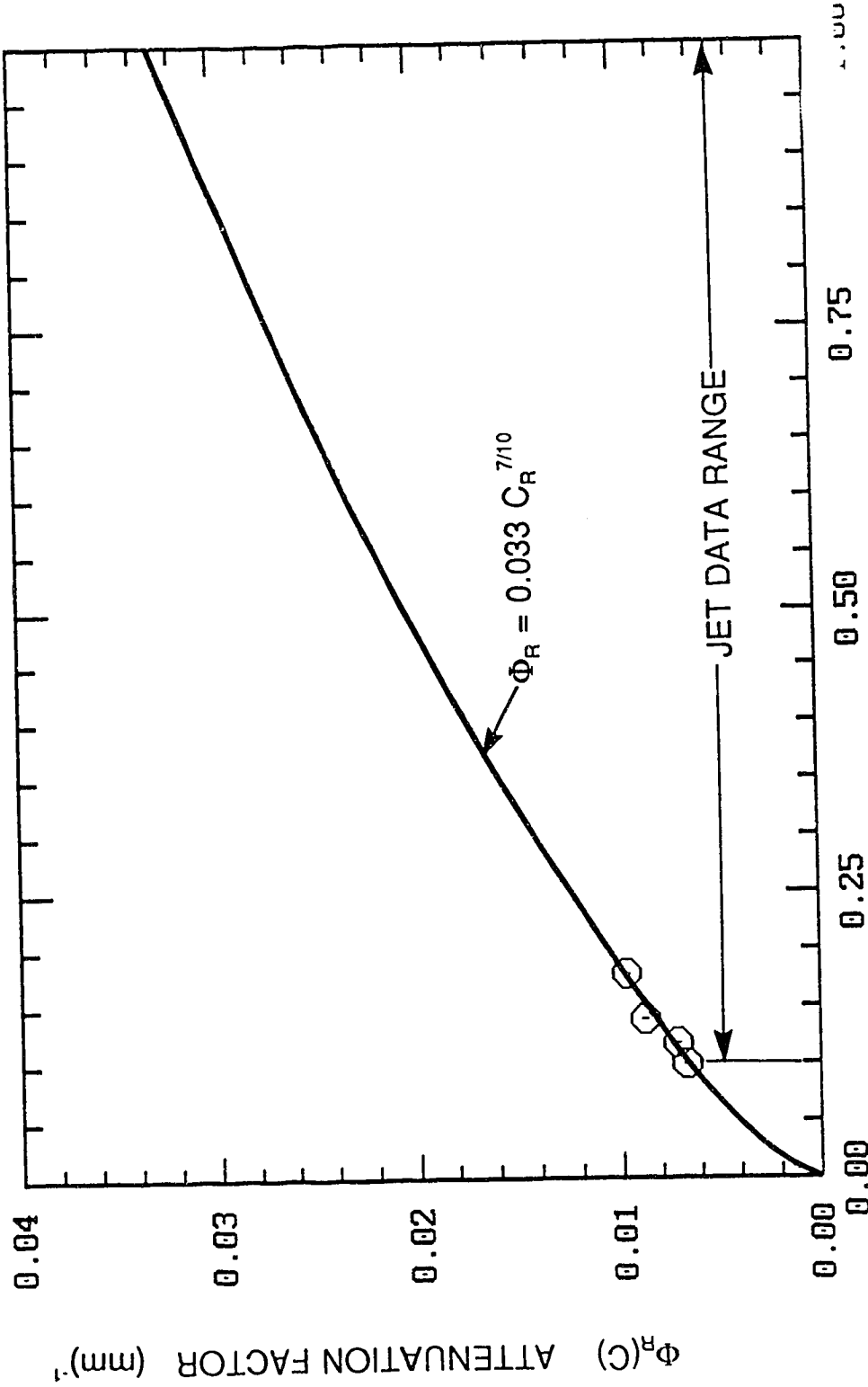


Figure 4-4: Assumed functional form of fluorescein attenuation factor ϕ_F for normalized jet fluid concentration. Fluorescein source concentration is $1 \cdot 10^{-6}$ mol/l.



C/C_{SOURCE} RHODAMINE JET FLUID CONCENTRATION

Figure 4-5: Assumed functional form of rhodamine attenuation factor Φ_R for normalized jet fluid concentration. Rhodamine source concentration is $5 \cdot 10^{-6}$ mol/l.

given power functions pass through zero attenuation at zero concentration. For the distances involved here, absorption of laser light by the water should not be significant, so the power function form was used. The experimental data for disodium fluorescein covers the high end of the range of normalized jet fluid concentrations where attenuation may be a problem: $0.6 < C_{JET,F} \leq 1.0$. The attenuation function for fluorescein can probably be used with a degree of confidence. The data for rhodamine attenuation, $0.6 < C_{JET,R} \leq 1.0$, does not cover the jet fluid concentration range where attenuation will be at a maximum. This fact, coupled with the deviation of the experimental attenuation data from the predicted behavior, makes the resulting attenuation function for rhodamine suspect. Further work will be required to more accurately quantify the attenuation behavior of rhodamine 610 at the concentrations used in this study for flow visualization. The problem of laser light sheet attenuation in rhodamine 610 is not considered further in this work.

By careful selection of flow and lighting geometries, the need for attenuation correction was minimized. As can be seen in Plate 4-1, initially laminar jets have a fairly large unmixed zone immediately downstream of the discharge tube. This is useful because it provides a region of known concentration in the image. The attenuation of a single light sheet passing through the laminar region of a fluorescein jet can be estimated using the model developed. The concentration in the laminar region will be $C_{jet,F}=1.0$. For the flow and lighting geometries used here $r_0 = 1432$ mm and the jet width = 8.8 mm. From equation (4.13) ϕ_F will be -0.012 for $C_{jet,F} =$

1.0, and equation (4.10) can be used to show that I/I_0 will decrease to a minimum of 0.89 across the laminar region, or 11% attenuation. If a simple top hat profile is assumed for both concentration and velocity, the average dye concentration in any cross section must go like $C_{avg} \cdot D_{jet} = \text{constant}$ by mass conservation. Substituting this into equations (4.13) and (4.10) shows that the minimum light sheet intensity will on average vary as $\exp(-D_{jet}^{1/2})$. For this study, the maximum observed jet width was approximately 8 diameters. The above analysis shows that I/I_0 will decrease to approximately 0.7 across the maximum jet width, or 30% attenuation. This increase in attenuation with increased jet width is due to the observed dye attenuation characteristics. The attenuation across the jet will be the same at all jet cross sections only if the attenuation factor has the form $\Phi(C) = a \cdot C$, where "a" is a positive constant.

When the jet was illuminated from either side by two different light sheets, the predicted light sheet intensity across the laminar region can be calculated by applying the above analysis to each sheet. The total light sheet intensity is the sum of the intensities from the two sheets, and for the given flow and lighting geometry it will vary by less than 0.2% across the laminar region of the jet. For the idealized top hat jet profiles from above, the maximum intensity variation across the widest observed part of the jet will be less than 2%. It was felt that this small error could be safely neglected for this study. A correction would probably be needed, however, if only a single light sheet was in use, if higher dye concentrations were used, or if a more absorptive dye than disodium fluorescein was used, such as rhodamine 610.

4.4 Correction of Light Sheet Non-Uniformity

Referring back to Plate 4-1, it can be seen that the constant concentration laminar region of the jet is certainly not constant intensity, but rather grows brighter with distance downstream of the discharge tube. This shows clearly that the variation of intensity with θ must be corrected for.

If the laser beam input to the cylindrical lens has a true Gaussian profile, then a perfect cylindrical lens would create a light sheet with a Gaussian profile $I(\theta)_{\text{GAUSSIAN}}$. A true Gaussian profile would allow for an analytical correction of light sheet variation possible. Unfortunately, real light sheets generated with fiber optics exhibit only approximately Gaussian behavior with many irregularities. Some of these irregularities are due to lens and tow tank sidewall imperfections, but the worst irregularities are caused by the light path within the fiber optic cable itself. These irregularities show up as bright and dark bands within the light sheets which cannot be predicted analytically.

The simplest way to determine the true $I(\theta)$ distribution within the tow tank is to fill it with a calibration solution of weakly concentrated fluorescent dye and illuminate it with the actual light sheets. Before or after each data run, the tow tank was drained and filled with a solution of $2 \cdot 10^{-7}$ mol/l disodium fluorescein, without altering the light sheets, the discharge tube displacement, or the 35 mm SLR camera placement. A longer exposure time, 1/15 of a second, was used to record the fluorescence of this weak solution. This image, once digitized and corrected to true intensity, was used to normalize each jet data image.

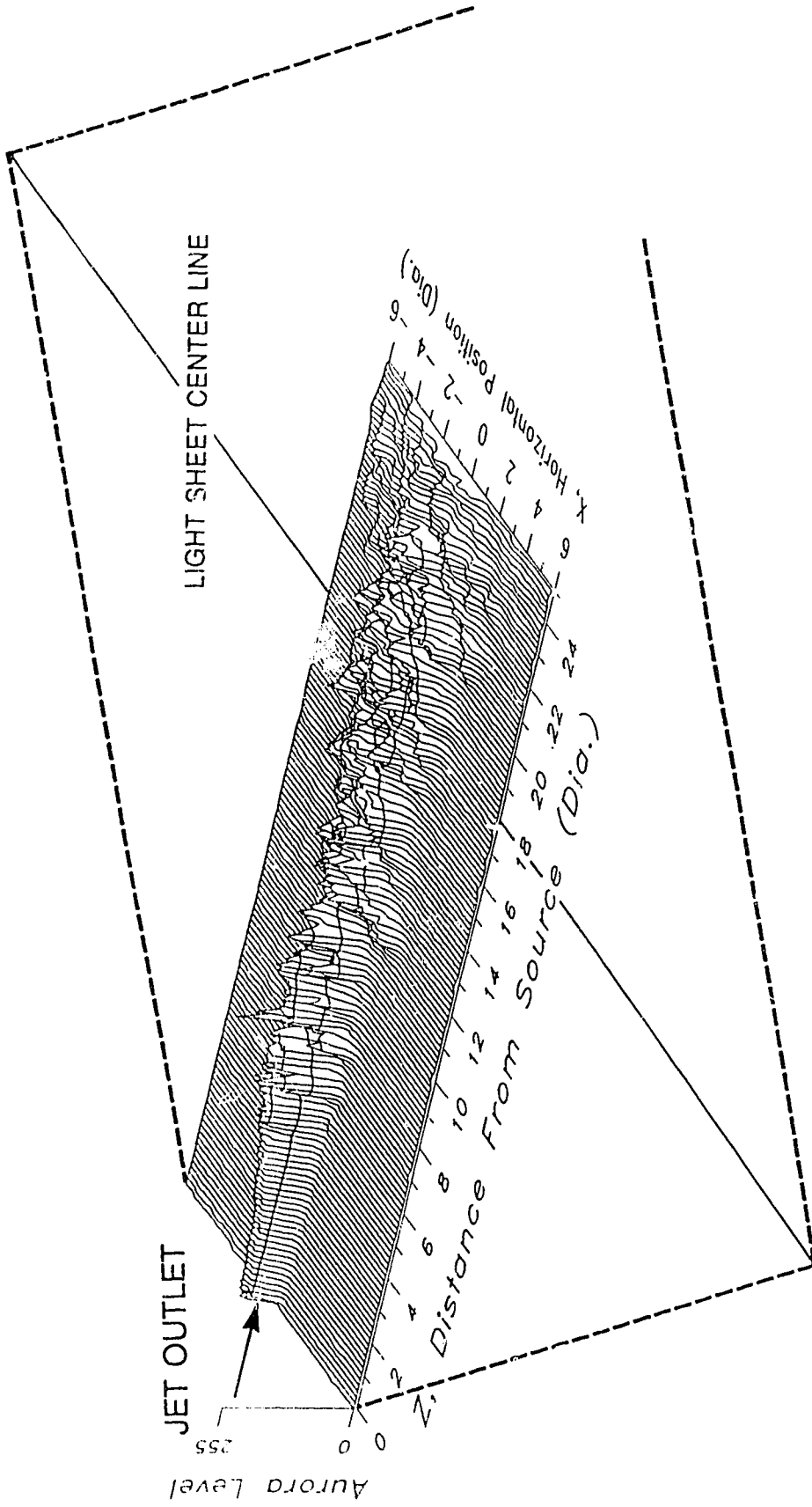


Figure 4-6: Typical jet image fluorescence distribution - two light sheets.

Figure 4-6 shows a surface plot of the fluorescence distribution in a typical fluorescein jet with an initially laminar region of constant concentration dye. The center line of both light sheets is at $z/D = 19$ (where z/D is the downstream distance normalized by jet diameter). It has been digitized from a typical 35 mm slide, and has been processed as described in Chapter 3 to subtract background light intensity and correct for black noise and video camera non-linearity. The effect of light sheet non-uniformity can easily be seen, as the fluorescence intensity increases from the jet origin along the laminar region of constant concentration.

Figure 4-7 shows a surface plot of the fluorescence distribution in the low concentration fluorescein calibration solution. This image has been digitized and corrected in exactly the same manner as the jet image. Because the dye solution is of constant concentration ($2 \cdot 10^{-7}$ mol/l), this fluorescence distribution differs from the light sheet intensity distribution only by a constant multiplier. An important feature to note is the non-uniformity of the distribution in the z direction (θ direction). This distribution would not be well represented by a simple Gaussian. The bright band off of the sheet center line at $z/D = 15$ is typical of the irregularities caused by the fiber optic delivery system. Also important to note is the relative uniformity in the cross-jet, or x direction. At the low dye concentrations used for this calibration picture and with two light sheets illuminating the region of interest, the variation of light sheet intensity in the θ or z direction can be determined.

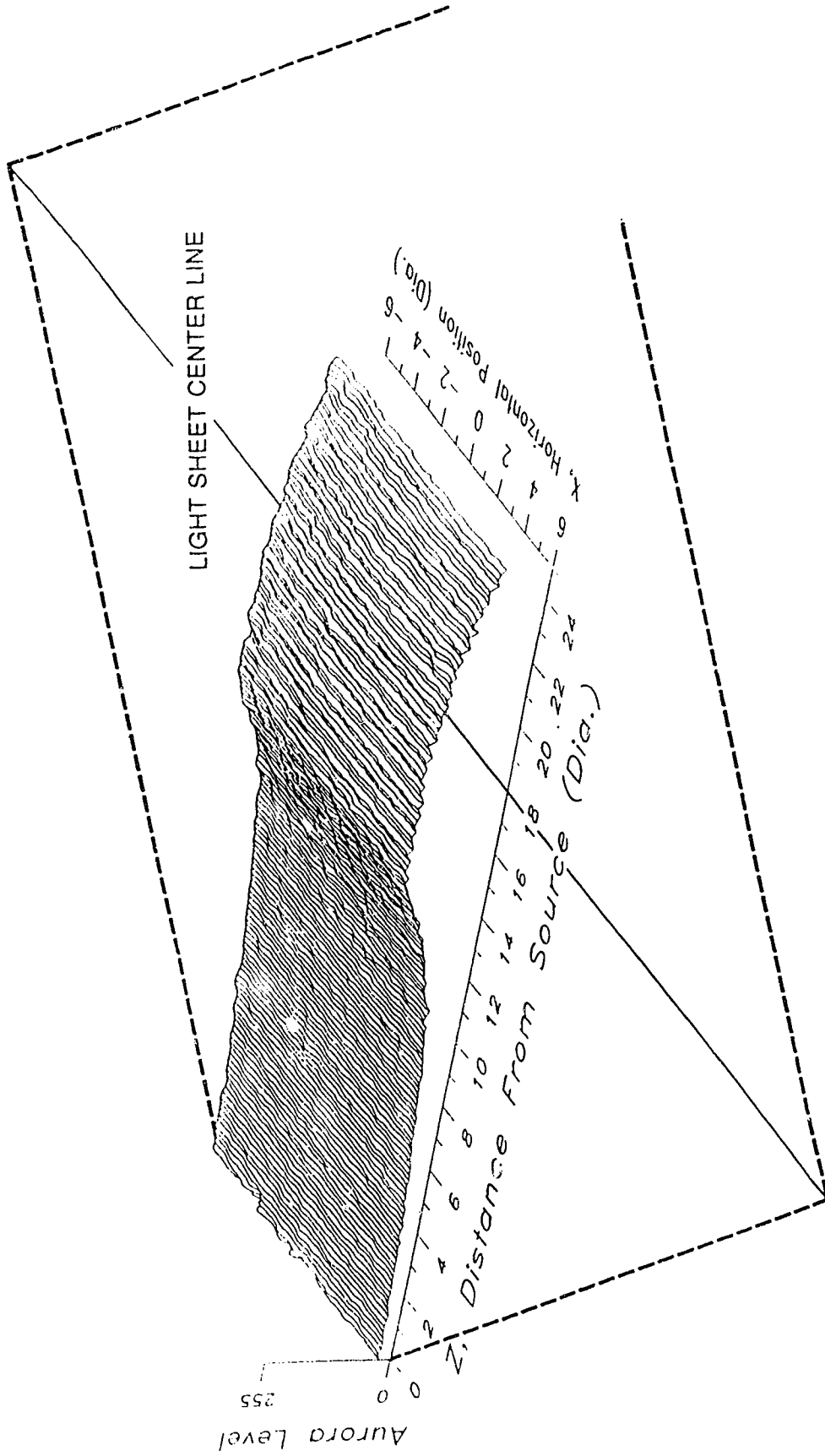
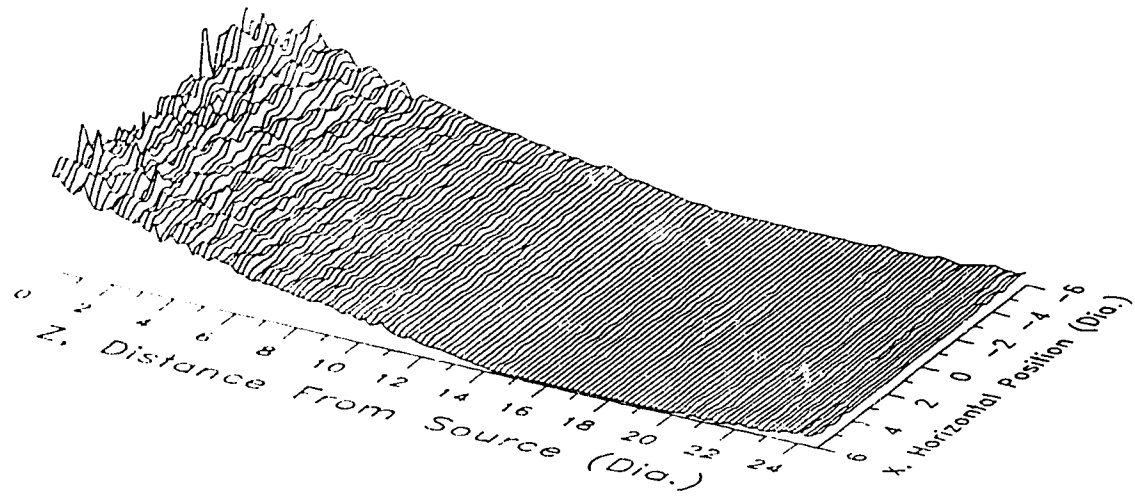


Figure 4-7: Fluorescence distribution in constant concentration dye - two light sheets.

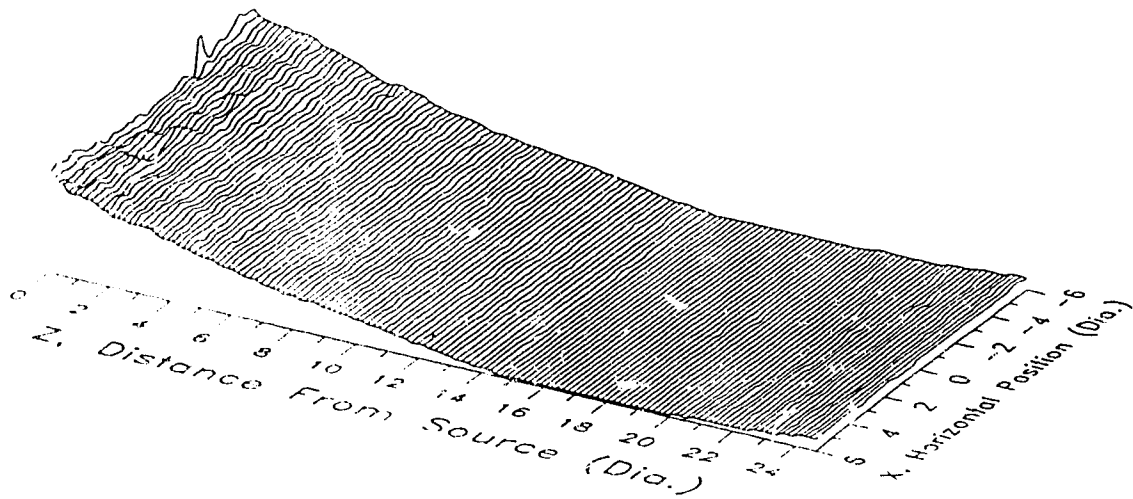
Before the constant concentration light sheet image from Figure 4-7 was used to normalize the jet image, it was spatially filtered to remove random noise. Figure 4-8 shows the correction to be performed to the jet image - ie: the inverse of the light sheet intensity distribution. The random noise in the correction is readily apparent in the low intensity region of the light sheet near the discharge tubes. It is also important to note that all images are digitized into integer intensity levels between 0 and 255. Integer resolution in the low intensity region of the light sheet will show up as larger errors in the correction than in the regions of high light sheet intensity.

Spatially filtering images is accomplished by considering square areas around each pixel in the image. Random noise can be reduced by setting the intensity value of the pixel under consideration to be some function of the pixels in the surrounding square area. For example, a 3 by 3 averaging filter assigns the mean intensity of the 9 pixels in a 3 pixel by 3 pixel square neighborhood to the center pixel. Repeating this process of setting each pixel in the image to its neighborhood's average intensity is a form of two dimensional low pass filtering. If the noise is truly random, then using this type of filter will remove noise. Using larger neighborhoods, for instance 5 by 5 or 7 by 7, will be more effective at removing the random noise, but will also hide more of the fine details of the image.

Another, very similar type of filter is a median filter, where the value of each center pixel in the square array is set to the neighborhood's median intensity level (ie: the level exceeded by 50% of the pixels in the square array). Random noise in video images tends to be in the form of random intensity spikes on single pixels. Using the



INVERSE LIGHT SHEET



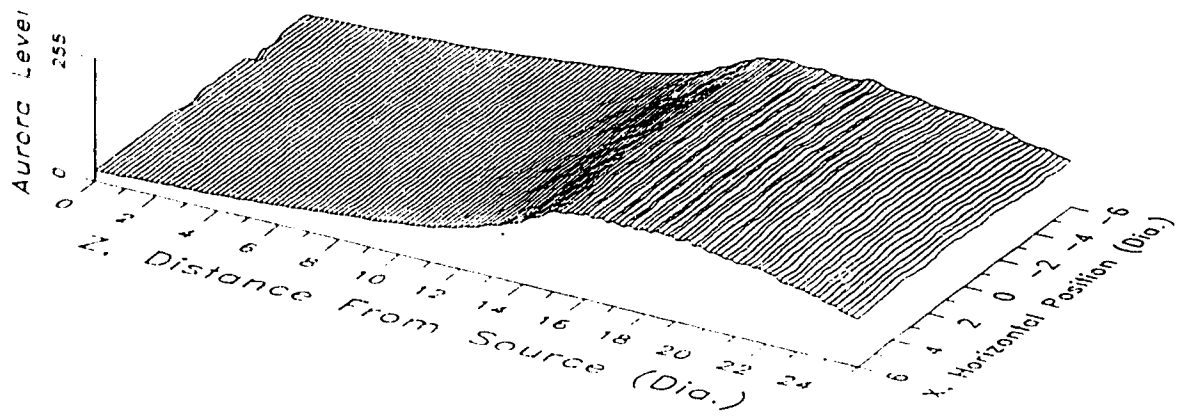
INVERSE MEDIAN FILTERED LIGHT SHEET

Figure 4-8: The effect of median filtering (using 3 x 3 pixel arrays) on light sheet correction.

median intensity of the neighborhood eliminates this type of noise more effectively than the average, because an average would include these spikes.

Median filtering the light sheet before normalization of jet images significantly reduces noise. The filtered light sheet distribution and its resulting normalized jet fluorescence distribution are shown in Figure 4-9. The concentration of jet fluid, normalized by the nozzle concentration, is known to be $C = 1.0$ in the potential core of the jet, allowing the fluorescence transfer function, $f(C)$, to be determined by calculating the average value of the normalized fluorescence within the potential core. If $f(C)$ is assumed constant for all values of C , then the normalized jet fluorescence distribution can be directly converted to the concentration distribution.

As a test for this correction method, a low velocity fluorescein jet was created by using salt solutions to produce a small density difference between jet and ambient fluid to maintain the laminar, constant concentration region for about 9 jet diameters. The constant concentration region of this jet covered about a factor of two increase in light sheet intensity. Figure 4-10 shows the correction which results from normalizing the jet fluorescence distribution with the median averaged light sheet fluorescence distribution. After about one jet diameter from the discharge tube, this method indicates a constant fluorescein concentration in the jet to within $\pm 5\%$. The jet image near the discharge tube was affected by the light reflection from the discharge tube. This scattered light is more intense with a fluorescing jet than with the light sheet alone, causing the normalized jet concentration error close to the tube. This straight-forward method of correcting light sheet nonuniformities reduces the



3 x 3 MEDIAN FILTERED LIGHT SHEET

RESULTING PREDICTED JET CONCENTRATION

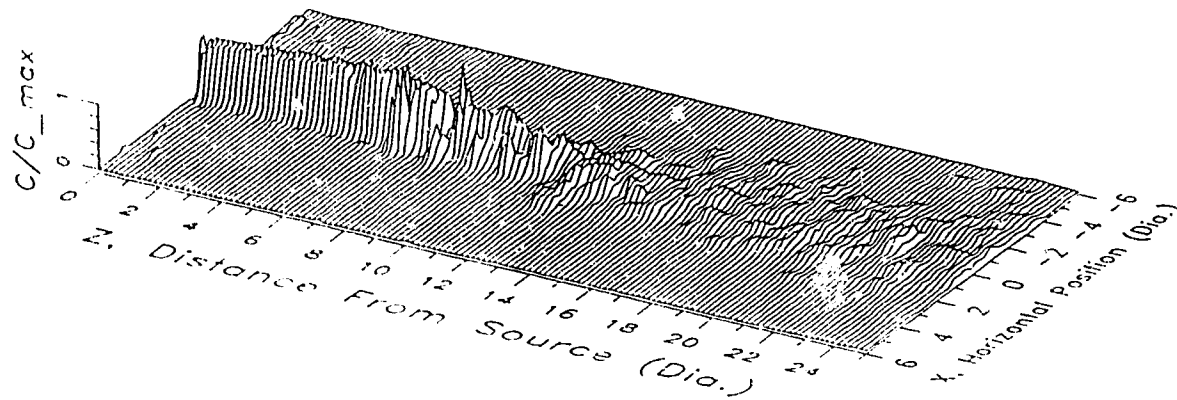


Figure 4-8): Filtered light sheet and resulting predicted jet concentration.

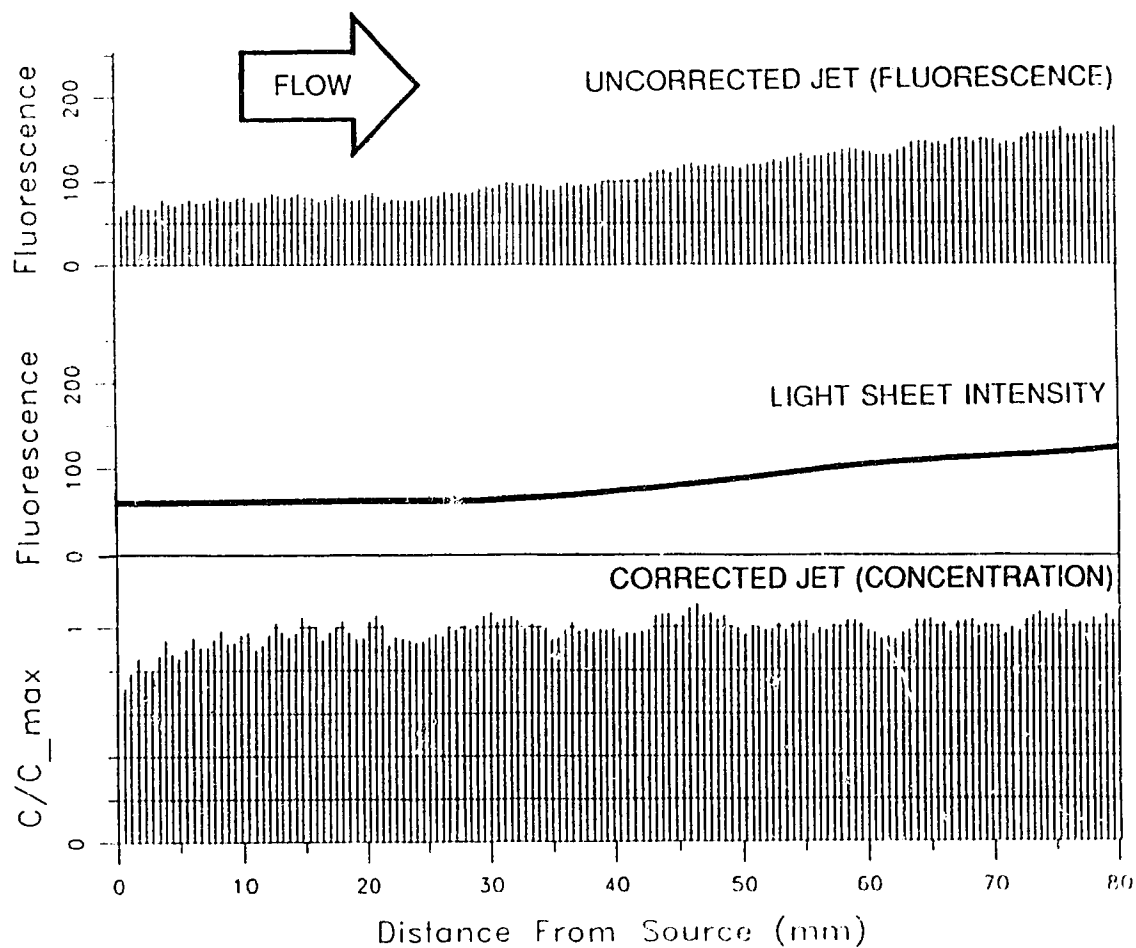


Figure 4-10: Laminar dye column fluorescence, filtered light sheet intensity, and resulting predicted dye concentration. Dye concentration is known to be constant in laminar region of jet - predicted concentration shows errors in correction method.

concentration error in an image to acceptable levels, and was used to convert dye fluorescence to concentration for all jet flow fields in this study.

4.3 Color Separation of Jet Fluid

The purpose of using a full color image processing system, rather than an intensity only, black and white one, was to use color information from a flow visualization image to examine the interaction between three or more mixing fluids. It was hoped that colorimetric information in an image would allow the rhodamine-dyed, fluorescein-dyed, and ambient fluid to all be treated separately so that concentration maps of the fluid originating from each jet in a mixing experiment could be determined from the same image.

In a two-jet, two-color mixing experiment, there are two potential core regions where the fluid is known to be pure jet fluid. From Plate 4-1, the initially laminar regions of each jet can be used to determine the hue of each pure jet fluid. The concentration of each jet fluid at every pixel in the interacting regions of the flow should be able to be determined by the pixel's hue and intensity. Unfortunately, this method could not be applied with any great success in this study.

To determine the apparent hue as a function of jet fluid mixture composition, an experiment was performed by measuring the average hue in the laminar potential core region of a known two component mixture. The jet fluid consisted of a volumetric mixture of standard concentration fluorescein and rhodamine dyes. For example, a mixture of 1 part $1 \cdot 10^{-6}$ mol/l fluorescein to 1 part $5 \cdot 10^{-6}$ mol/l rhodamine simulates a 50% red jet fluid, 50% green jet fluid mixture.

The average hue in the mixed jet laminar region is plotted as a function of mixture composition in Figure 4-11. As discussed in Chapter 2, the absolute concentration of the rhodamine-dyed fluid was deliberately made 5 times higher than that of the fluorescein-dyed fluid to try and match fluorescence levels. Unfortunately, it is apparent from Figure 4-11 that this concentration difference has caused the rhodamine dyed fluid to mask the presence of fluorescein in the mixture. For a 50% fluorescein, 50% rhodamine jet fluid mixture, the average hue has shifted only $\approx 25\%$ of the way from pure rhodamine hue to pure fluorescein hue. This makes any type of calibration curve highly non-linear. For example, the calibration curve shown in Figure 4-12 is a modified second order least squares fit of the calibration data. It was modified to force the function through the origin. If we define:

$$h = \frac{Hue_{ACTUAL} - Hue_R}{Hue_F - Hue_R} \quad (4.14)$$

as the fractional hue, h , between pure rhodamine and pure fluorescein, then the fraction of fluorescein in a given mixture, F_F , is:

$$F_F = 0.1 \cdot \left(1 - \frac{0.01}{h+0.01} \right) + 1.8 \cdot h - 0.9 \cdot h^2 \quad (4.15)$$

It is obvious from Figure 4-12 that this type of calibration will do a very poor job predicting fluorescein fractions below $F_F \approx 25\%$.

Further compounding the problem is the fact that the average measured hue

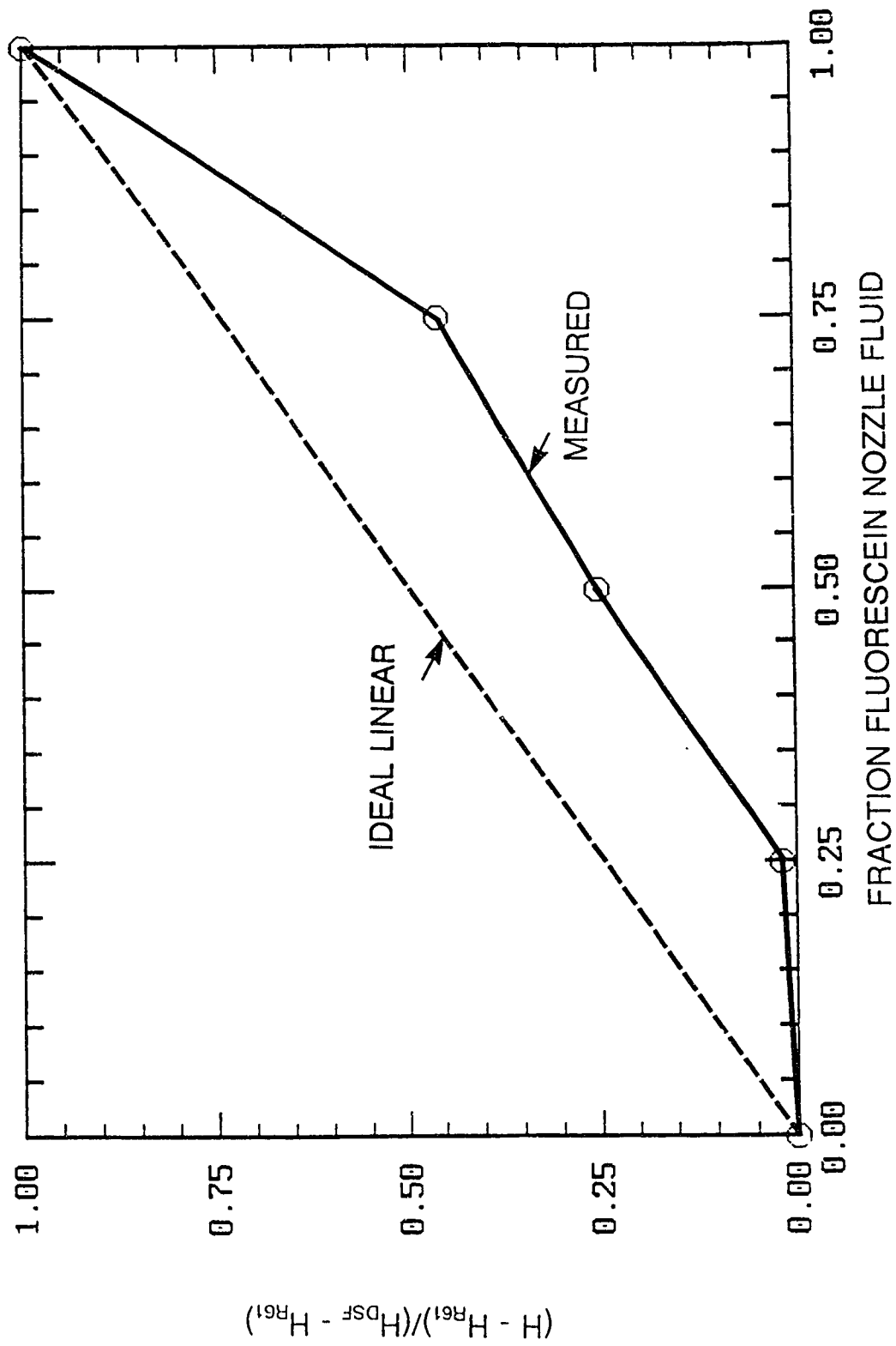


Figure 4-11: Hue variation with mixture composition

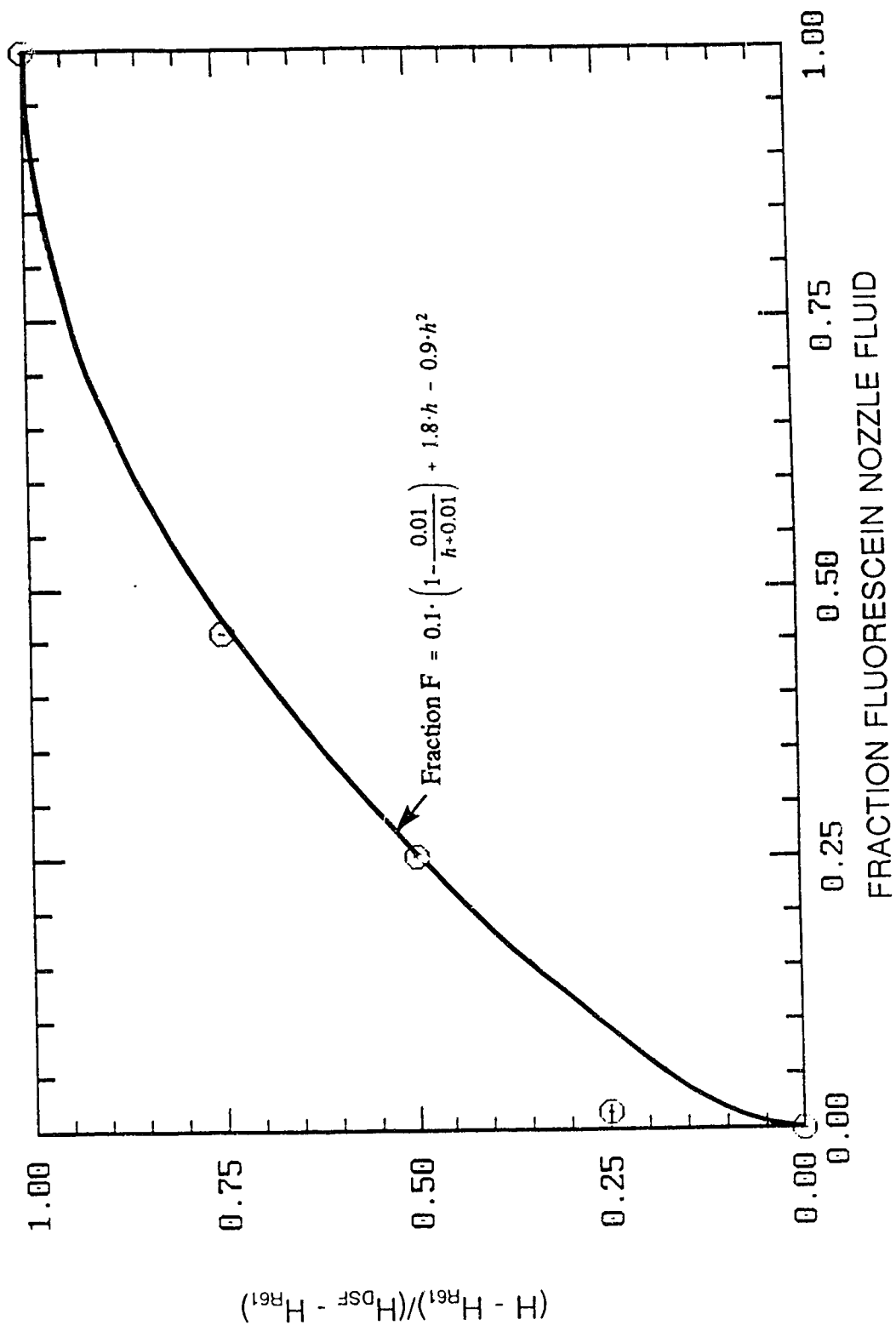


Figure 4-12: Hue calibration curve for fluorescein-rhodamine mixtures.

in the laminar region of the jet may be a poor representation of the hue in that area. Refer back to Figure 3-6, which showed the camera and image processing system's response to a step change in input intensity and the spikes in the RGB signal caused by the edge enhancement circuitry and the analog amplifier response in the camera. The red, green and blue signals each showed different response characteristics. On the right hand edge of the step change, only the red amplifier showed a spike in intensity level. In the jet images being studied, the laminar region of the jets also produced a step change in intensity to the camera. As a result, the hue of the laminar region of the jets shifted towards red moving from the left hand edge of the jet to the right hand edge of the jet. The calibration determined above when applied to images in this study will predict that the mixture composition in the laminar region of a jet is not constant.

The fluorescein/rhodamine separation by hue has a very non-ideal calibration with the two mixtures used in this study. The rhodamine 610 is much more opaque and obscures the disodium fluorescein emission. Hue separation techniques will have to be improved in future studies before this method can be used to analyze multiple hue images.

Further work in this area should be directed toward adjusting the rhodamine concentration levels so as not to mask the fluorescein. Bypassing the edge enhancement circuitry in the camera and developing error correction techniques for the red, green and blue amplifier response curves will allow the hues measured by the image processing system to be less susceptible to edge effects. This study has

established the ground work to pursue analysis of full color flow visualization images, and the topic merits further work.

Chapter 5 - Interacting Turbulent Jets

5.1 Background and Overview

Jets and plumes have been studied extensively over the last century. Many techniques have been developed to study their time averaged behavior using single point velocity probes and single point scalar concentration detectors. Good overviews of jet behavior can be found by Rajaratnam (1976) and List (1982a and 1982b), or in a fluid mechanics reference text such as Schlichting (1979), pp. 729-757.

A number of studies have addressed the problem of interacting parallel jets. Miller and Comings (1960), and Tanaka (1970 and 1974) studied the velocity and pressure fields of a pair of parallel plane (2 dimensional) jets issuing from slots in a common end wall. Marsters (1977), Elbanna, Gahin and Rashed (1983) and Elbanna and Sabbagh (1987) all studied the velocity and pressure fields of pairs of "ventilated" parallel plane jets. "Ventilated" means there was no common end wall between the discharge slots, allowing ambient fluid to enter the mixing process from between the slots.

All of the above experimental studies observed that the center stream lines of the two jets curve sharply toward one another and merge into an apparent single jet due to mutual entrainment of the ambient fluid between the jets. After merging, the mean velocity and turbulence intensity of the combined jets strongly resembled a jet issuing from a single slot located at the midpoint between the two original slots with a displaced origin (further upstream).

Marsters (1977) used a simple mass and momentum conservation to predict

the merging of two ventilated plane jets. This approach could have been adapted to the present study of two round jets, but as will be shown later, the center streamline curvature of the parallel round jet case is not as significant as for the plane jet case, and no attempt was made to use this type of analysis here.

Elbanna (1987) observed that removing the common end wall between the jets reduced the curvature of the merging plane jet center lines, and moved the position of the merging point 2.5 times further downstream than in the equivalent case with an end wall present studied by Tanaka (1970 and 1974). It makes intuitive sense that allowing ambient fluid to enter into the region between the plane jets will reduce the effect of mutual entrainment, and leads one to expect that the curvature of center lines in the parallel round jet case will be very much smaller than in the plane jet case.

Becker and Booth (1975) studied two mixing round jets, but not the case of initially parallel center lines. The center lines of the jets in this study were pointed toward a common intersection point downstream of the jet nozzles. This was the only study found which measured the concentration of a scalar tracer (smoke) in interacting jets rather than the momentum field. Even for this round jet case it appeared the jets deflected toward one another due to the pressure gradient field formed by the impinging jets.

Simonich (1987) investigated the interactions between heated and non-heated parallel round jets at high Mach numbers ($0.6 \leq M \leq 1.44$). No evidence of center line curvature was observed. Rather, the mean velocity profiles of the two jets seem

to spread independently until they grow together. The Mach number had only a small effect on the location of where the jets began to merge. For a jet separation of 3 diameters, the same as used in this study, Simonich found that the velocity profiles of the two jets had grown wide enough to produce non zero velocities on the mutual jet center line at a downstream location of about $z/D = 7$ for all Mach numbers studied. The jets in the present study will be seen to have similar behavior, even though the Reynolds number is several orders of magnitude lower and the flow is virtually incompressible.

Several studies have attempted to describe interacting jets using superposition of single jet momentum fields. Knystautas (1964) used superposition to characterize a line of axisymmetric jets merging to form a quasi-two-dimensional plane jet. Demissie and Maxwell (1982) found the velocity field of a three-dimensional slot jet was well described by superimposing the momentum fields of several axisymmetric square jets in a line (with the same total area and momentum flux). Pani and Dash (1982a and 1982b) used this idea of superposition of momentum to predict the velocity fields of multiple three-dimensional slot and circular jets. In all of these studies, negligible flow field pressure gradients resulted in no observed evidence of jet center line displacement. The momentum superposition concept is expanded upon in more detail in section 5.5.

The majority of this thesis has been devoted to techniques developed to use image processing to study mixing flows. In the course of this work, many data pictures of single and interacting jets have been acquired. These data pictures were

used to study the effect of initial turbulence on the entrainment of single jets and the interactions between parallel jets. This chapter will show that the system developed is a good tool for pursuing this objective and others further. Examples will be shown of taking traditional "point" measurements of concentration with the new system and combining these with Laser Doppler Velocimeter measurements to develop a simple interacting jet model. Some of the unique advantages of full-field concentration measurements will be presented, along with some thoughts on how these can be used to study turbulent mixing experiments in new ways, such as mean and fluctuating jet areas and full field spatial fluctuation correlations.

5.2 Jet Flow System

Jets were produced using the equipment shown by the schematic diagram in Figure 5-1. It is important to note the co-ordinate system used to describe position in the jet. For two jets, the origin is located at the midpoint between the discharge tube exits. For single jets, the origin was located at the center of the discharge nozzle exit. The coordinate used to describe position in the flow direction was z , and the coordinate normal to the flow direction was x . These nonstandard coordinates were chosen so that the coordinate system would correspond to coordinates used in the Data Translation image processing system and also be right handed.

Rotameters and needle valves were used to measure and regulate the two jet flow rates independently, and solenoid valves were used to turn the flow on and off. An almost constant pressure head of dyed water was maintained using two head tanks approximately 3 meters above the jet discharge tubes. The small change in

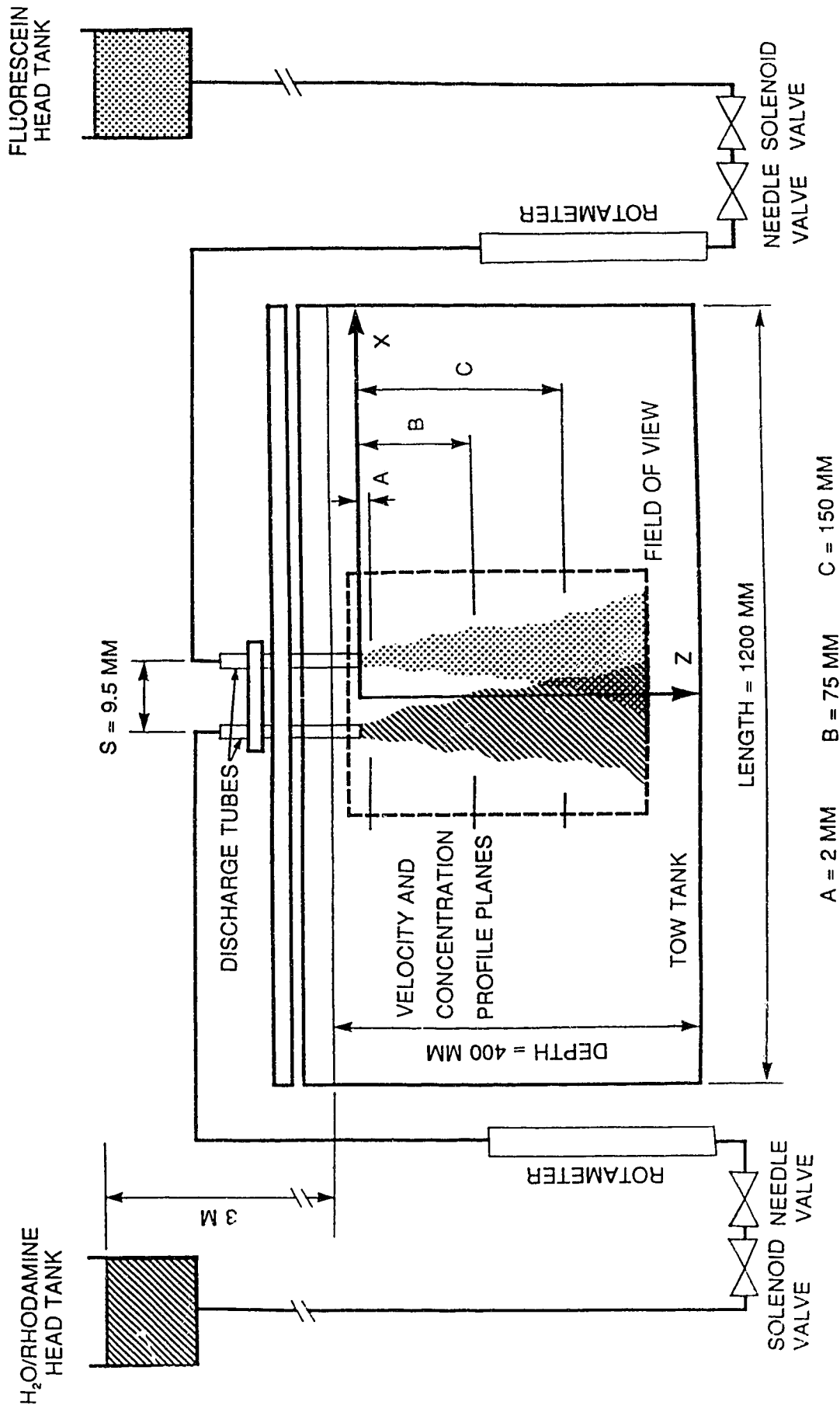


Figure 5-1: Flow apparatus

head from the tank level dropping during a run caused no measurable change in jet flow rate. The jets discharged downward into a glass tow tank, 1.2 meters long and 0.4 meters wide, filled with water to a depth of $d = 40.6$ cm (16"). The discharge tubes were held 3.8 cm (1.5") below the tank water level, leaving 36.8 cm (14.5") between the end of the discharge tube and the bottom of the tank. The jet flow rate for all tests was 11.0 ± 0.2 ml/s, producing a mean nozzle velocity of 18 cm/sec.

The discharge tubes, shown in Figure 5-2, were made from 9.5 mm (3/8") o.d. thin wall brass tubing with an inside diameter of 8.8 mm (.347"). The discharge tube center lines were spaced 3 diameters or 2.9 cm (1.125") apart. The Reynolds number of the flow discharging from the tubes, based on mean velocity and discharge tube inside diameter was $Re_D = 1600$. To create initially laminar jets, the 28 cm (11") long tubes were used with nothing added to them to generate turbulence. To create initially turbulent jets, turbulence generators were installed in the discharge tubes. These turbulence generators, also shown in Figure 5-2, were made by drilling eight 1.3 mm (0.052") diameter holes in round plastic plugs sized to press fit in the brass discharge tubes. Inserted 2.5 cm (1") in from the outlet end of the tube, a turbulence generator caused an initially turbulent jet to emerge from the discharge tube. The effect of the turbulence generators can be seen by comparing Plate 4-1 (initially laminar jets) and Plate 4-2 initially turbulent jet at the same flow rate).

Both the dyed jet water and the clear water in the tow tank were held at room temperature (22 ± 2 °C). The concentration of dye in the jet fluid was low, $1 \cdot 10^{-6}$ mol/l to $5 \cdot 10^{-6}$ mol/l, so the density difference between the jets and the background

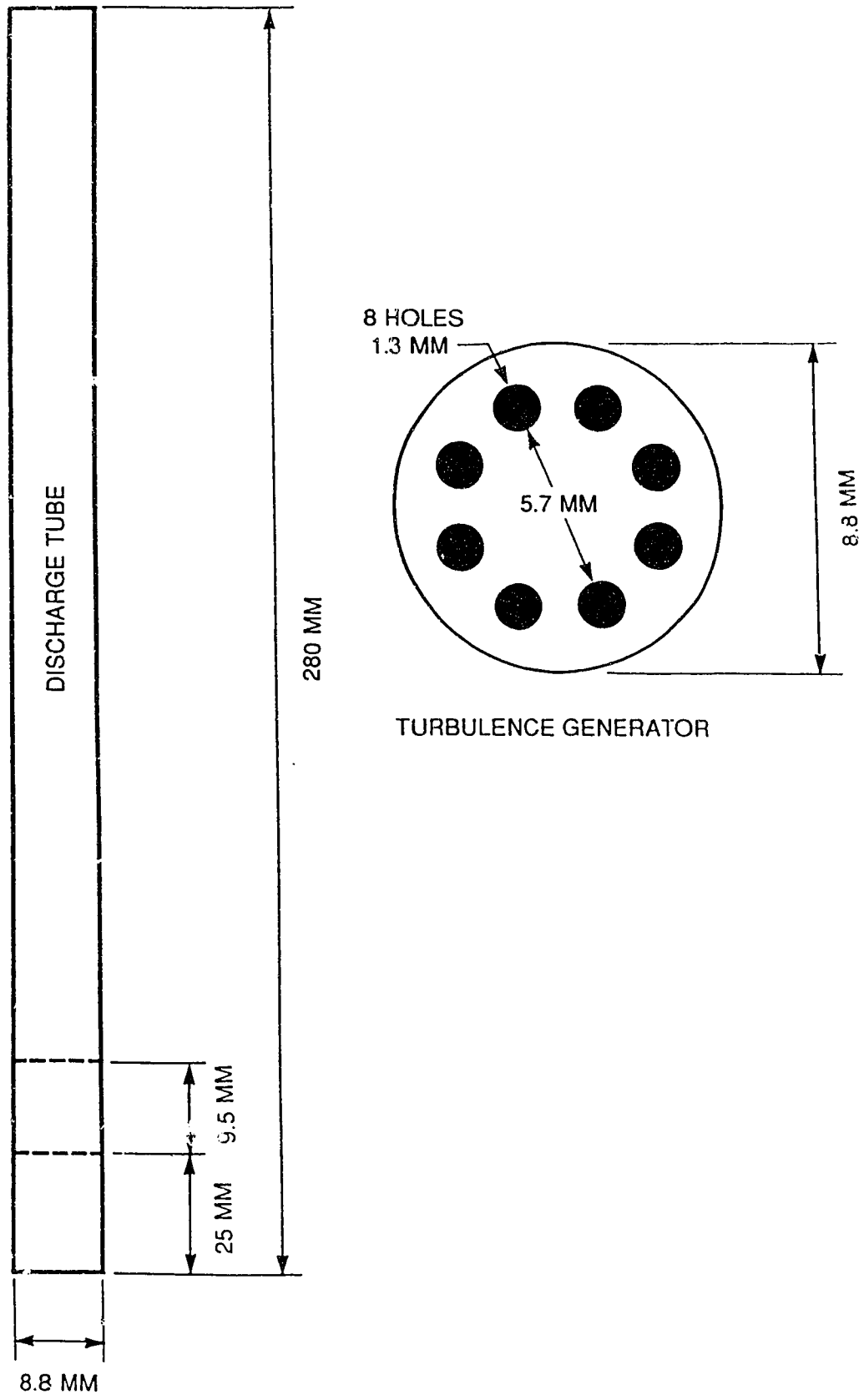


Figure 5-2: Discharge tubes and turbulence generators

fluid was negligible. The jets were purely momentum driven and not affected by buoyancy.

5.3 Jet Configurations

Four different jet configurations were studied:

1. A single jet with no turbulence generator installed.
2. A single jet with a turbulence generator installed, eg: Plate 4-2.
3. Two jets discharging parallel to one another, center lines separated by 3 tube outside diameters (28.6mm, 1-1/8"), no turbulence generators installed, eg: Plate 4-1.
4. Two parallel jets with both having turbulence generators installed.

The jets created without turbulence generators have a laminar flow region within a short distance of the nozzle and will be referred to as "laminar" jets. The jets created with turbulence generators installed will be referred to as "turbulent" jets. The single jet cases were visualized using disodium fluorescein. For the two-jet cases, disodium fluorescein was used to dye one jet, while the other jet was clear, undyed water. This method was intended to visualize jet interactions without requiring color separation. Since only one jet was marked with dye, no direct information about the second jet could be determined. Its effect on the dyed jet could be inferred by comparing the two jet case to the equivalent single jet case.

5.4 Velocity Measurements

To perform mass balances on dyed jet fluid the jet mean velocity distribution is required. Work proceeding in parallel to this study at the University of Alberta's

Mechanical Engineering Department has involved Laser Doppler Velocimeter (LDV) studies of submerged water jets. Using this equipment, velocity measurements were made of the same jets and experimental configurations used in this study.

The system used was a single component 2 beam system with a He-Ne 16 mW laser and TSI optics and counter processor. Stepper motors controlled by a microcomputer positioned the probe. Refer to Zelt (1991) for details.

Velocity measurements were taken in the same plane of symmetry illuminated by the light sheets in the visualization experiments. Mean and fluctuating velocity profiles were measured at downstream locations of $z/D = 0.23, 8.5$ and 17.0 ($z = 2$ mm, 75 mm and 150 mm). These three locations were chosen to study the jet velocity at three key locations:

- 1) at the nozzle exit,
- 2) where the jets are just beginning to merge, and
- 3) where the jets have almost completely merged.

The flow was sampled and averaged for 30 seconds at each of 20 to 25 points spaced evenly across the profiles.

The velocity data taken near the discharge tube outlet, $z/D = 0.23$, were used to determine the effect of the turbulence generators on the flow in the tubes. The jets are not interacting at this location, so there are only two cases to examine. The mean velocity profiles for both jets at $z/D = 0.23$ are shown in Figure 5-3.

The mean velocity profile for the laminar jet is symmetric about the discharge tube center line, and shows the high centerline velocities one would expect in laminar

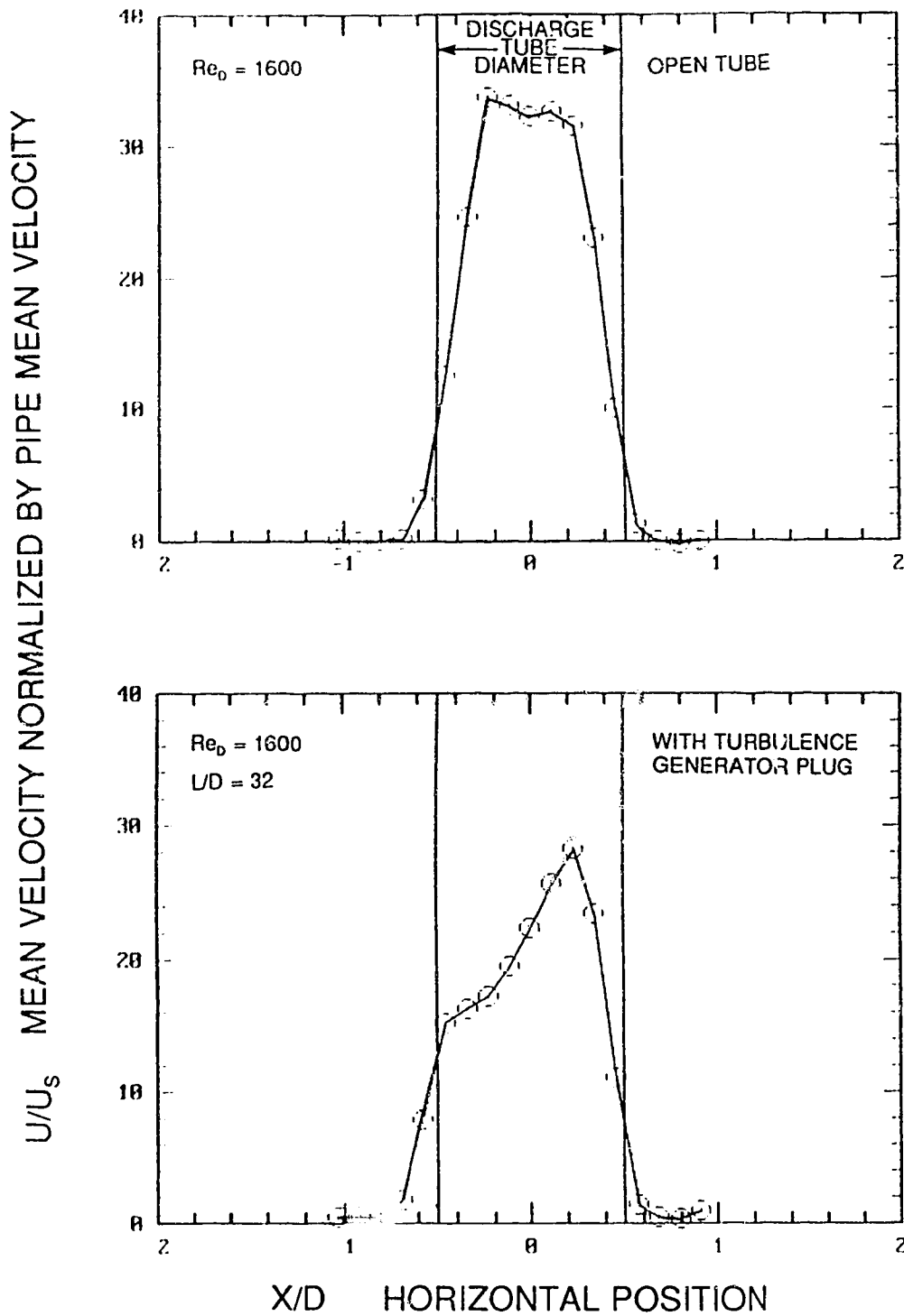


Figure 5-3: Mean velocity profiles of laminar and turbulent jets at $Z/D = 0.23$ (2 mm) with plug at $L/D = 2.9$ inside tube.

pipe flow. However, the profile does not show the parabolic shape of fully developed laminar flow. This is not surprising because the discharge tube length to diameter ratio, $L/D = 32$, was not enough for fully developed laminar flow.

The mean velocity profile of the turbulent jet is not symmetric and does not show the uniform velocity distribution of fully developed turbulent pipe flow. The maximum velocity was located off of the tube center line, close to the tube wall. The multiple jets created within the discharge tube by the turbulence generators probably deflected as they entrained one another and the resulting flow configuration was nonuniform. The turbulence generators do not simulate turbulent pipe flow, but this was not their purpose. They were intended to perturb the flow so that the jet would become turbulent and start entraining fluid immediately. No attempt was made in either the laminar or turbulent jets to adjust and refine the flow discharging from the tubes.

The fluctuating velocity profiles at the jet exit, $z/D = 0.23$, for both the laminar and turbulent jets are shown in Figure 5-4. The turbulent jet had RMS velocity fluctuations greater than 25% of the mean discharge velocity across the entire width of the exit diameter. The laminar jet had RMS velocity fluctuations of less than 5% of the mean exit velocity in the high speed core of the flow. However, there are large RMS velocity fluctuations greater than 35% of the pipe area-averaged velocity in the high shear regions at the jet edges. It was surprising to find these high velocity fluctuation levels so close to the discharge tube exit because visualization experiments showed that the laminar region of the jet persisted for at least 4 or 5 jet

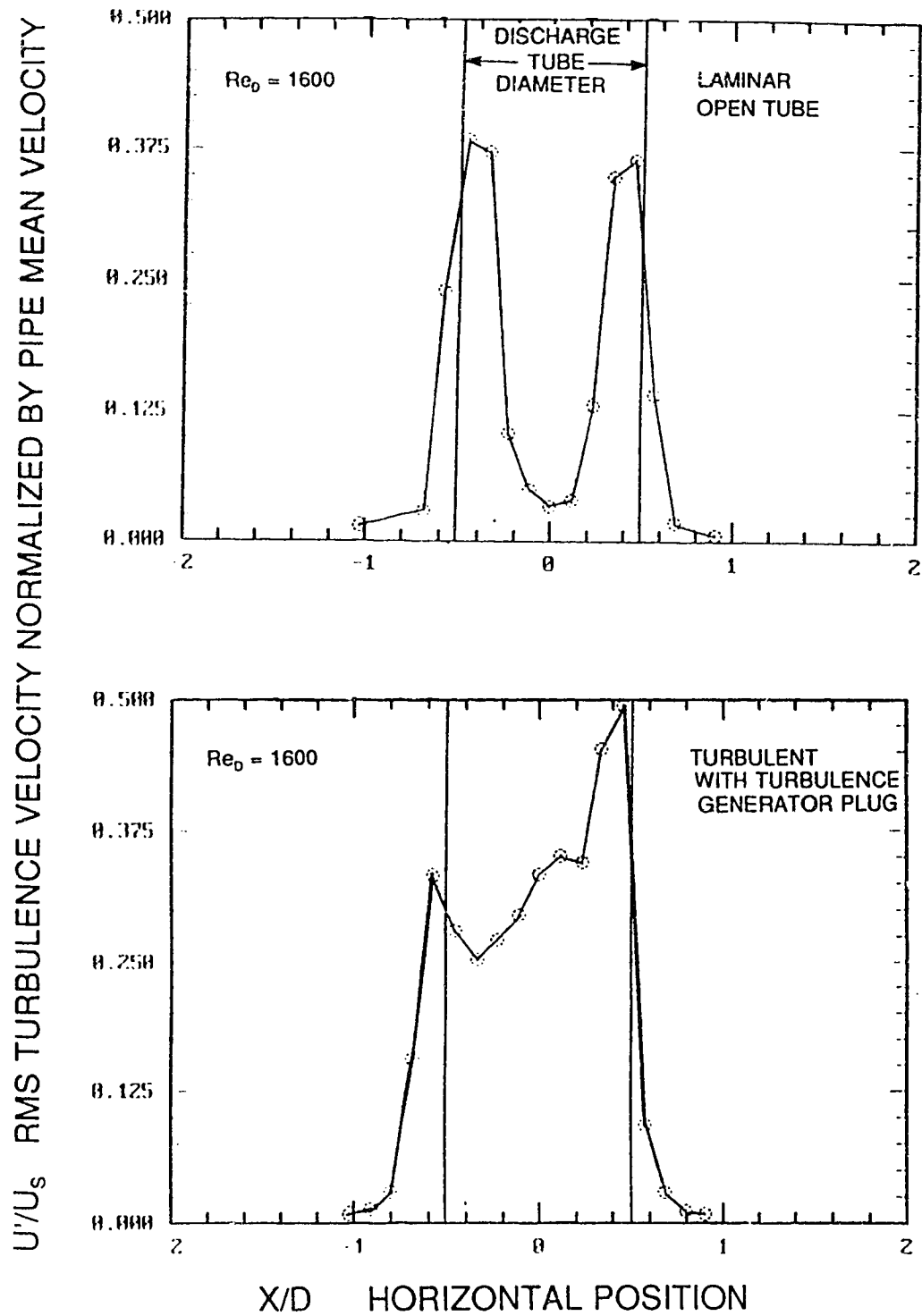


Figure 5-4: RMS turbulence velocity profiles of laminar and turbulent jets at $Z/D = 0.23$ (2 mm).

diameters further downstream. Apparently, these large velocity fluctuations did not cause an immediate onset of turbulence in the free jet core. These RMS velocity fluctuations were perhaps caused by the jet flapping back and forth very slightly or by waves in the edge of the laminar region.

Velocity profiles for single and interacting turbulent jets are shown in Figures 5-5 and 5-6. These profiles were taken at $z/D = 8.5$ ($z=75\text{mm}$) and $z/D = 17.0$ ($z=150\text{ mm}$) respectively. Gaussian distributions have been plotted with the velocity data for single jets. The Gaussian distributions were fitted through the measured center line velocity U_0 at $z/D = 0$ and through the average jet half widths of velocity, $U = U_0/2$ at $x/D = \pm \delta_w$. The Gaussian distribution is a good approximation for the mean velocity of the single turbulent jet at $z/D = 8.5$, but is not as good an approximation at $z/D = 17.0$. The mean velocity of the single jet at $z/D = 17.0$ appears to have shifted to the left of the discharge tube centerline by about $0.5D$.

5.5 Zero Interaction Jet Model

The simplest model to predict the behavior of the interacting turbulent jets is a zero interaction entrainment model in which the growth of each jet by entrainment is unaffected by the presence of the other jet. This was originally conceived as the simplest theory which conserved momentum in the jets. However, it was later discovered that this concept has received fairly extensive treatment in the literature. As was shown in the lucid discussion by Knystautas (1964) and in Pani and Dash (1983a), Reichardt's hypothesis can be used to develop superposition of momentum for a free jet with no pressure gradients or applied shear. Reichardt examined large

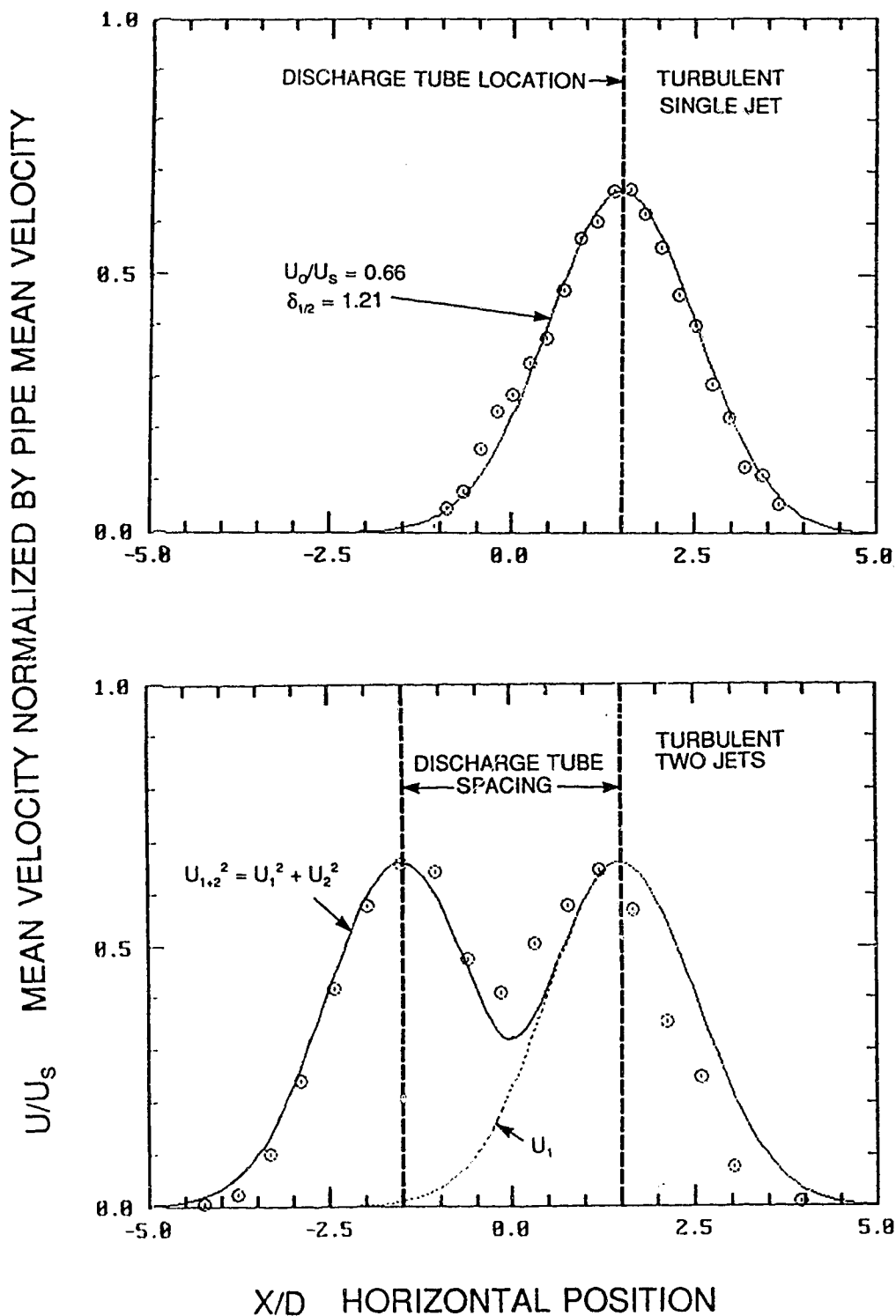


Figure 5-5: Mean velocity profiles for single and interacting turbulent jets at $Z/D = 8.5$ (75 mm).

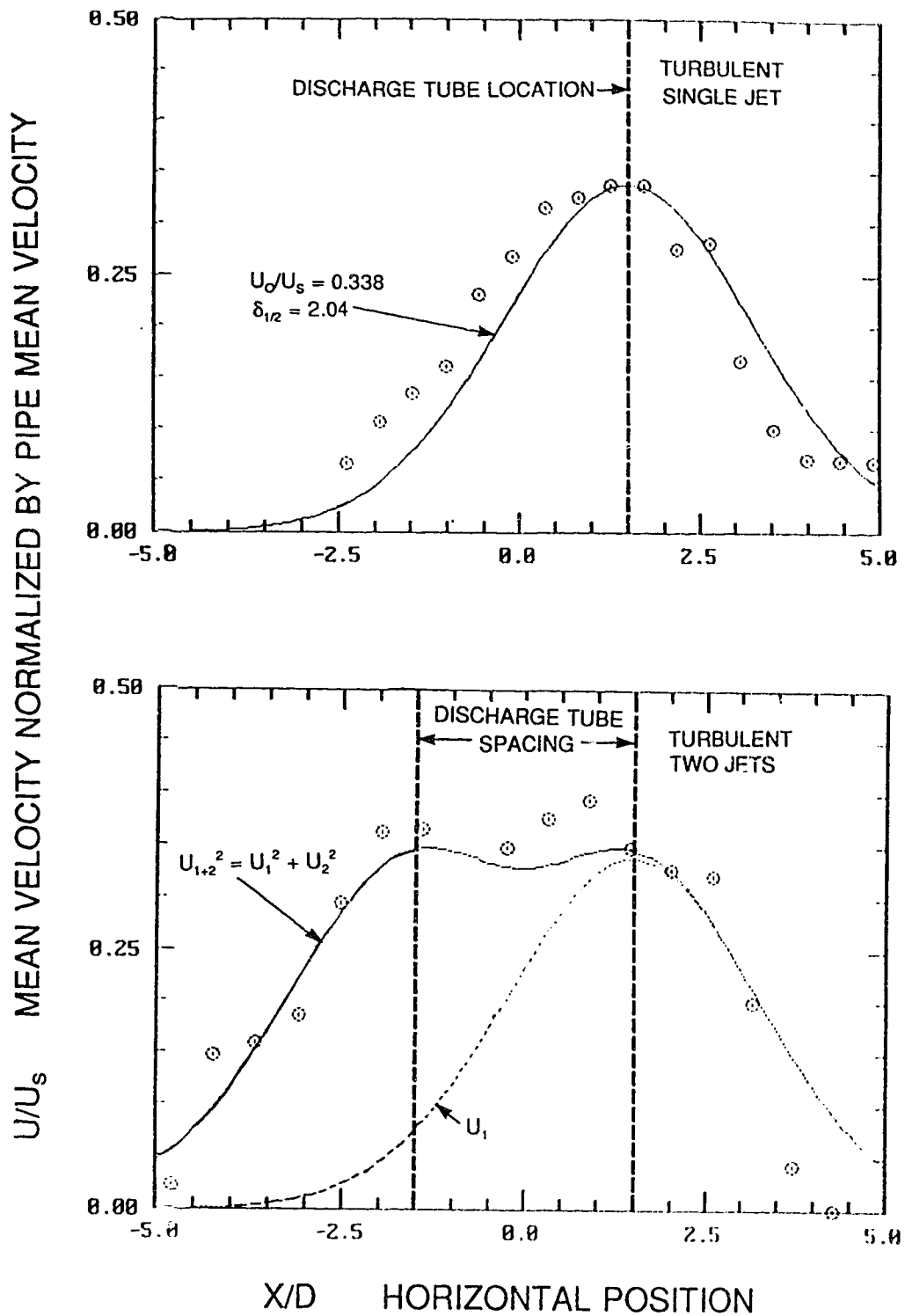


Figure 5-6: Mean velocity profiles for single and interacting turbulent jets at $Z/D = 17$ (150 mm).

quantities of experimental data and observed that jet velocity profiles are well described by Gaussian distributions. He worked backwards and determined that a Gaussian profile is produced when the ratio of turbulent shear stress to the downstream momentum gradient in the radial direction was a function of downstream distance only. This form of the turbulent shear stress leads to equations of motion which are linear in \bar{u}^2 for free jets with no pressure gradients. The streamwise momentum contribution from the fluctuating component of \bar{u}^2 is an order of magnitude smaller than the contribution from the mean component, so

$$\bar{u}^2 = \bar{U}^2 \quad (5.1)$$

For two identical jets, this implies that the squared mean velocity distributions of the two individual jets can be added at each point to give the mean square velocity distribution of the combined jets, i.e.:

$$\bar{U}_{1+2} = \sqrt{\bar{U}_1^2 + \bar{U}_2^2} \quad (5.2)$$

This model is shown by the solid lines in the interacting jet velocity profiles of Figures 5-5 and 5-6. The Gaussian distributions fitted to the single jet profiles were combined using point-wise addition of momentum as described above.

This simple model does predict the limited amount of velocity data shown remarkably well, except that the right hand jet in Figure 5-5 seems to have been sucked toward the left hand jet, with a center line displacement of about 0.5 D at

both $z/D = 8.5$ and $z/D = 17.0$. Small pressure gradients in the flow field may have caused these center line displacements. Figure 5-7 shows the same model at $z/D = 8.5$, but the center line of the right hand Gaussian distribution has been shifted half a diameter to the left, $-0.5 D$. Figure 5-8 shows the same correction at $z/D = 17.0$. The good agreement which results from this small displacement suggests that jet interaction may be well described by this simple model derived for zero pressure gradients, but with a correction for center line displacement. This simple zero interaction entrainment concept will be used in the next section to model the mean concentration distribution in interacting jets.

The measured RMS velocity fluctuations for the single and interacting jets at $z/D = 8.5$ and 17.0 are shown in Figure 5-9. The 30 second time averages produced some variability but the single jet data shows some evidence of the characteristic weakly bimodal profile expected from previous studies described in List (1982a, 1982b). Longer time averages at each point for all LDV data should result in a decrease in the scatter, and future work should probably be done with 100 second averages.

5.6 Eulerian Time Averaging of Jet Concentration

Traditionally, studying the fluctuating concentration field has meant studying the time averaged concentration properties at a single point or perhaps a few simultaneous points using some sort of concentration detector. Mapping the entire concentration field meant sequentially moving a probe to different points in the flow, usually no more than a hundred locations. Using video images of full-field flow

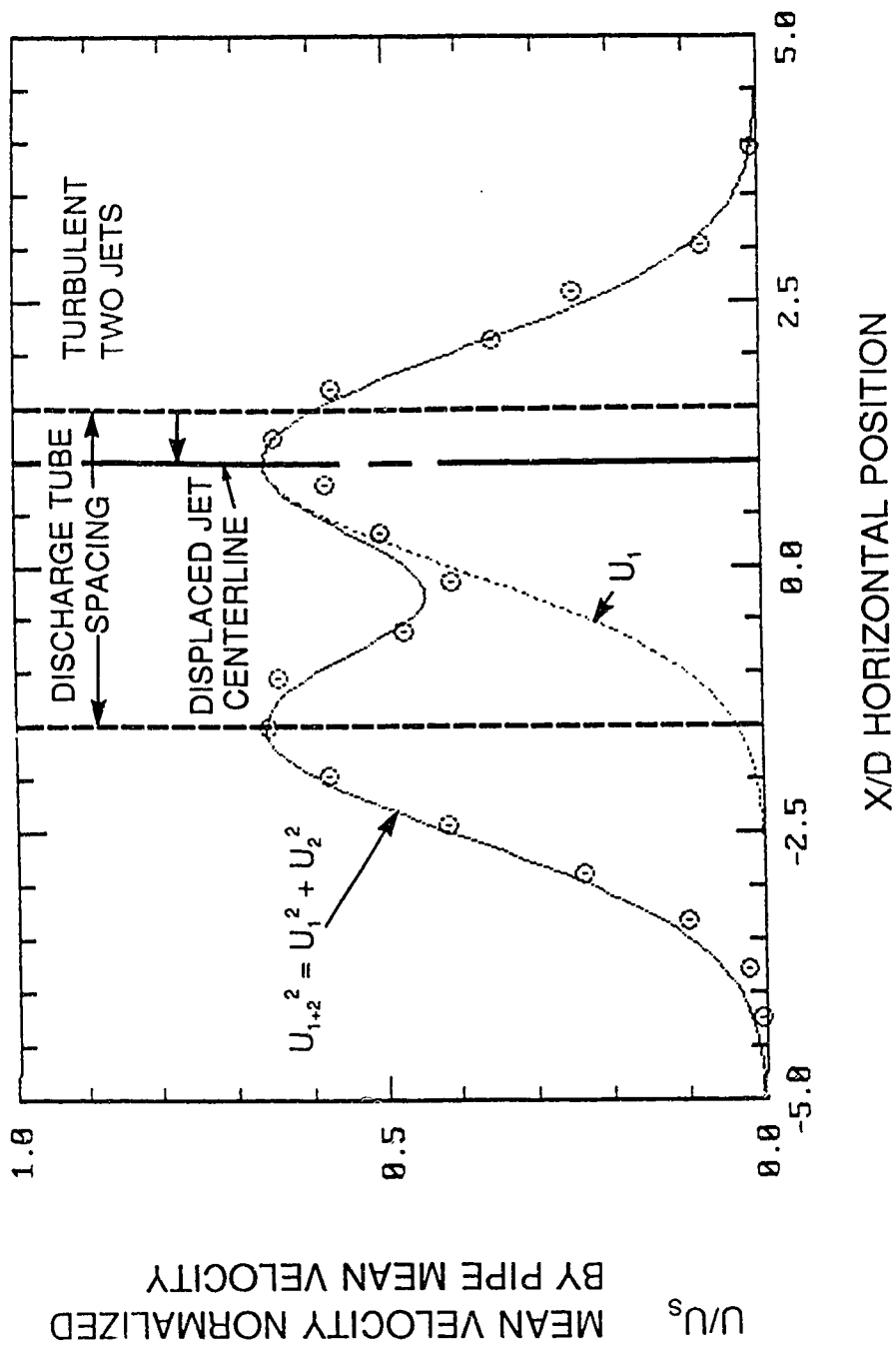


Figure 5-7: Effect of displaced center line on zero interaction model at $Z/D = 8.5$ (75 mm).

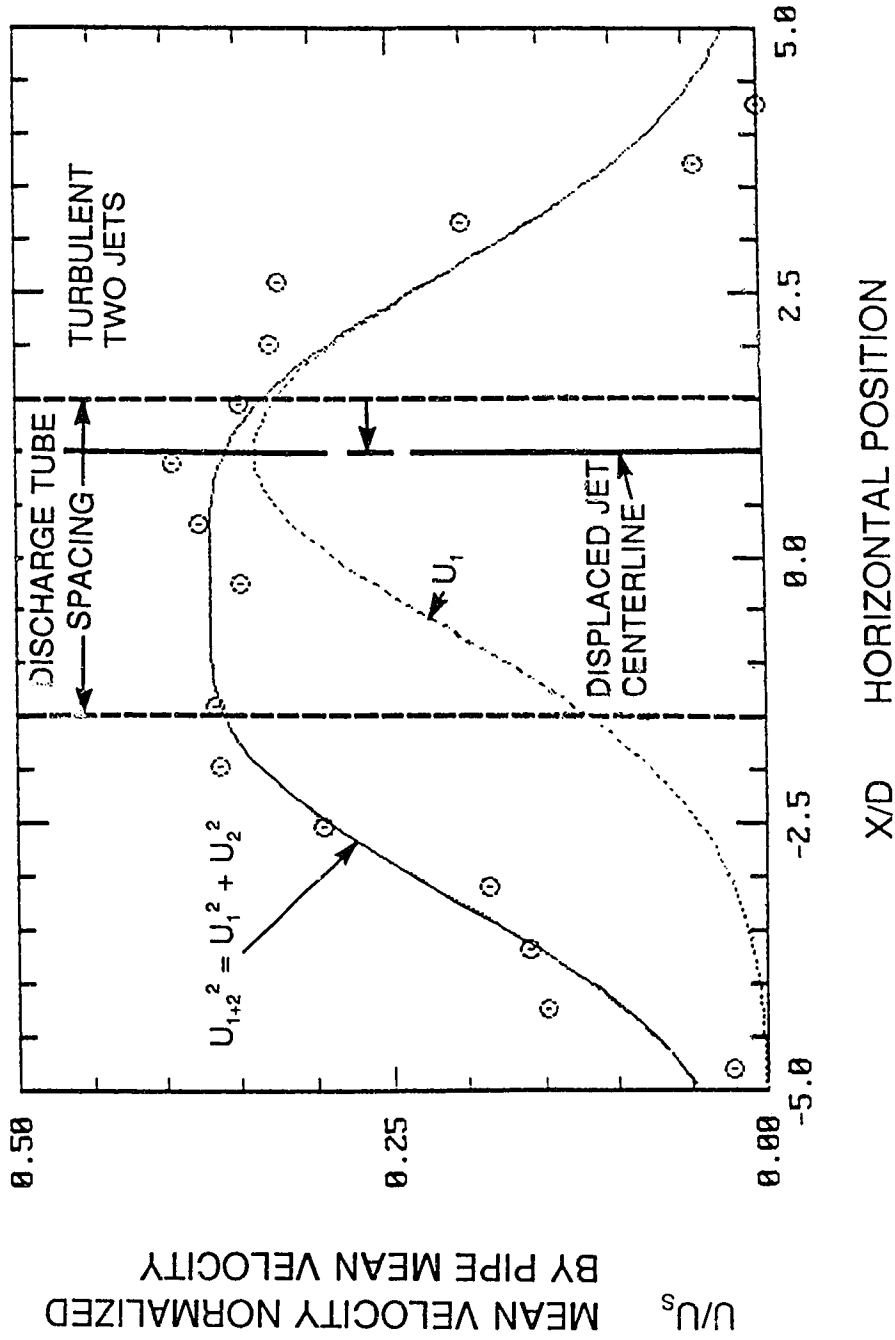
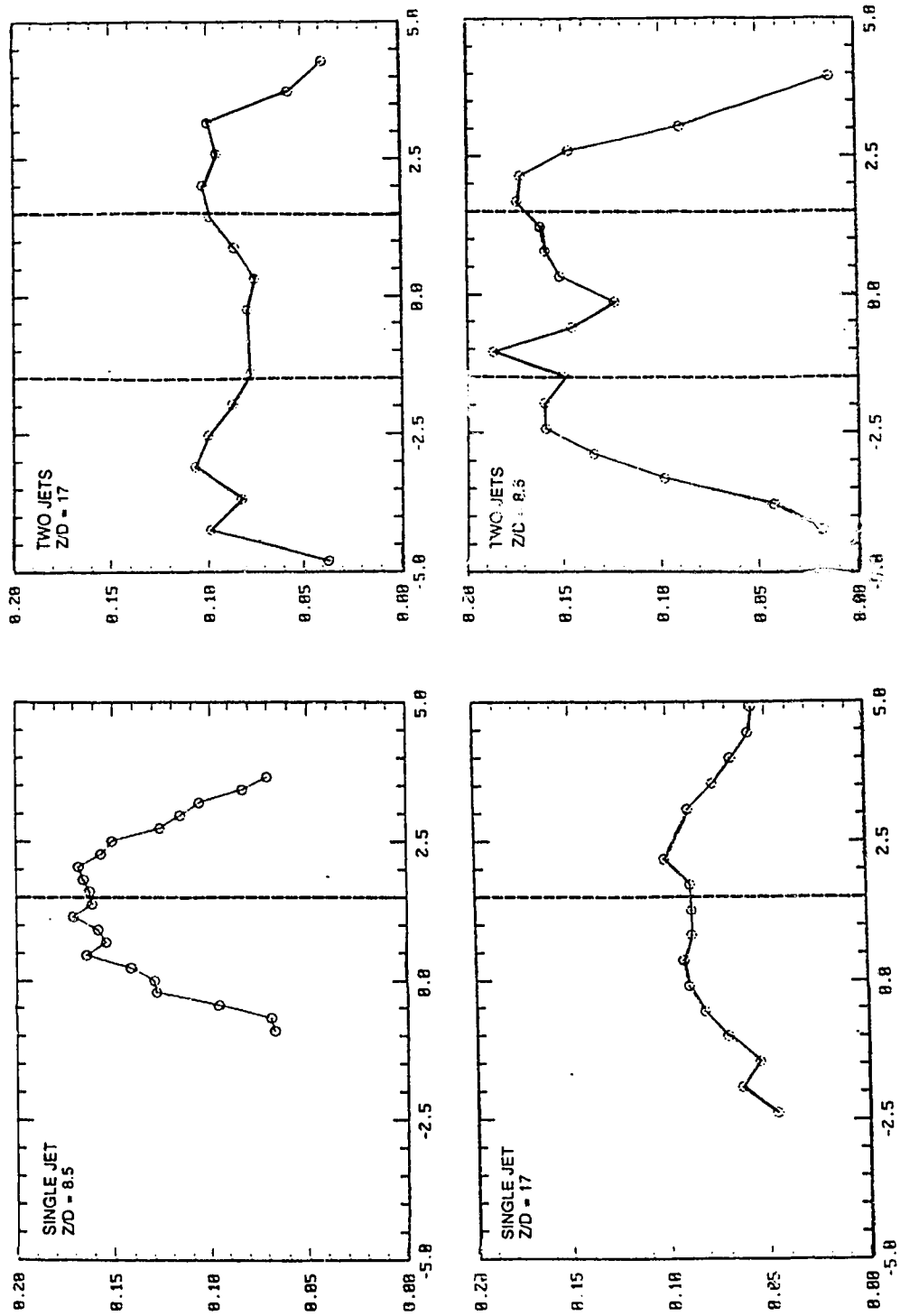


Figure 5-8: Effect of displaced center line on zero interaction model at $Z/D = 17$ (150 mm).

U/V_s RMS VELOCITY FLUCTUATIONS NORMALIZED
BY PIPE MEAN VELOCITY



X/D HORIZONTAL POSITION

Figure 5-9: RMS velocity fluctuation profiles of single and interacting jets, all jets with turbulence generator plugs installed in discharge tubes.

visualization in the present study, each pixel in a concentration field image can be used as a concentration detector. Time averaging the concentration at each point (pixel) over a large number of time sequence images allows the traditional time averaged concentration field properties to be measured at almost a quarter of a million points simultaneously - a substantial improvement in spatial resolution.

In this study, images were acquired using a 35 mm SLR camera with a power winder capable of approximately 3 images per second. Reserving a few slides from each roll of film for background and light sheet images meant that a typical run consisted of 25 to 33 jet images over a time of about 8 to 10 seconds. One run, the single turbulent jet, was performed 3 separate times for a total of 100 slides over a total ensemble time of about 35 seconds. As mentioned in the previous section, 30 second averages were used for the LDV measurements. The length of time, then, that the existing concentration data could be time averaged over was substantially shorter than desired for all but one run.

Because of the volume of data available, the point-wise time averaged concentration profiles were computed only for the two downstream positions of $z/D = 8.6$ and 17.1 , corresponding to the velocity profiles discussed in the previous section. The two cases discussed here are the single turbulent jet and interacting turbulent jet cases. The interacting turbulent jets were visualized with disodium fluorescein in one jet and clear water in the other.

Mean concentration profiles, computed at a few points across the jet (roughly corresponding to the LDV sampling points), are shown in Figures 5-10 and 5-11. As with the velocity data, Gaussian distributions have been plotted with half widths δ_{vC} computed by curve fits to the concentration data for single jets. These distributions were fitted through the measured center line concentration, C_o , at $z/D = 0$, and through the average jet half widths, $C = C_o/2$ at $x/D = \pm \delta_{vC}$.

The Gaussian distributions are good approximations to the measured mean concentration profiles for the single turbulent jet at both $z/D = 8.6$ and $z/D = 17.1$. Previous experiments have found that the profile of a scalar quantity such as concentration or temperature falls off more slowly with horizontal position than the velocity profile in a round jet. Previous studies have shown this ratio to be about 1.4 for fully developed jets, as in Schlichting (1979), p. 753 or List (1982a, 1982b). For the turbulent single jet in this study, $\delta_{vC}/\delta_{v_u} = 1.01$ at $z/D = 8.5$ and $\delta_{vC}/\delta_{v_u} = 1.06$ at $z/D = 17$. A dye mass balance was performed to check this discrepancy. Gaussian profiles were assumed for both the velocity and the concentration distributions. The profiles were fitted to the measured values of C_o and U_o and half widths δ_{vC} and δ_{v_u} . The dye mass flux was integrated over the entire jet. Mass was found to be conserved using this technique at $z/D = 8.5$, so the measured ratio, $\delta_{vC}/\delta_{v_u} = 1.01$, is probably correct. The generally accepted ratio of 1.4 is for fully developed jets, not for the developing jets investigated in this thesis.

A similar mass balance was also performed at $z/D = 17.0$. Using the measured peaks and half-widths to define the Gaussian profiles, the mass balance

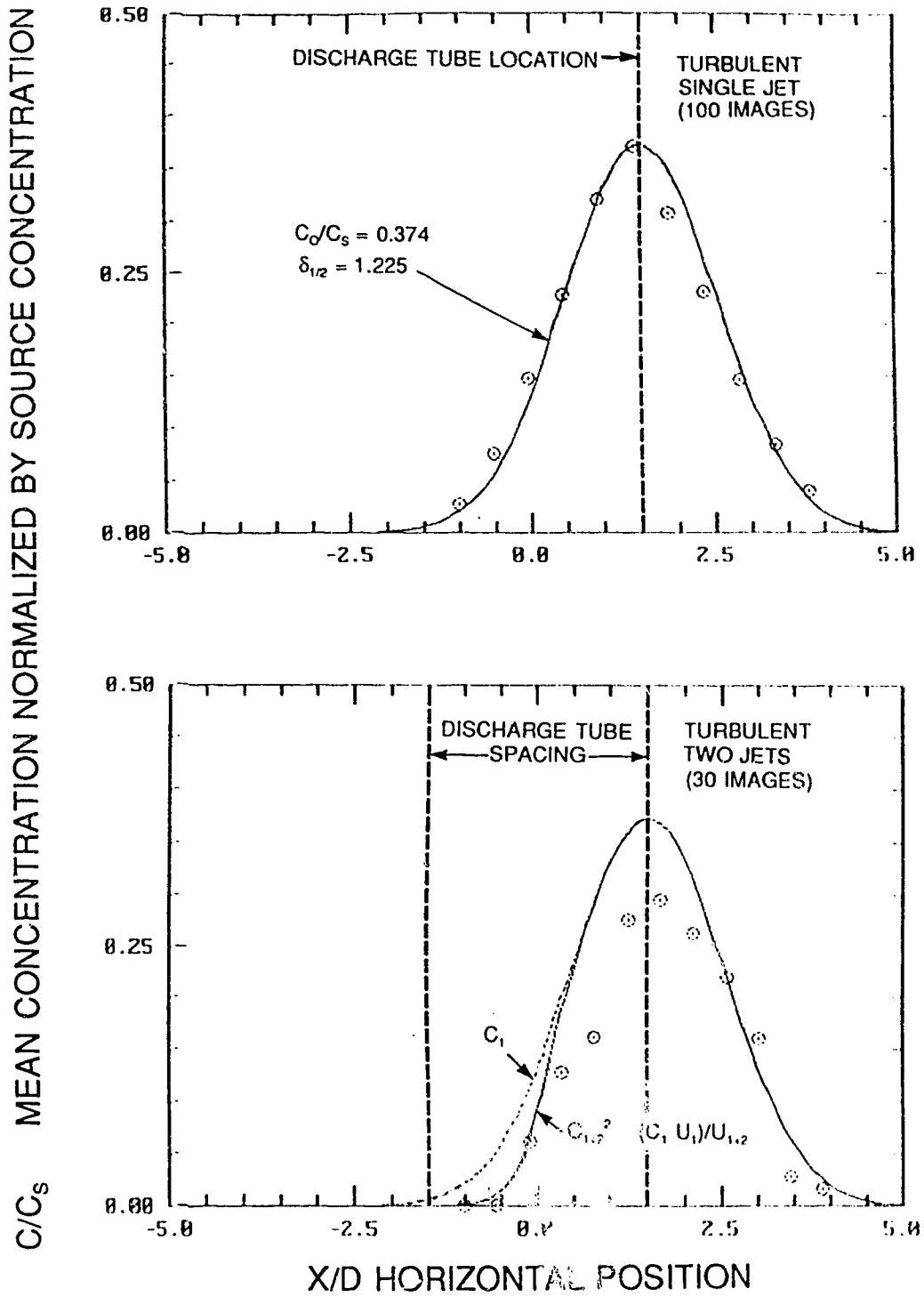
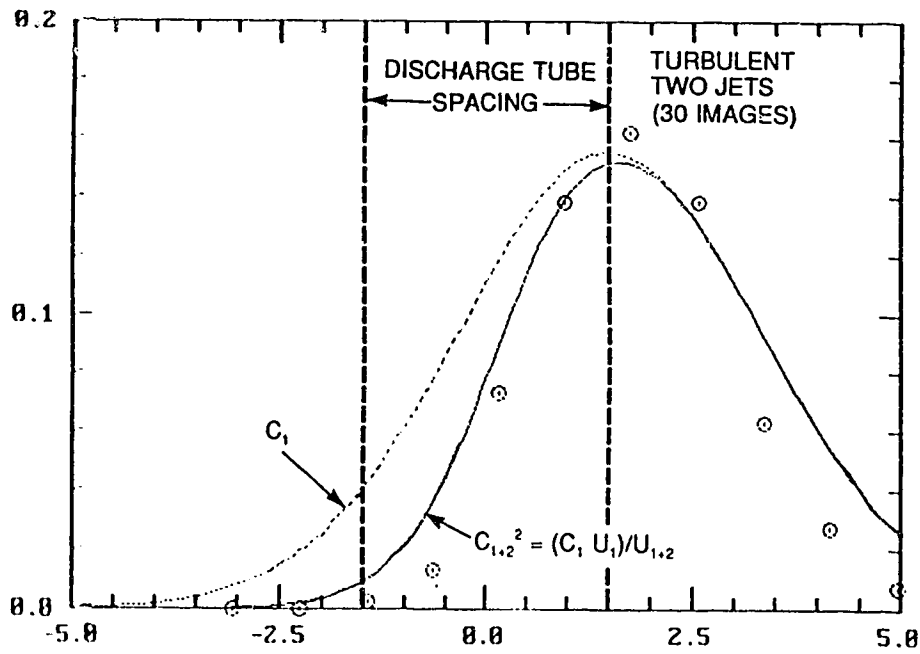
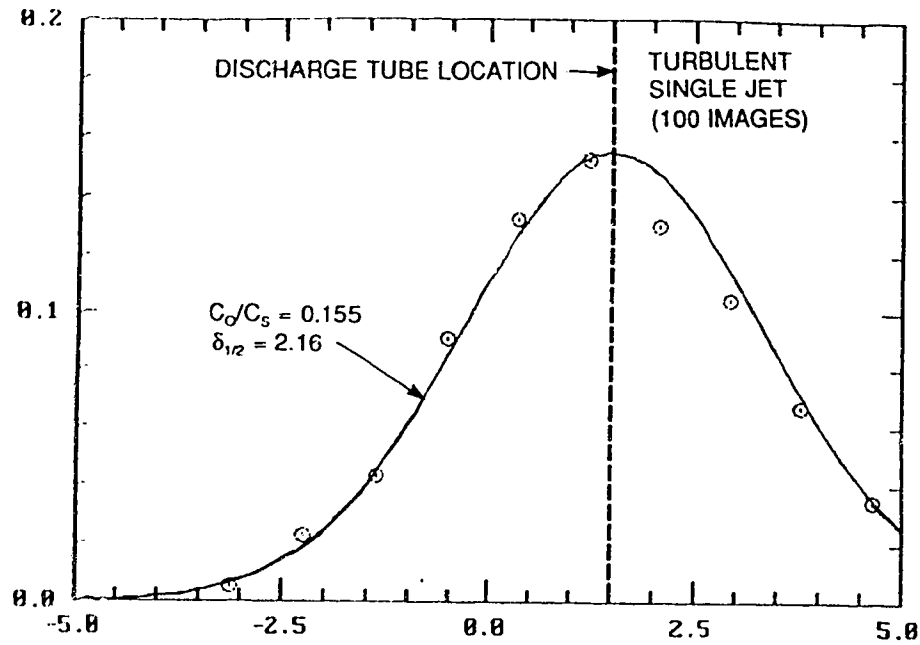


Figure 5-10: Mean concentration profiles for single and interacting turbulent jets at $Z/D = 8.6$ (76 mm).

C/C_S MEAN CONCENTRATION NORMALIZED BY SOURCE CONCENTRATION



X/D HORIZONTAL POSITION

Figure 5-11: Mean concentration profiles for single and interacting turbulent jets at $Z/D = 17.1$ (152 mm)

failed; only 70% of the dye mass flux was observed. The discrepancy was most likely due to the small ensemble size of 100 images. At the lower concentration levels, the small ensemble was not sufficient to adequately define the outer edges of concentration profile.

The simple zero interaction entrainment model can also be used to describe the two jet concentration distribution. If the mixing characteristics of the jets follow the assumptions necessary for Reichardt's hypothesis, then the stream wise z concentration flux from each jet should sum at each point in the flow field to conserve mass. Effectively:

$$\bar{C}_{1,2} \cdot \bar{U}_{1,2} = \bar{C}_1 \cdot \bar{U}_1 + \bar{C}_2 \cdot \bar{U}_2 \quad (5.3)$$

at each point in the flow. The velocity distribution for the two jets is known from Equation (5.1). With only one jet dyed (ie: $C_2 \equiv 0$ everywhere) then the concentration field becomes:

$$\bar{C}_{1,2} = \frac{\bar{C}_1 \cdot \bar{U}_1}{\sqrt{\bar{U}_1^2 + \bar{U}_2^2}} \quad (5.4)$$

Two curves have been plotted along with the interacting turbulent jet data in Figures 5-10 and 5-11. The solid line is the Gaussian concentration distribution from the single jet profile at that location, and the dashed line is the zero interaction model prediction of the concentration profile using the Gaussian concentration and

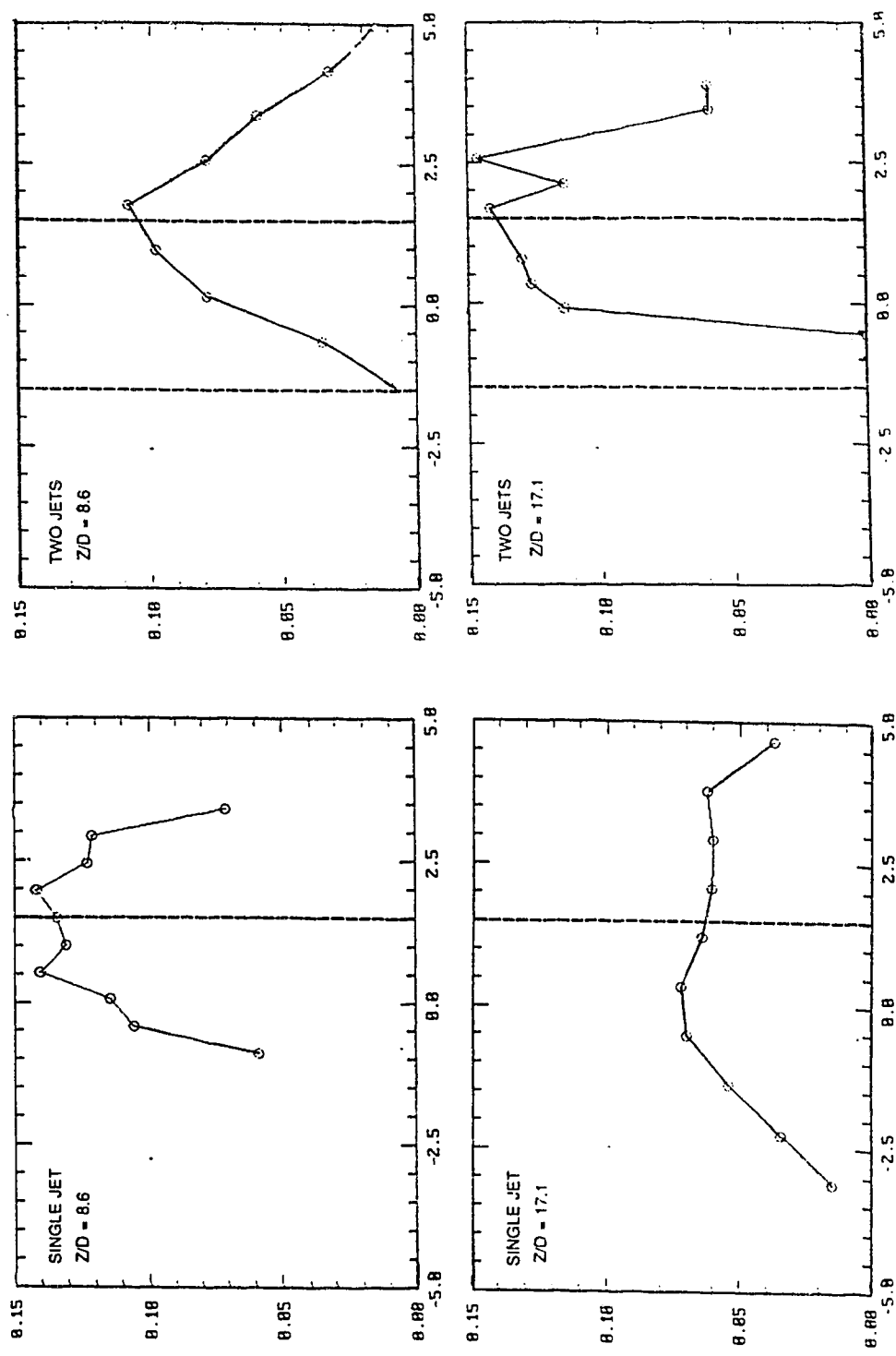
velocity profiles fitted to the single jet data.

The zero interaction entrainment model does not predict the concentration profile well. The interacting turbulent jet data is from a test with only 30 images, or approximately 10 seconds of data. It is not known whether the failure of the zero interaction model to accurately predict the interacting jet concentration profile is due to inadequacies of the model, or the small number of images used to determine the actual mean profile. It is suspected that the small sample size is the problem.

The measured concentration fluctuations for the single and interacting jets at $z/D = 8.6$ and 17.1 are shown in Figure 5-12. The weakly bimodal profile expected when looking at scalar fluctuations as opposed to velocity fluctuations is apparent. As expected, there appears to be more scatter in the interacting turbulent jet data (30 images) than in the single turbulent jet data (100 images). Future studies of time averaged concentration data should use many more images if accurate time averaged behavior is to be measured. The use of a video cassette recorder and high shutter speed video camera, rather than a slide film camera, would make acquiring these large quantities of data easier. However, these large amounts of images would result in large required image correction and storage capabilities.

5.6 Mean and Fluctuating Full Field Jet Concentration

In addition to the usual Eulerian point averages, flow visualization allows us to develop new statistical measures of the turbulence and mixing. The Data Translation image processing system measures full field instantaneous concentrations at up to a quarter of a million points in the plane of symmetry of the jet(s). The



C/C_s RMS CONCENTRATION FLUCTUATIONS
 NORMALIZED BY SOURCE CONCENTRATION

X/D HORIZONTAL POSITION

Figure 5-12: RMS concentration fluctuation profiles of single and interacting jets, all jets with turbulence generator plugs installed in discharge tubes.

simultaneous nature of all these readings permits looking at the concentration field in a number of unique ways, a few of which will be discussed in this section.

Figure 5-13 shows the type of information available about the concentration field at any instant. It shows contour plots of the instantaneous concentration field on the axis of symmetry of a single turbulent jet. Using the image processing technique for simple point measurements of the time varying concentration at select points utilizes a fraction of the information available in a typical image.

As a simple example, the mean behavior of the jet need not be inferred from the average concentration at a few points. Instead, whole images can be averaged to produce a full field concentration map of the type shown in Figure 5-14. This figure shows the mean concentration field for four of the investigated cases: a single laminar jet, a laminar jet interacting with an undyed laminar jet, a single turbulent jet, and a turbulent jet interacting with an undyed turbulent jet. This figure also shows some of the errors still present in the image processing system. Ensembles of more than 30 slides (≈ 10 seconds) are necessary for adequately determining the mean behavior of this flow configuration. In regions of high concentration gradients, such as the region near the outlet of the laminar jets, camera amplifier problems caused errors, one of which was the ringing error visible in the scan direction, between the two discharge tubes. As well, the image digitization and background correction technique used did not completely eliminate the intensity of the discharge tubes in the image. However, in the turbulent mixing regions of interest, the image processing technique can map the entire mean concentration field from a relatively

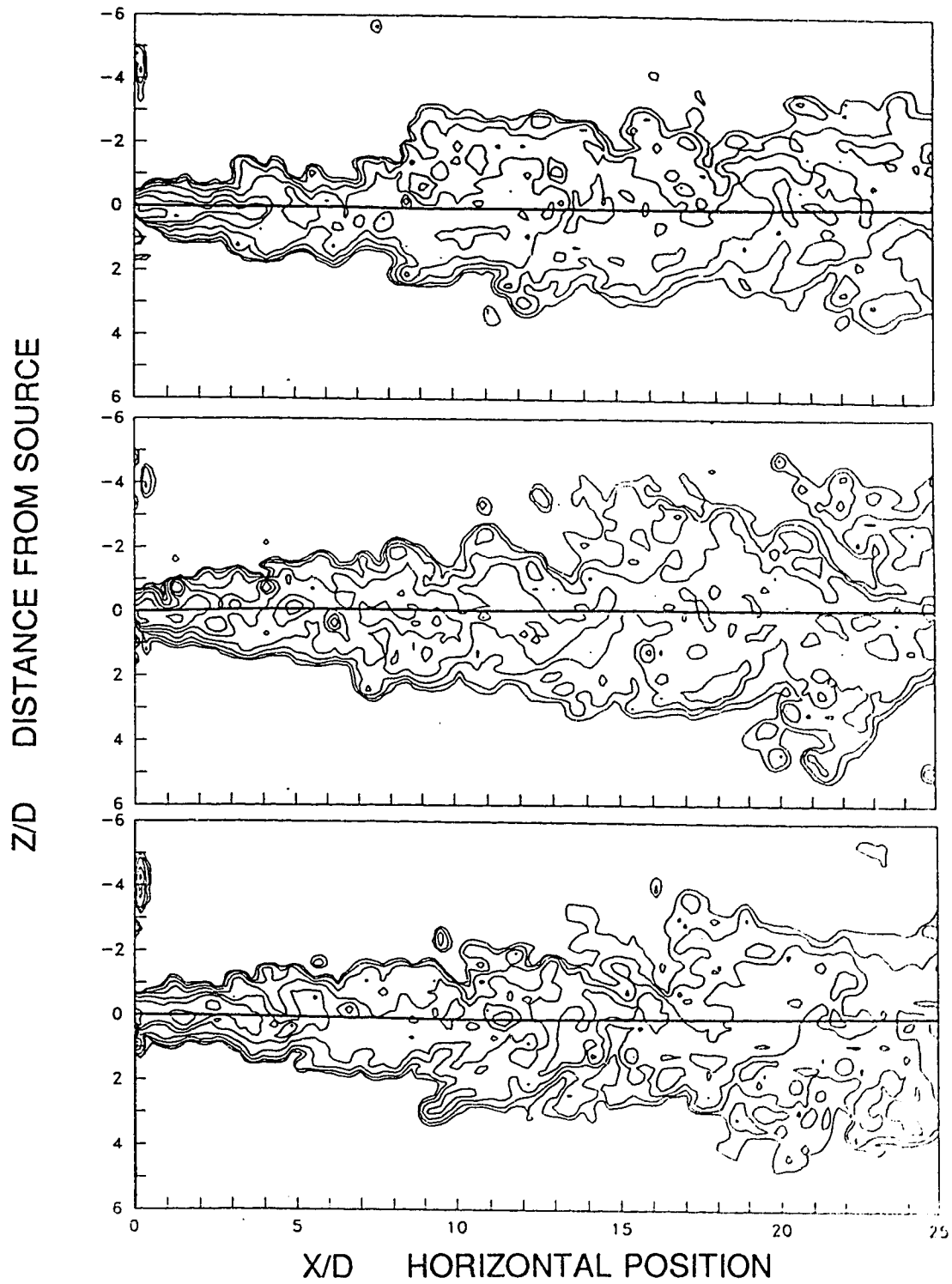


Figure 5-13: Typical (time independent) instantaneous concentration fields of a single, turbulent jet.

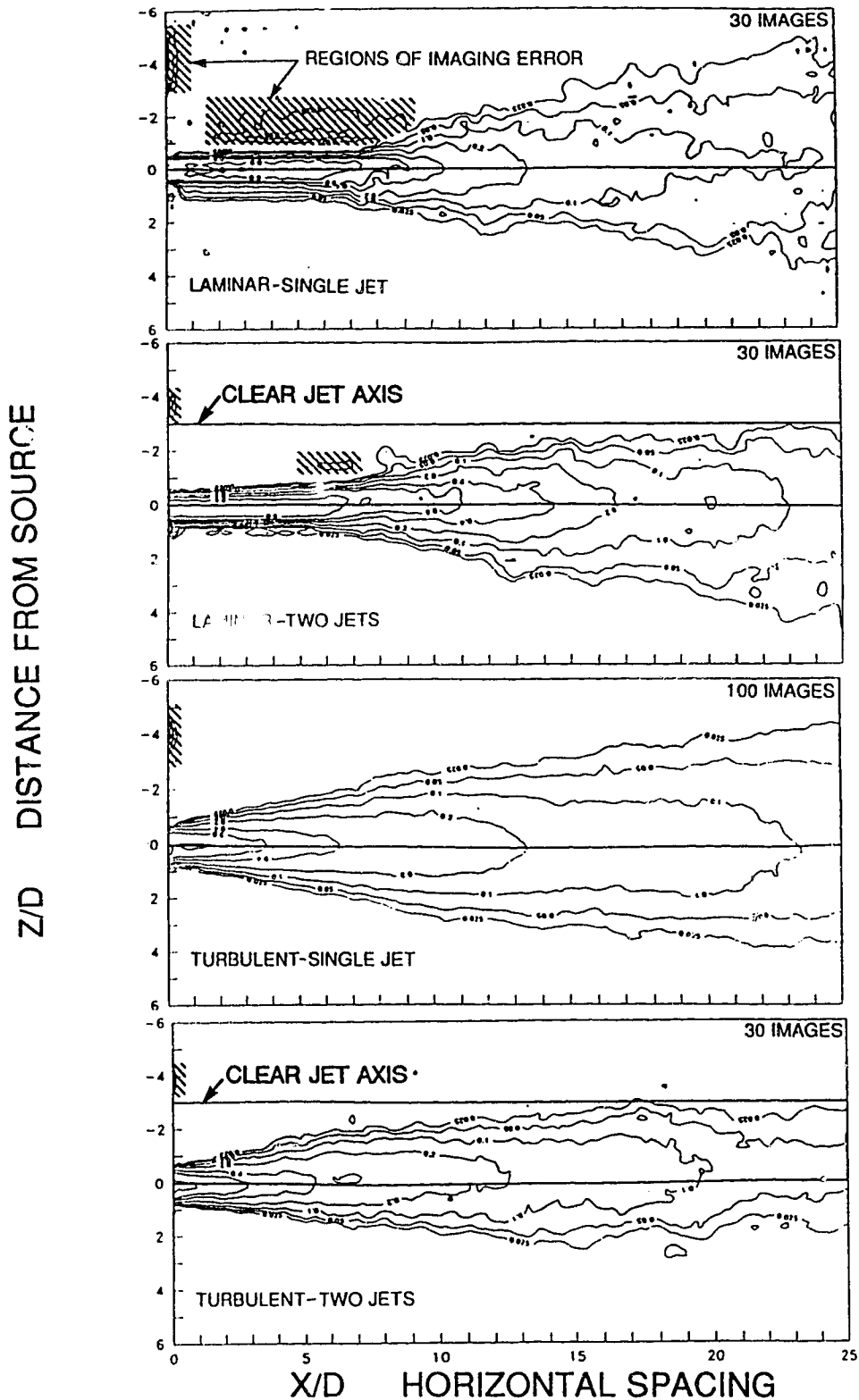


Figure 5-14: Mean concentration fields of single and interacting turbulent and laminar jets (one jet dyed only). Note that the shaded areas were affected by errors in the image processing system.

small number of images - a much faster process than mapping the field with a single concentration probe.

Knowing the entire instantaneous concentration field means that spatial correlations of concentration fluctuations can be measured in any direction and any spacing within the plane of the image. Spatially correlating concentration fluctuations was not attempted in this study, but would be an elementary problem to solve given the tools developed here.

Full-field concentration measurements also allow new ways of examining mixing processes, not previously considered. As an example, consider the contour plot of the jets shown in Figure 5-14. The lines plotted in this figure represent lines of constant concentration, or isopleths. The area within any isopleth is the mean area of the jet in the image plane which has concentration greater than or equal to the isopleth concentration. The area between any two isopleths is the mean area of the jet in the image plane which has concentration between the given isopleth values. For an axisymmetric mean jet, these areas can easily be extended to volumes of given mean concentration ranges. These mean areas could be measured using conventional point averaging techniques, and in fact could be described mathematically given the well defined Gaussian profile of a typical jet, jet spreading rates, and the principal of conservation of momentum. The image processing technique allows us to measure the instantaneous area within a given isopleth or pair of isopleths. The mean of these instantaneous areas can be computed, and knowing the instantaneous isopleth area for many images allows the definition of the spatial intensity of isopleth area

fluctuation, ie:

$$i_{th} = \frac{\sqrt{A_{th}^{\prime 2}}}{\bar{A}_{th}} \quad (5.5)$$

where

$$A_{th}^{\prime} \equiv A_{th} - \bar{A}_{th} \quad (5.6)$$

at any instant. The area fluctuation intensity might be extended to volume fluctuation intensity in flows where the mean behavior is known to be axisymmetric or 2 dimensional.

This type of information could be very informative in, say, flammability studies for gas leaks. What is the mean area covered by a combustible gas/air mixture which is within the flammability range for that gas? How much does this area vary? Figure 5-15 shows the mean and fluctuating areas for 10% concentration ranges in the same turbulent, single jet discussed above. The concentration range greater than 1.0 results from the edge enhancement error discussed in Chapter 3. It is interesting to note without further comment that the isopleth area fluctuation intensity stays relatively constant at about 20% for isopleth ranges between 10% and 90%, even though the mean area of these isopleth ranges change by two orders of magnitude.

The new ways to utilize this instantaneous full field concentration information

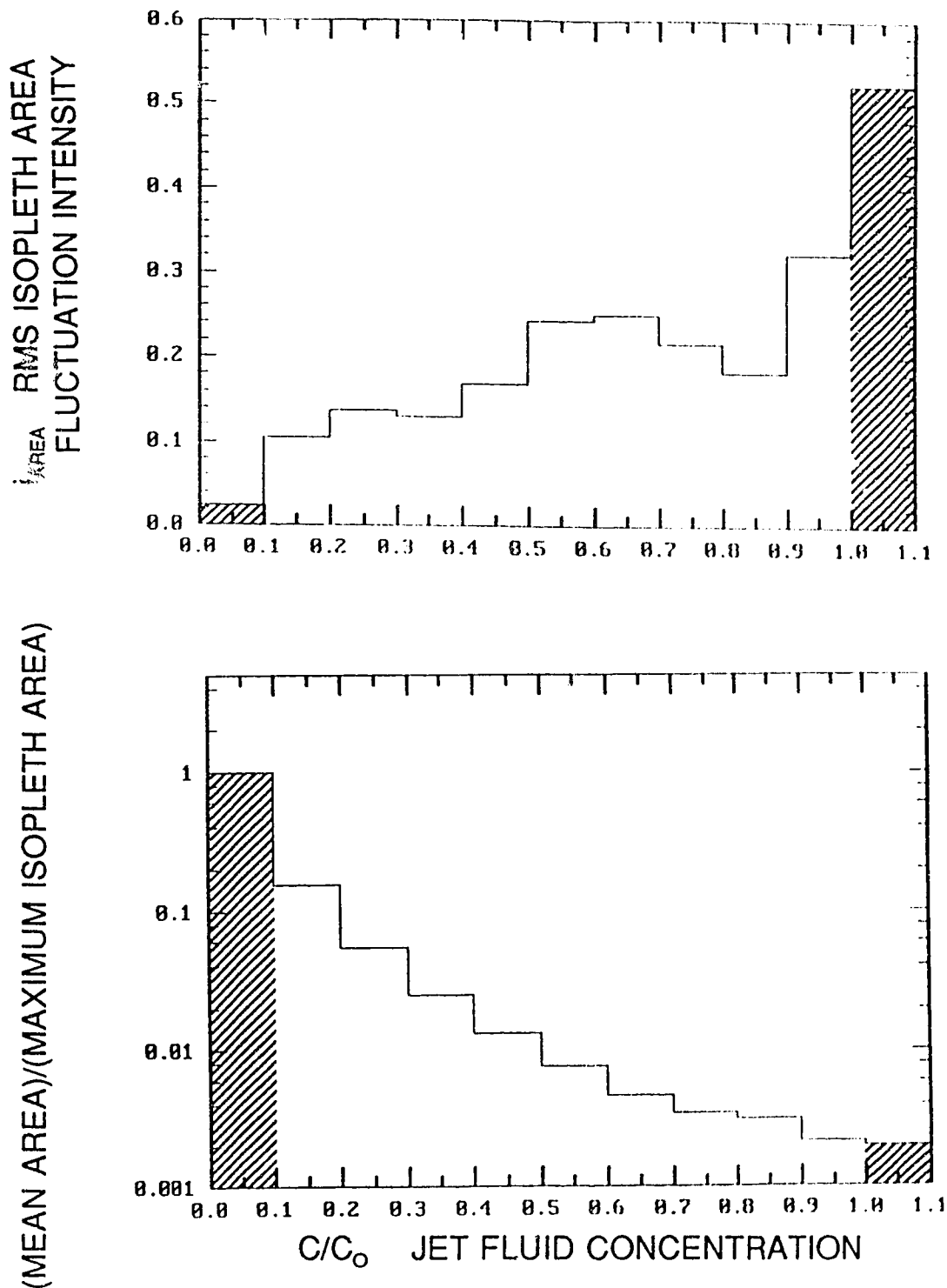


Figure 5-15: Mean and fluctuating isopleth areas for a single, turbulent jet. Note that the shaded area for $C > 1.0$ is caused by camera errors, and the shaded area for $C < 0.1$ may not be valid because not all of the jet fluid at $C < 0.1$ was contained in an image.

have only been touched upon in this study. It is hoped that new information about many different kinds of mixing configurations may be obtained with these techniques.

Chapter 6 - Conclusions and Recommendations

Objectives in scientific research change as a study evolves. When this study began, the extraction of quantitative information from flow visualization images was regarded as a minor problem, and the physics of jets a major one. While it was recognized that there probably would be a few non-linearities in the conversion from intensity to concentration, it was thought that a system to measure full field dye concentrations could be developed in a straight forward manner. Before the mechanics of jet interactions could be studied, however, the emphasis of this thesis had to shift towards what was revealed to be an extremely complex image analysis problem.

Laser sheet light flow visualization provides a wealth of qualitative information about the interactions between two jets. The extraction of quantitative information from those qualitative images has turned out to be a process fraught with non-linearities. Fluorescent dyes have been seen to mix so as to obscure the fluorescence of one of the component dyes. The light sheets did not provide a uniform lighting intensity over the experiment. Light sheets were attenuated by the dyes which they were passing through, further increasing their non-uniformity. The slide film, camera and lens combination may also contain non-linearities in recording light intensity and color as well as spatial distortions. In addition, the chemical processes used to develop the slides may contain further unknown variables. Random noise was added to the images during the recording and digitizing process. Even the video camera used to digitize the data slides contained more than one non-linear transformation.

In this thesis, many of these obstacles were overcome. The experimental procedure was chosen to minimize the problems where possible, and quantitative corrections were devised for those problems which could not be neglected.

The fluorescent hue of mixed dyes proved to be a very non-linear function of the mixture composition. Further work towards optimizing the concentration ratios of disodium fluorescein and rhodamine 610 is needed. Although rhodamine and fluorescein are generally regarded as the best fluorescent dyes to use in water, a potentially fruitful direction of research could be to test alternate dyes. This dye mixing problem was overcome in this study by using only a single dyed jet interacting with a clear water jet, and inferring the effect of mixing by comparing the interacting jet to the single jet case.

A model of laser light attenuation was developed, but was used to quantitatively evaluate attenuation only over a narrow range of dye concentration. Sufficient information was determined to show that attenuation was not a problem in the double light sheet illumination configuration chosen for the fluorescein-dyed jet tests. Further research can build on this model to correct for light sheet attenuation in experiments where it cannot be neglected.

The two light sheet configuration also created a sufficiently uniform light distribution so that the Gaussian intensity profile of the light sheets could be corrected for by normalizing jet images with a constant concentration background image. This technique was validated by successfully determining the concentration field of a known concentration laminar jet. It is probable that a light sheet

attenuation correction would be required before this technique could be used for experimental configurations where attenuation was significant.

Intensity non-linearities in the image digitizing process were quantitatively evaluated and corrected. The effect of the edge enhancement circuitry built into the Hitachi video camera was not corrected, but was not thought to be a significant problem in the existing study, as it only occurred in image regions of extremely high intensity gradients such as the initially laminar region of low Reynolds number jets. This edge enhancement circuitry should be disabled or bypassed in future work, and other researchers are cautioned that this type of enhancement circuitry may be present in other types of video cameras.

As a result of these challenges, the focus of this study shifted towards the development of the image analysis techniques. The analysis of jet interaction was thus limited in scope. In addition to demonstrating the analysis system's functionality, however, the jet experiments brought to light some interesting points.

A large number of images are required to obtain statistically valid descriptions of jet behavior. This number is minimized if all images in the ensemble are sufficiently separated in time so as to be statistically independent. Images are recorded with the film camera at a very slow rate, about 3 images per second. The images are not sufficiently spaced so that one roll of film (approximately 30 exposures) is a sufficient ensemble. It was estimated that at least 100 images from three separate tests were required to obtain statistically correct jet behavior. The spreading rates of concentration profiles in single jets were found to be almost

identical to those of the velocity profiles. This does not agree with previously accepted work which has found that $\delta_w/\delta_v \approx 1.4$. The small ensemble sizes used in this study may account for this discrepancy.

The velocity fields of interacting jets were found to be described remarkably well by point by point conservation of momentum, using a zero interaction entrainment model. This model, combined with some sort of jet center line displacement correction, merits further investigation.

An example of using this system as a new way of looking at jet behavior was shown by examining fluctuating mean isopleth areas. The area contained within a line of constant concentration varies by only 20% to 30%. This has implications, for instance, in flammability studies, because a relatively constant area of a jet will be within the flammability limits of the jet fluid. The jet isopleth area can be thought of as being similar to a candle flame in a breeze. The flame will flap about and change shape, but will maintain an approximately constant area. New techniques for utilizing the instantaneous concentration field information available from the image analysis system have not been thoroughly explored, and further work should be able to advance the study of mixing processes.

References

- Amorese, P. and Bloomfield, J., (1988), "A slew of standards for camera systems", ESD: THE ELECTRONIC SYSTEM DESIGN MAGAZINE, March, 1988, pp. 94-98.
- Armstrong, R.C., and Vosen, S. R., (1990), "Colour image processing as a combustion diagnostic of liquid propellant", COMBUSTION INSTITUTE/CANADIAN AND WESTERN STATES SECTION, SPRING TECHNICAL MEETING, Banff, pp. 289-292.
- Becker, H.A., and Booth, B.D., (1975), "Mixing in the interaction zone of two free jets", AICHE JOURNAL, Vol. 21, pp. 949-958.
- Brown, G.L., and Roshko, A., (1974), "On density effects and large structure in turbulent mixing layers", JOURNAL OF FLUID MECHANICS, Vol. 64, pp. 775-816.
- Cenedese, A., and Paglialunga, A., (1990), "Digital direct analysis of a multiexposed photograph in PIV", EXPERIMENTS IN FLUIDS, Vol. 8, pp. 273-280.
- Dahm, W.J.A., and Dimotakis, P.E., (1987), "Measurements of entrainment and mixing in turbulent jets", AIAA JOURNAL, Vol. 25, pp. 1216-1223.
- Dawson, B., (1988), "Focusing on image enhancement", ESD: THE ELECTRONICS SYSTEM DESIGN MAGAZINE, March, 1988, pp. 83-86.
- Demissie, M., and Maxwell, W.H.C., (1982), "Three-dimensional slot jets", ASCE JOURNAL OF THE HYDRAULICS DIVISION, Vol. 108, pp. 247-251.
- Dimotakis, P.E., Miake-Lye, R.C., and Papanтониou, D.A., (1983), "Structure and dynamics of round turbulent jets", PHYSICS OF FLUIDS, Vol. 26, pp.3185-3192.
- Elbanna, H., Gahin, S., and Rashed, M.I.I, (1983), "Investigation of two plane parallel jets", AIAA JOURNAL, Vol. 21, pp. 986-991.
- Elbanna, H., and Sabbagh, J.A., (1987), "Interaction of two nonequal plane parallel jets", AIAA JOURNAL, Vol. 25, pp. 12-13.
- Escoda, M.C., and Long, M.B., (1983), "Rayleigh scattering measurements of the gas concentration field in turbulent jets", AIAA JOURNAL, Vol. 21, pp. 81-84.
- Gonzalez, R.C., and Wintz, P., (1987), DIGITAL IMAGE PROCESSING, 2ND EDITION, Menlo Park: Addison-Wesley.

- Guilbault, G.G., (1973), **PRACTICAL FLUORESCENCE: THEORY, METHODS AND TECHNIQUES**, New York: Dekker.
- Hanson, R.K., (1986), "Combustion diagnostics: Planar imaging techniques", **TWENTY-FIRST SYMPOSIUM (INTERNATIONAL) ON COMBUSTION**, The Combustion Institute, pp. 1677-1691.
- Hernan, M.A., and Jimenez, J., (1982), "Computer analysis of a high-speed film of the plane turbulent mixing layer", **JOURNAL OF FLUID MECHANICS**, Vol. 119, pp. 323-345.
- Hesselink, L., (1988), "Digital image processing in flow visualization", **ANNUAL REVIEW OF FLUID MECHANICS**, Vol. 20, pp. 421-485.
- Hong, Z., and Chuang, S., (1988), "Kinetic theory approach to twin plane jets turbulent mixing analysis", **AIAA JOURNAL**, Vol. 26, pp. 303-310.
- Huber, A.H., and Arya, S.P.S., (1989a), "Video images of smoke dispersion in the near wake of a model building. Part I. Temporal and spatial scales of vortex shedding", **JOURNAL OF WIND ENGINEERING AND INDUSTRIAL AERODYNAMICS**, Vol. 31, pp. 189-223.
- Huber, A.H., and Arya, S.P.S., (1989b), "Video images of smoke dispersion in the near wake of a model building. Part II. Cross-stream distribution", **JOURNAL OF WIND ENGINEERING AND INDUSTRIAL AERODYNAMICS**, Vol. 32, pp. 263-284.
- Kiver, M.S., (1964), **COLOR TELEVISION FUNDAMENTALS**, 2ND EDITION, New York: McGraw-Hill.
- Knystautas, R. (1964), "The turbulent jet from a series of holes in a line", **THE AERONAUTICAL QUARTERLY**, Vol. 15, pp. 1-28.
- Koga, D.J., Abrahamson, S.D., and Eaton, J.K., (1987), "Development of a portable laser sheet", **EXPERIMENTS IN FLUIDS**, Vol. 5, pp. 215-216.
- Koochesfahani, M.M. and Dimotakis, P.E., (1985), "A 'flip' experiment in a chemically reacting turbulent mixing layer", **AIAA JOURNAL**, Vol. 23, pp. 1191-1194.
- Koochesfahani, M.M. and Dimotakis, P.E., (1985), "Laser-induced fluorescence measurements of mixed fluid concentration in a liquid plane shear layer", **AIAA JOURNAL**, Vol. 23, pp. 1700-1707.

- Koochesfahani, M.M., and Dimotakis, P.E. (1986), "Mixing and chemical reactions in a turbulent mixing layer", *JOURNAL OF FLUID MECHANICS*, Vol. 170, pp. 83-112.
- Kychakoff, G., Paul, P.H., van Cruyningen, I., and Hanson, R.K., (1987), "Movies and 3-D images of flowfields using planar laser-induced fluorescence", *APPLIED OPTICS*, Vol. 26, pp. 2498-2500.
- List, E.J., (1982a), "Turbulent jets and plumes", *ANNUAL REVIEW OF FLUID MECHANICS*, Vol. 14, pp. 189-212.
- List, E.J., (1982b), "Mechanics of turbulent bouyant jets and plumes", *HMT THE SCIENCE AND APPLICATIONS OF HEAT AND MASS TRANSFER*, Vol. 6, pp. 1-68.
- Long, M.B., Chu, B.T., and Chang, R.K., (1981), "Instantaneous two-dimensional gas concentration measurements by light scattering", *AIAA JOURNAL*, Vol. 19, pp. 1151-1157.
- Long, M.B., Tzeng, H.M., and Fourquette, D., (1983), "Time-resolved two-dimensional concentration measurements in an acoustically driven flow", *AIAA JOURNAL*, Vol. 21, pp.1085-1088.
- Marsters, G.F., (1977), "Interaction of two plane, parallel jets", *AIAA JOURNAL*, Vol. 15, pp. 1756-1762.
- Massons, J., Ruiz, X., and Díaz, F., (1989), "Image processing of the near wakes of stationary and rotating cylinders", *JOURNAL OF FLUID MECHANICS*, Vol. 204, pp. 167-184.
- Miller, D. R., and Comings, E. W., (1960), "Force-momentum fields in a dual-jet flow", *JOURNAL OF FLUID MECHANICS*, Vol. 7, pp. 237-256.
- Pani, B., and Dash, R. (1983a), "Three-dimensional single and multiple free jets", *ASCE JOURNAL OF HYDRAULIC ENGINEERING*, Vol. 109, pp. 254-269.
- Pani, B. and Dash, R. (1983b), "Three-dimensional wall jets from multiple outlets", Technical Note 376, *PROCEEDINGS OF THE INSTITUTION OF CIVIL ENGINEERS*, Vol. 75, Part 2, pp 735-749.
- Rajaratnam, N., (1976), *TURBULENT JETS*, New York: Elsevier Scientific Publishing Company.
- Reynolds, O., (1883), "The motion of water", *NATURE*, Vol. 28, pp. 627-632.

- Schäfer, F.P., ed., (1973), DYE LASERS, New York: Springer-Verlag.
- Schlichting, H., (1979), BOUNDARY LAYER THEORY, Seventh Edition, New-York: McGraw-Hill, pp. 729-757.
- Shlien, D.J., (1988), "Instantaneous concentration field measurement technique from flow visualization photographs", EXPERIMENTS IN FLUIDS, Vol. 6, pp. 541-546.
- Simonich, J.C., (1986), "Isolated and interacting round parallel heated jets", AIAA PAPER 86-0281.
- Tanaka, E., (1970), "The interference of two-dimensional parallel jets (1st report, experiments on dual jet)", BULLETIN OF THE JAPAN SOCIETY OF MECHANICAL ENGINEERS, Vol. 13, pp 272-280.
- Tanaka, E., (1974), "The interference of two-dimensional parallel jets (2nd report, experiments on the combined flow of dual jet)", BULLETIN OF THE JAPAN SOCIETY OF MECHANICAL ENGINEERS, Vol. 17, pp 920-927.
- Vranos, A., and Liscinsky, D.S., (1986) "Planar imaging of a turbulent methane jet", AIAA JOURNAL, Vol. 24, pp. 1564-1565.
- Vranos, A., and Liscinsky, D.S., (1988) "Planar imaging of jet mixing in crossflow", AIAA JOURNAL, Vol. 26, No. 11, pp. 1297-1298.
- Walker, D.A., (1987), "A fluorescence technique for measurement of concentration in mixing liquids", JOURNAL OF PHYSICS E: SCIENTIFIC INSTRUMENTS, Vol. 20, pp. 217-224.
- Walker, D.T., and Tiederman, W.G., (1989), "The concentration field in a turbulent channel flow with polymer injection at the wall", EXPERIMENTS IN FLUIDS, Vol. 28, pp. 86-94.
- Walsh, J.W.T., (1965), PHOTOMETRY, THIRD EDITION, New York: Dover.
- Wilson, A., (1988), "What color is color?", 1988 IMAGE PROCESSING CATALOG, Marlboro: Data Translation, Inc., pp. 8-20 to 8-23.
- Winter, M., Lam, J.K., and Long, M.B., (1987), "Techniques for high-speed digital imaging of gas concentrations in turbulent flows", EXPERIMENTS IN FLUIDS, Vol. 5, pp. 177-183.
- Zelt, B.W. (1991), PH.D. THESIS IN PROGRESS, University of Alberta, Edmonton, Alberta.